3-2023

Direct Collocation Methods for Comparison of Aerothermodynamic Models Effect on Hypersonic Trajectory Optimization by the Process of Continuation

Noor K. Khan

DIRECT METHODS FOR COMPARISON OF AEROTHERMODYNAMIC MODEL EFFECTS ON HYPERSONIC TRAJECTORY OPTIMIZATION BY THE CONTINUATION PROCESS

THESIS

Noor K Khan, Second Lieutenant, USAF

AFIT-ENY-MS-23-M-278

DEPARTMENT OF THE AIR FORCE
AIR UNIVERSITY

AIR FORCE INSTITUTE OF TECHNOLOGY

Wright-Patterson Air Force Base, Ohio

AFIT-ENY-MS-23-M-278

DIRECT METHODS FOR COMPARISON OF AEROTHERMODYNAMIC MODEL EFFECTS ON HYPERSONIC TRAJECTORY OPTIMIZATION BY THE CONTINUATION PROCESS

THESIS

Presented to the Faculty

Department of Aeronautical and Astronautical Engineering

Graduate School of Engineering and Management

Air Force Institute of Technology

Air University

Air Education and Training Command

in Partial Fulfillment of the Requirements for the

Degree of Master of Science in Aeronautical Engineering

Noor K Khan, B.S

Second Lieutenant, USAF

March 23, 2023

AFIT-ENY-MS-23-M-278

DIRECT METHODS FOR COMPARISON OF AEROTHERMODYNAMIC MODEL EFFECTS ON HYPERSONIC TRAJECTORY OPTIMIZATION BY THE CONTINUATION PROCESS

THESIS

Noor K Khan, B.S
Second Lieutenant, USAF

Committee Membership:

Lt Col Micheal Zollars, PhD
Chair

Lt Col Robert Bettinger, PhD
Member

Lt Col Darrell Crowe, PhD
Member

Lt Col Robert MacDermott, PhD
Member

Abstract

An algorithm was created to optimize trajectories of hypersonic glide vehicles with selected cost functions by applying the process of continuation to direct orthogonal collocation methods. The trajectory was optimized to maximize the range of launch position given a fixed terminal location. The process of continuation was used to address the complexity of the model whereby less complex solutions were used to seed increasing complex modeling in an iterative fashion. The hypersonic glide vehicle system dynamics were modeled with three-dimensional, three degree of freedom equations of motion assuming no thrust and a non-rotating Earth for the states defined as vehicle radial position, latitude, longitude, speed, flight path angle, and heading angle. The control for the system was placed on the bank angle of the vehicle. Three aerothermodynamic models were compared when input as path constraints to calculate the stagnation point heating rate at the nose as well as integrated for heat load. Use of the continuation method enabled rapid generation of converged optimized trajectories. Differences noted between iterations of the continuation process showed the evolution of vehicle trajectories based on the problem formulations. The continuation method was demonstrated as an effective tool for optimization. Analysis of the aerothermodynamic models through continuation revealed the coupling of various systems within the hypersonic model that affected how the algorithm converged upon a solution to meet the given maximum heat rate limit. Each aerothermodynamic model rendered a different optimal trajectory with the Sutton Graves model producing the most conservative, highest stagnation point heat rate and heat load estimates and the Galman model predicting the lowest values.

Table of Contents

Page

Page

List of Figures

List of Tables

List of Abbreviations

Abbreviation		Page
LGL	Legendre-Guass-Lobatto	30
IPOPT	interior point optimizer	31
SNOPT	sparse nonlinear optimizer	31
3D	three dimensional	34
AI	artificial intelligence	44

List of Symbols

Symbol		Page
q	Dynamic pressure	20
m	Vehicle mass	20
J	Cost function	25
t_0	Initial time	26
t_f	Final time	26
L	Lagrangian	26
u	Control	26
x	States	26
C	Proportionality constant	41
$\dot{Q}_{max}$	Maximum heat rate	41
T_g	Gas temperature	42
T_w	Wall temperature	42

DIRECT METHODS FOR COMPARISON OF AEROTHERMODYNAMIC MODEL EFFECTS ON HYPERSONIC TRAJECTORY OPTIMIZATION BY THE CONTINUATION PROCESS

I. Introduction

1.1 Motivation

The beginning of the 1960s was the beginning of exploration into the hypersonic realm. Many "firsts" were accomplished during this time period, such as the first human to travel at hypersonic speeds in a space capsule and the first human to fly at a "mile-per-minute" in an aircraft, the X-15 [1]. These firsts demonstrated the applications of new aerodynamic theories and technologies. The hypersonic field is upon another period of innovation with more advanced technologies at researchers' disposal to help solve complicated hypersonic problems.

Hypersonic systems, vehicles that travel faster than Mach 5, are being studied to aid in the development of operational systems in the near-future. The history of hypersonic research has ebbed and flowed with national interests and funding. During the Cold War, it became abundantly clear to the world how important it was to possess the technological advantage. Nations were focused on funding missile and nuclear research. Additionally, the 1960s was also the age of the space race. While funding may have slowed for changing priorities in the past, research in hypersonic weapons never stagnated completely as it has been a part of the conventional prompt global strike (CPGS) program since the early 2000s [2]. The prompt global strike mission was aimed at providing "the United States with the ability to strike targets

anywhere on Earth with conventional weapons in as little as an hour, without relying on forward-based forces" [3]. Among the capabilities considered in achieving this objective were hypersonic systems.

In today's strategic environment, there is an ever-increasing need for the development of simulation programs to accurately model the maneuverability of high-speed vehicles [2]. Globally, hypersonic vehicle programs have become active in multiple nations. The United States has focused its research efforts on developing hypersonic systems that would enable "responsive, long-range, strike options against distant, defended, and/or time-critical threats [such as road-mobile missiles] when other forces are unavailable, denied access, or not preferred," as stated by the former Vice Chairman of the Joint Chiefs of Staff and former Commander of U.S. Strategic Command General John Hyten [2]. Due to the complexity of hypersonic systems and the requirement for testing, accurate and robust modeling is necessary for system development.

Hypersonic vehicles fall into three general classes: ballistic reentry vehicles, hypersonic glide vehicles (HGV), and hypersonic cruise vehicles (HCV). The difference in trajectories can be observed in Figure 1. Ballistic missiles follow a parabolic trajectory, with minimal control and will operate exo-atmospherically, while glide and cruise vehicles operate endo-atmospherically for the majority of their trajectory. Glide vehicles do not utilize propulsion after launch while cruise vehicles engage in powered flight.

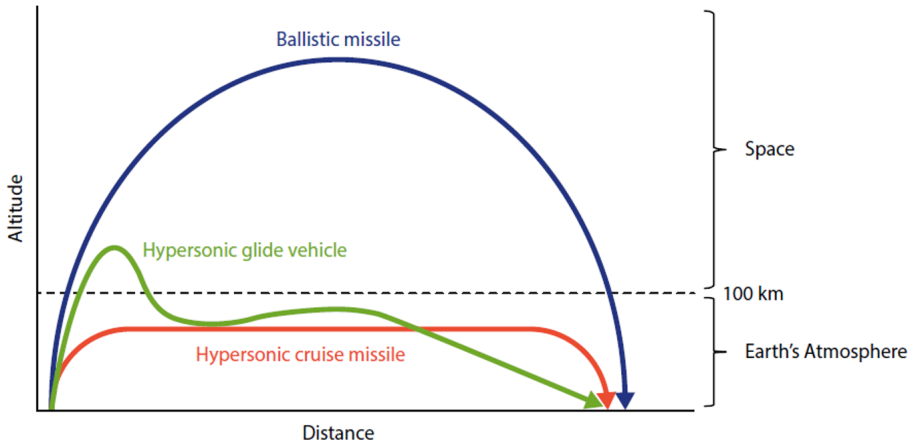

Figure 1. Notional trajectories of a ballistic missile, hypersonic glide vehicle, and hypersonic cruise missile [4].

Endo-atmopsheric flight provides an advantage for hypersonic glide and cruise vehicles due to the ability to maneuver during flight. The maneuverability allows for a broader range of applications. An endo-atmospheric flight path may result in delayed detection from a terrestrial based radar due to a limiting line of sight, as illustrated in Figure 2. A radar would not detect a low flying vehicle until much later in its flight path, thus compressing the timeline for any counter measures.

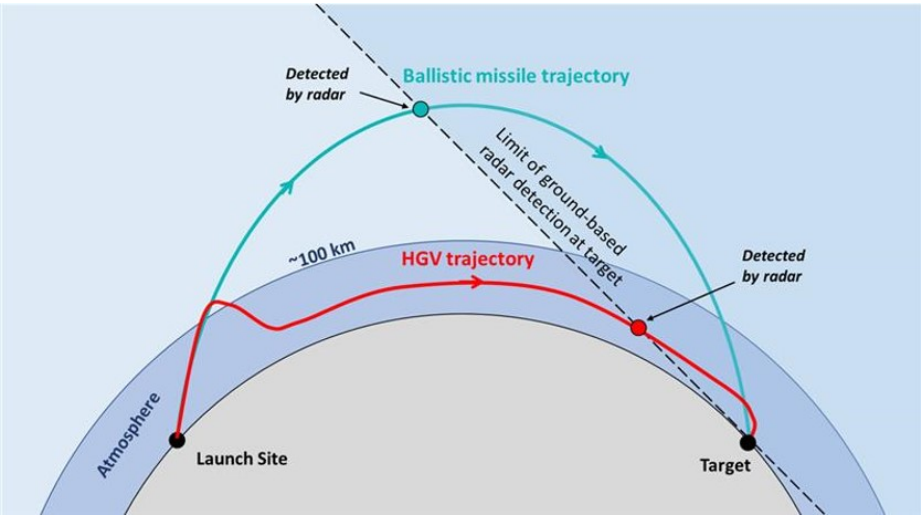

Figure 2. Radar detection points during trajectories of a HGV and a ballistic missile [2].

1.2 Problem Description

The current research stems from the push from the Pentagon and Congress to deploy hypersonic weapons [2] and funding from the Air Force Research Laboratory (AFRL). Research is focused on progressing simulations to create feasible trajectories for various hypersonic missions and vehicles. The long term goal of the research effort is to provide an algorithm for mission strategists to plan a feasible trajectory for a hypersonic vehicle, be it glide or cruise, between a given target and initial condition. The algorithm should be able to accommodate various mission objectives, incorporated as performance measures. The entire flight path from commencement to termination would be modeled at a sufficient level of fidelity. A sufficient level of fidelity would include multiple constraints as well as the integration of the various disciplines involved in accurately simulating a hypersonic system.

The scope of this research is limited to the initial realization of the simulation software. The goal is to produce optimized trajectories for a generic hypersonic vehicle in the glide phase of flight with a heating path constraint to gain insight on the effects of various aerothermodynamic models. The process of continuation will be explored as a method to solve the complex problem of hypersonic trajectory optimization.

Direct orthogonal collocation methods, interchangeably called pseudospectral methods, were used to solve for optimized hypersonic trajectories. The pseudospectral solver used herein was the GPOPS-II algorithm. Additionally, a comparison of aerothermodynamic heating models will be analyzed including their effect on an optimized trajectory. The heating constraints will be integrated into the system as path constraints with a maximum limit not to be exceeded. The research effort herein will focus on modeling hypersonic glide vehicles with a three degree of freedom dynamic system. The mission chosen for this research effort was to maximize the range given

a final target by leaving the initial vehicle position undefined. The algorithm would then be free to converge upon an initial position that would maximize the trajectory range while still arriving at the prescribed endpoint.

1.3 Research Hypothesis

The continuation process enacted upon an optimization software will result in quick convergence times. The continuation process will also allow for a converged solution of a complicated problem with path constraints. Different aerothermodynamic models will result in different trajectories and achieve different minimum heating rates and heat loads. Comparing aerothermodynamic models will reveal the most conservative method of calculating the stagnation point heating rate.

1.4 Research Tasks

- Produce a converged solution for a simple hypersonic problem
- Create an algorithm for the continuation process
- Find a converged solution trajectory for a complicated problem with a path constraint on the stagnation point heating rate through the continuation process
- Research aerothermodynamic models and compare trajectory solutions

1.5 Research Objectives

While there has been research in the field of optimizing hypersonic trajectories, the knowledge in this research topic is far from complete. The ability to generate hypersonic trajectories has been demonstrated, but the process is yet to be refined. There are two objectives to begin the realization of the over-arching goal of creating an

algorithm that can accurately model a hypersonic trajectory. The first research objective is to understand the applicability of the continuation process with pseudospectral methods. The second research objective is to compare various aerothermodynamic models and their effects.

The applicability and utilization of the continuation process will be demonstrated with iterations of code. Continuation is the method of starting with a simple problem and using the solution to seed a more complex problem. The progression of optimized solutions utilizes different performance measures, i.e. missions, to build up the complexity. The different performance measures demonstrate the adaptability of the continuation process and simulation tool. The initial seed used was the solution from the simple iterative Fourth Order Runge Kutta (RK4) process. The first use of GPOPS-II code produced a converged solution for a generic HGV with the RK4 seed. The next iteration produced a converged solution of the High Speed Army Reference Vehicle (HARV) [5] optimized for a maximum range.

The solution of the optimized HARV trajectory was used to accomplish the second objective of comparing aerothermodynamic models and their effects on an optimized trajectory. A heat rate constraint was appended onto the code that produced the HARV trajectory solution as a path constraint. Chapman [6], Sutton-Graves [7], and Galman [8] equations were used as the three aerothermodynamic models in comparison due to their similar fidelity levels. Each provides a stagnation point heating rate. A heating rate profile and heating load profile were then determined from each model to show the direct differences. Additionally, the resulting trajectories from the application of each aerothermodynamic model were compared.

1.6 Assumptions

The system dynamics were derived with the following assumptions:

- No thrust
- Spherical, non-rotating Earth
- Drag parallel and opposite to velocity
- Lift perpendicular to velocity
- The gravity vector is parallel to the vehicle position vector

Additional assumptions in this research effort include:

- Constant coefficient of lift C_L and coefficient of drag C_D
- The vehicle surface is in radiative equilibrium with the surroundings so the heat rate constraint is directly linked to the surface temperature [9]

1.7 Document Overview

This document contains five chapters. This first chapter provided an introduction to the research topic with motivation and scope of the work. Chapter II provides the background information on the various disciplines and techniques involved in hypersonic trajectory optimization research. A summary of previous relevant research is provided for context. Chapter III describes the methods employed to accomplish the research objectives. Details on the problem formulations and models used are included. The research results on continuation and comparison of the aerothermodynamic heating models are presented and analyzed in Chapter IV. Chapter V wraps up with an overall analysis of the results, as well as a summary of the thesis to include any challenges encountered as well as the future direction of research.

II. Background

Hypersonic trajectory optimization is a complicated problem which incorporates a multitude of disciplines. The background chapter is aimed at building an understanding of the disciplines utilized for the current research effort. Section 2.1 lays the foundation of understanding hypersonic flow regime. Section 2.2 explains some heat transfer theory and aerothermodynamic models. Section 2.3 explores various vehicle models. Section 2.4 provides an overview of optimal control theory and the optimization program to be used. Lastly, Section 2.5 is a literature review of the relevant research conducted up to the current day to provide context for this research effort.

2.1 Hypersonic Flow

Hypersonic flows differ significantly from subsonic and supersonic flows. There is not a single event that marks the transition from supersonic to hypersonic flow. Generally flows above Mach 5 are considered to be hypersonic [1]. The defining characteristic that distinguishes hypersonic flow from other flow regimes is energy. Bertin [10] describes the flow as having transitioned into the hypersonic regime when the internal energy of the flow is small relative to the kinetic energy (KE) of the flow. Hypersonic flow is physically different from supersonic flow [1]. The relatively large amount of kinetic energy transfers or transforms into alternate forms; for example, chemical reactions of molecules in the atmosphere. Chemical reactions of air molecules are very unlikely to occur in other flow regimes and are considered negligible. The kinetic energy transformation causes different physical phenomena. Anderson [1] compiled four defining characteristics of hypersonic flow: thin shock layers, the entropy layer, viscous interactions, and high-temperature flow. Additionally, low-density flow

is often a commonly experienced regime of hypersonic flights, but not necessary since hypersonic speeds can be achieved in higher density air. For example, often times shuttles on a reentry trajectory will experience hypersonic speeds at high altitudes near space where the air has a lower density than air closer to the Earth's surface. However, a hypersonic glide vehicle can also experience hypersonic speeds closer to the Earth's surface in higher density air.

The flow field between the shock wave and vehicle body is thin relative to shocks in slower supersonic flow conditions. This is consistent with oblique shock theory [1]. Figure 3 shows the shock wave angle of a wedge with a 15° half-angle at Mach 30 in calorically perfect gas, assuming a constant specific heat ratio of 1.4. Solving with oblique shock theory equations, the resulting shock wave angle is 18° [1], whereas the same set up at Mach 2.5 would result in a shock angle of 37° [11].

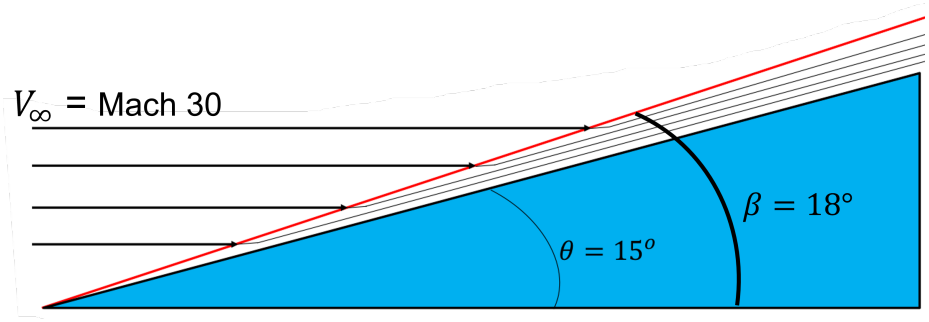

Figure 3. Thin shock layer of 15° wedge in hypersonic flow [1].

Large entropy gradients occur inside the shock wave due to the streamline encountering different strengths of the shock depending on the location from centerline. Crocco's theorem relates areas of large entropy gradients with areas of strong vorticity. The interaction between the inviscid ambient flow and boundary layer results in complicated physical interactions barring any attempts at a simple standard boundary layer calculation. A more detailed explanation can be found in [1].

Additionally, hypersonic flow contains a large amount of kinetic energy. The

kinetic energy of the freestream inviscid flow is transferred to the fluid within the viscous boundary layer increasing the temperature. Pressure remains constant in the boundary layer. To keep pressure constant with an increase in temperature, the density must decrease. With the mass flow also remaining unchanged, the boundary layer area must increase to accommodate a lower density. A thicker boundary layer affects the surface-pressure distribution. Subsequently lift, drag, and stability of the vehicle are affected. Skin friction and heat transfer also increase. Changes to the inviscid flow are caused by interaction with a viscous boundary layer. Viscous interaction is the interaction between the outer inviscid flow and the viscous boundary layer. Viscous interaction effects are more prominent near the nose of a vehicle where the pressure is greatest. The surface-pressure distribution is less extreme downstream, but the effects remain. [1].

The transfer of kinetic energy to internal energy of gas molecules increases the temperature significantly, i.e. thousands of Kelvin. The high temperature excites the molecules and leads to chemical reactions. Once the flow becomes a chemically reacting flow, the assumption of a constant ratio of specific heats is no longer valid and must be accounted for to achieve realistic results. Convection and radiation are two methods of heat transfer from the hot boundary layer to the cooler vehicle surface. Convective heating occurs when objects are in contact with each other. Radiative heating is when the temperature of an object is relatively higher than a near-by object and heat waves increase the temperature of the cooler object. Convective heat transfer is the more common method of heat transfer in all regimes and the largest contributor to the heat rates and heat load experienced by an object. However, for the special cases when radiative heating is present, it may become the dominant method [1].

Another consideration of hypersonics are the specifics of the flow regimes a vehicle

may encounter at hypersonic speeds. Low-density flow is a flow regime. A more commonly known flow regime is the continuum flow regime. At sea level the average distance between molecules of air, defined as the mean free path (λ), is 2.17×10^{-7} m. For a vehicle flying through the air at sea level is considered to be flying through a continuum flow as it will experience a continuous medium. However, at higher altitudes, air density decreases. At an altitude of 342,000 m, $\lambda = 1$ m and the assumption of continuum flow is no longer accurate. A sufficiently dense atmosphere is required for aerodynamic controls to work on a vehicle. Low-density flow is the regime of flow where aerodynamics must be considered through the lens of kinetic theory, as the assumption of continuum flow is not applicable. The free molecular regime is when individual molecular impacts begin to matter due to the extremely low density beginning around 500,000 m in altitude. A reentry vehicle will travel through various flow regimes upon its reentry from space back down to sea level. Accurate aerodynamics can only be predicted by applying the correct assumptions dictated by the flow regimes. Knudsen number Kn is the similarity parameter that governs the flow regime a vehicle is in. Kn is defined as $Kn = \lambda/L$ where L is the characteristic length of the vehicle body. A smaller Kn indicates a flow regime closer to continuum, while a higher Kn indicates a regime closer to the free molecular regime. Therefore, different sized vehicles can experience different flow regimes at different altitudes [1].

The key to determining the aerodynamics of a vehicle in hypersonic flight, such as lift and drag, is in the ability to calculate the surface-pressure distributions over the vehicle body. Hypersonic flow is non-linear, which inherently makes those calculations complicated. To find aerodynamic forces and moments on the vehicle, there are two options: aerodynamic look-up tables [12] [13] [14] or calculating the surface pressure distribution [15] [16]. Aerodynamic tables are convenient but only when available. When the field of hypersonics was first being explored, access to current-

day computing power was non-existent and as a result, a variety of simplified models or theories were used, namely, local surface inclination methods. Local surface inclination methods were built off the inviscid, linearized, two-dimensional, supersonic flow theory definition of the pressure coefficient,

$$C_p = \frac{2\theta}{\sqrt{M_\infty^2 - 1}} \tag{1}$$

where θ is the local deflection angle and M_∞ is the freestream Mach number [1]. Equation (1) is not valid for hypersonic flows, however, the concepts can be modified and then applied to hypersonic flows, restricted to thin bodies at small angles of attack. Local surface inclination methods were useful to aerodynamicists because a detailed solution of the complete flowfield is not required to predict the pressure distribution over the vehicle body. Once the pressure distribution is known, the lift and drag can be calculated. The ability to calculate coefficients of lift and drag are beneficial, especially when aero-tables are unavailable [1].

$$C_p = 2sin^2(\theta) \tag{2}$$

One of these surface inclination methods is the Newtonian method. Isaac Newton derived the Newtonian sine-squared law, Equation (2), "for the force on an inclined plane in a moving fluid" via his fluid-dynamic theory in the 1680s [1]. A schematic for this law is provided in Figure 4 where V_∞ is the velocity of the freestream and θ is the angle the plate is inclined to the freestream. While the law was created for application of low speed flows it was proven to be inaccurate. However, this is not the case when applied to hypersonic flows.

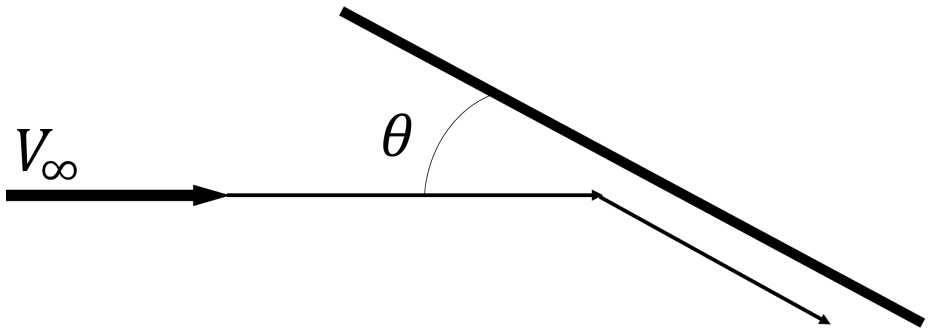

Figure 4. Schematic of Newtonian impact theory [1].

Newton unknowningly predicted thin shock layers when drawing an image of freestream flow impacting the surface then following parallel to the body surface downstream. To find the local surface deflection angle, θ, at a point on the body for shapes other than a flat plat, a tangent line to the body is drawn at that point and the angle is then between that tangent line and the freestream. Newtonian's theory assumes that the flow does not wrap around the body. The pressure coefficient C_p is only calculated where the freestream impacts the body on the frontal area. Therefore, the pressure on the leeward side, or shadow region, is assumed to be the freestream pressure and $C_p = 0$ [1].

$$C_p = C_{pmax} sin^2(\theta) \tag{3}$$

Lester Lees [17] proposed a modification to the Newtonian flow theory, provided in Equation (2), with the maximum value of the pressure coefficient C_{pmax} in Equation (3). C_{pmax} is evaluated at the stagnation point behind a normal shock wave and calculated from an equation derived from normal shock theory.

Finally, by keeping the vehicle limited to speeds below Mach 10, making assumptions to dismiss some high gas temperature effects within the boundary layer is permissible. Staying below Mach 10 is most beneficial for simplifying assumptions due to avoidance of most chemically reacting flow complications which become more promi-

nent at speeds higher than Mach 10. Inviscid methods are valid to use for hypersonic flow calculations because they account for thin shocks and surface heating. Viscous effects on the vehicle will be accounted for via heat transfer methods applied to the problem, discussed in Section 2.2.

2.2 Aerothermodynamic Models

As discussed in Section 2.1, a vehicle traveling at a hypersonic speed contains more kinetic energy relative to a lower speed regime. As it slows, the KE is transferred into other forms, such as thermal energy. The thermal energy is transferred to the vehicle and boundary layer air molecules. However, only a small fraction of the total KE is transformed into heat and transferred to the vehicle body [18]. The nose region of the Apollo reentry capsule reached 11,000 K on its return through the Earth's atmosphere [1]. For context, titanium melts at 1943 K [19]. The fraction of energy transformed to thermal energy is dependent on the vehicle size, vehicle shape, aerodynamic regime, and speed. Usually around 1-5% of total thermal energy near peak heating is transferred to the entry system [18].

The accurate prediction of the heating environment of an atmosphere's interaction with a system is important for the design to ensure survivability. Typically, an over prediction of heat rate is preferred to create room for uncertainty, but is not required. The discipline of aerothermodynamics is closely coupled with a thermal protection system (TPS) design because it is based on heat calculations. The type of material used for a TPS is determined by the heat rate, while the TPS thickness is determined by the heat load. There is an important distinction between heat rate and heat load [18]:

- Heat rate ($\dot{q}$) is the instantaneous heat rate at a point on the vehicle. Typical units are Watts per meter squared (W/m^2) [18]

- Heat load (Q) is the integration of heat rate with time over a trajectory, usually Joules per meter squared (J/m^2) [18]

Heat rate is the more commonly calculated term in hypersonic trajectory optimization problems. Examples of heat rate calculations can be found here: [12] [14] [15] [16] [20] [21] [22] [23] [24]. The trajectory flown can affect heating on the vehicle as well, for example, comparing the difference in instantaneous heat rates at the stagnation point vs. the total heat load. To illustrate this, Figure 5 compares two identical ballistic vehicles on a reentry trajectory with differences in either flight path angle (γ) in Figure 5a, i.e., steepness of reentry, or ballistic coefficient (β) in Figure 5b [18]. The ballistic coefficient is

$$\beta = \frac{W}{C_D S} \tag{4}$$

where W is the weight, C_D is the drag coefficient, and S is the wetted area [1]. Taken from [18], Figure 5a shows the different trajectories resulting from shallow and steep entries. The steeper angle has a higher peak heat rate and a lower total heat load relative to the shallower angle. Figure 5b compares trajectories from high and low ballistic coefficients. The higher ballistic coefficient results in both a higher peak heat rate and heat load relative to the lower β [18]. For a vehicle to have a higher ballistic coefficient, looking at Equation (4), would mean the vehicle has less drag, less wetted area, or more weight.

(a) Difference in flight path angle. **(b) Difference in ballistic coefficient.**

Figure 5. Trajectories of two identical ballistic vehicles [18].

The results of Figure 5 are summarized in Table 1.

Table 1. Differences in heat rate and heat load for trajectories with various flight path angles and ballistic coefficients.

	Increase flight path angle (γ)	Increase ballistic coefficient (β)
Heat Rate	Increase	Increase
Heat Load	Decrease	Increase

The theory of stagnation point radiative heat transfer is the foundation for a lot of the aerothermodynamic models. When atoms or molecules collide, usually, they will emit a photon that carries energy with it. Photons, which effectively travel instantaneously, are emitted isotropically. The integration of those photons hitting the surface, multiplied by the energy they contain, is radiative heating. In other words, radiative heating is the heat transfer to the vehicle from radiation produced by excited atoms and molecules in the shock layer [18].

Calculating heat rate at a stagnation point is the method of preference in the field of hypersonic trajectory optimization problems. Most research uses models that only account for convective heat transfer. From the literature review conducted in Bettinger's section on "The Atmospheric Flow Environment and Heat Flux", convective heat transfer was concluded to be dominant over radiative heat transfer at speeds below 11 km/s [25]. For example, an ICMB velocity of 6 km/s experienced a

convective stagnation heat rate around 3 times larger than the radiative heat rate. Maximum radiative heat rates were confirmed to be parabolic with a peak around 11 km/s. The research effort herein will set a maximum speed boundary limit of 8 km/s in attempt to produce more realistic heat rate estimates.

Chapman derived a general version of a stagnation point heat rate equation from boundary-layer equations beginning with the Navier Stokes equations of continuity, momentum, and energy [6]. The heat rate equation at a stagnation point has the assumptions of axially symmetric flow, equilibrium air, and negligible radiative heat transfer. Chapman states that neglecting radiative heat transfer is realistic "if the ratio of the energy radiated (per unit mass along a streamline) to the local static enthalpy is small" [6]. Radiative heat transfer can be assumed negligible at speeds below Mach 10. Therefore, the equation only accounts for convective heat transfer and calculations of heat transfer rates will be inaccurate.

$$\dot{q_s} = \frac{C}{\sqrt{R}}(\frac{\rho_\infty}{\rho_0})^n(\frac{\bar{u}}{cos(\phi)})^m \tag{5}$$

The general Chapman equation of heating rate at a stagnation point ($\dot{q_s}$) can be calculated with Equation (5) where C, n, and m are constants that depend on the type of boundary layer flow [6]. Typical values for the constants are $m = 3$ for Earth, $n = -0.5$ for laminar flow, and $C = 17,000$ when in air.

$$\dot{q_s} = 1.63 \times 10^{-4}(\frac{\rho}{R_n})^{\frac{1}{2}}V^3 \tag{6}$$

Equation (6) is the more commonly found form of the Chapman equation which is for Earth's specific atmosphere. The Chapman model equation is a simplified aerothermodynamic model. Equation (6) has been written without the hot wall correction term because the term is frequently neglected in hypersonic flows where

the wall enthalpy is much lower than the freestream enthalpy [18]. The form of Equation (6) for the Chapman model has been used by many authors [12] [14] [20] [21] [22] [23] [24]. There are additional simplified stagnation point heating models that follow a similar equation as the Chapman model.

Overestimation and underestimation from stagnation point heating rate models of similar fidelity to the Chapman model were shown in Bettinger's section on "Verification and Selection of Heat Flux Model" [25]. Stagnation point heating rates calculated from various estimation models were compared to flight data obtained from various NASA vehicles including two flights in 1966 from suborbital Apollo command modules, a space shuttle (STS-5), and a Crew Exploration Vehicle (CEV), as depicted in Figure 6.

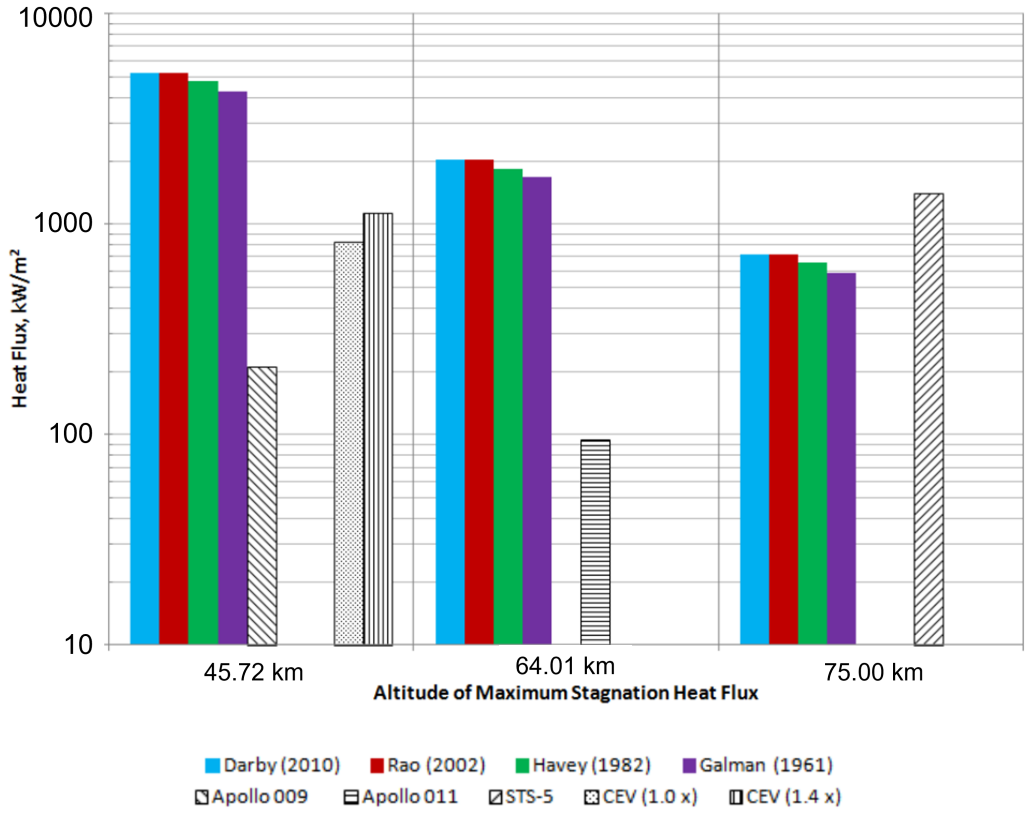

Figure 6. Comparison of stagnation point heat rate models with flight data from various NASA vehicles [25].

For blunt body vehicles, capsule-like in design, models overpredicted heat rates by an order of magnitude or more. For the winged body of the space shuttle, in the far right column of Figure 6, models underestimated heat rates by around 50%. However, Bettinger points out some considerations that justify the use of a stagnation point heat rate models [25]. He noted that the largest differences between model estimations and flight data occurred with blunt body spacecraft, like the capsule design of the Apollo command module and CEV. Additionally, models excluded any radiative heat transfer contributing to the inaccuracies. Lastly, final consideration was the accuracy of the flight data being used to validate estimations. The closest approximation of the models was to the space shuttle, a winged vehicle [25]. While none of these NASA vehicles resemble the sharp nosed vehicle models to be used in this research, it is important to understand the inaccuracies of a simple heat rate model.

A higher fidelity model is the reference enthalpy, or reference temperature, method which takes into account compressibility effects in a simplified manner via some reference temperature inside the boundary layer [1]. Reference enthalpy methods are better suited for slender bodies [16] due to the simplicity of application to hypersonic problems [1]. One such method of reference enthalpy is Eckert's Reference Enthalpy method [1] [16], defined as

$$\dot{Q}(u, T_x) = St(T_r)\rho(T_r)V_e[H_{aw}(T_r) - H(T_w)]. \tag{7}$$

$$St(T) = \frac{c_f(t)}{2Pr(T)^{2/3}} \tag{8}$$

$$H_{aw}(T) = H(T_e) + Pr(T)^{r_f}\frac{V_e^2}{2} \tag{9}$$

H in Equation (7) is enthalpy calculated with Equation (9), ρ is air density, St is the Stanton number calculated with Equation (8), and all are temperature dependent.

T_r is the reference temperature, T_e is the edge temperature, c_f is the skin friction coefficient, and r_f is the recovery factor calculated with Equation (10).

$$\begin{cases} r_f = \frac{1}{3}, & c_f(T) = 0.370[log_{10}Re(T, x_{le})]^{-2.584}, \text{ turbulent flow} \\ r_f = \frac{1}{2}, & c_f(T) = 0.664Re(T, x_{le})^{-0.5}, \text{ laminar flow} \end{cases} \tag{10}$$

For Equation (10), $Re(T, x_{le}) = \frac{\rho(T)V_e x_{le}}{\mu(T)}$ and x_{le} is the distance from the leading edge. The edge temperature will equal the reference temperature for a flat plate [1] which is a valid when using the Modified Newtonian Method as applied by Coulter [16].

Additionally, the vehicle can experience enormous forces at high speeds that would need to be constrained to ensure its structural survival. Therefore, a normal load (n) and dynamic pressure (q) constraint will likely be incorporated into the final simulation tool [23] as

$$n = \frac{1}{m}\sqrt{L^2 + D^2} \leq n_{max}, \tag{11}$$

$$q = \frac{1}{2}\rho V^2 \leq q_{max}, \tag{12}$$

where m is the vehicle mass.

One of the highest fidelity heat transfer models is computational fluid dynamics (CFD). CFD provides an accurate numerical analysis of a system. It is the most computationally expensive of all the previously mentioned methods, however, it's accuracy provides invaluable detail. The results are able to be fed back into an optimization algorithm or used as validation. More on CFD can be found in [26]. While CFD was not incorporated in this research, it was considered in collaboration with a research counterpart and will be studied in future work.

2.3 Vehicle Models

Starting in the 1950s with the space race, a need for new technology arose. Vehicles and capsules had to be designed to withstand the heat from reentry into the atmosphere to ensure survival [27]. The emergence of space flight meant the effects of hypersonic flow conditions had to be incorporated into new technologies [1] for both manned and unmanned vehicles. As research expanded, different ideas were presented ranging from non-winged blunt body capsules, like the Apollo 10 capsule shown in Figure 7a, to slender symmetrical winged vehicles [27]. In 1961, the X-15 achieved its first hypersonic flight endo-atmospherically, exceeding Mach 5 [1].

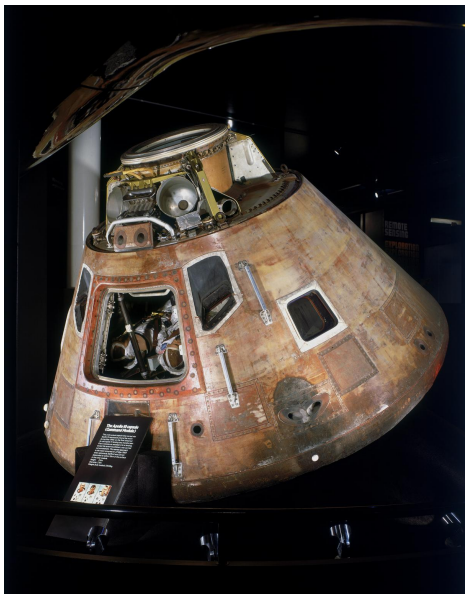

(a) Apollo 10 command module [28].

(b) North American X-15 aircraft [29].

Figure 7. Blunt body, Apollo 10, and slender body, X-15, vehicles.

Blunt bodies became the choice of shape for manned reentry vehicles, which achieve hypersonic speeds, due to their ability to create normal shock waves. Shock waves dissipate energy into the surrounding gas by converting KE into internal energy of the gas molecules. Therefore, chemical reactions, dissociation, and ionization can occur at higher speeds [18]. However blunt body capsules have minimal aerodynamic

maneuvering [30] [18]. Maneuvering is required for applications of precision. Slender bodies have lower drag and are more maneuverable than blunt bodies [18]. Slender body vehicles are driven by oblique shock relations, whereas blunt bodies are driven by normal shock relations [17].

A majority of research in the field of hypersonic trajectory optimization use slender body models or modification on existing experimental slender body vehicles, like the SR-71 [12], X-15, generic Common Aero Vehicle (CAV) model [12] [24], Generic Hypersonic Aerodynamic Model Example (GHAME) [14], X-43 [31], and X-51 [31]. A lot of projects have focused on hypersonic glide vehicles, thereby, neglecting to include a propulsion model [16] [32] [20] [13] [22] [15] [23] [9]. For the current research, the High-Speed Army Reference Vehicle (HARV) was used [5]. The HARV is an open source geometry created by the Army to facilitate foundational research and fill the gap in knowledge of hypersonic vehicle aerothermodynamics. HARV dimensions are given in calibers allowing for scaling. A few variations of the vehicle were provided in the technical note [5]: the choice between a cone or ogival nose and three or four fins. Figure 8 shows a solid model representation of the cone nose configuration with four fins.

Traditionally, hypersonic glide vehicles are either boost-launched or air-launched. When ground or boost-launched, the launch is typically accomplished via a rocket booster. This is a relatively straight forward phase of flight which many papers do not include in their trajectory optimization model. Often the addition of a launch phase is recommended as future work for completeness.

Hellman in 2014 worked on a project of simulating various launch trajectories to get the Defense Advanced Research Projects Agency (DARPA) XS-1 up to Mach 10, which was one of the program's requirements [21]. The paper focused on trading dynamic pressure values, via constraints, for sustained flight time above certain Mach

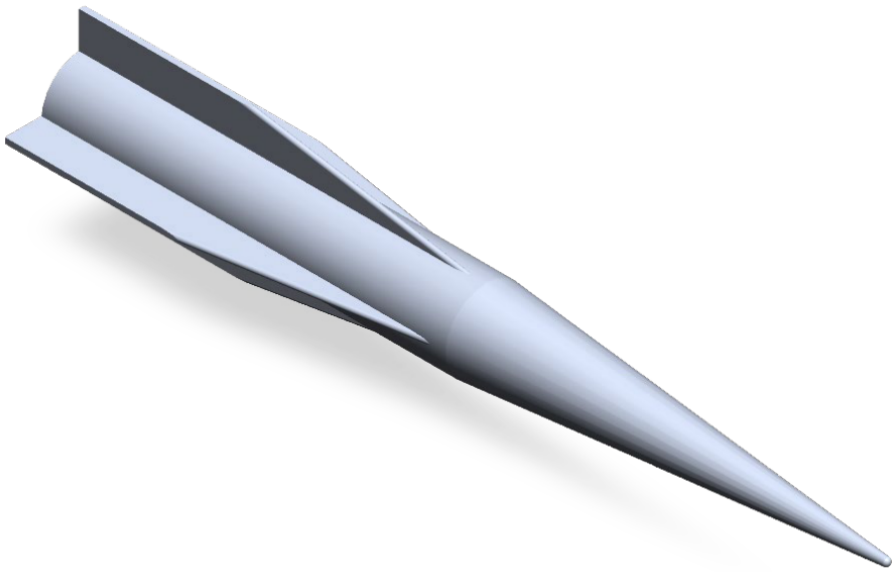

Figure 8. Solid model rendering of HARV with cone nose and four fins [5].

numbers. Unfortunately the paper did not go into detail on the exact propulsion model used to simulate a reusable first stage rocket which was the modeled propulsion system. However, it can be inferred that a simple one-dimensional thrust model was used.

$$T = g_0 \dot{m}_f I_{sp} \tag{13}$$

An example of a standard thrust equation is Equation (13) [14]. The one-dimensional thrust model in Equation (13) is commonly found in papers that incorporate a propulsion model into their system. Oftentimes, a more complicated propulsion model is found in papers like Dalle [31] who focused on a hypersonic cruise vehicle (HCV) via incorporating air-breathing propulsion models with a hypersonic trajectory. While propulsion models for air-breathing engines in the hypersonic flight regime are complicated and necessary to model for HCVs, HGVs do not include these dynamics. The flight dynamics remain the same throughout the glide phase of an HGV.

Vehicle properties are incorporated into both three degree of freedom (3DOF)

and six DOF equations of motion (EOMs). The connection of a vehicle's properties is easily recognized in a six DOF model where the forces and moments are calculated for each surface of the vehicle. For 3DOF models, the dynamics of the system assume a psuedo point mass, due to the incorporation of lift and drag but not encapsulating all forces and moments. Vehicle properties such as mass and wetted area are included in calculations. The psuedo point mass assumption is common when utilizing 3DOF EOMs.

2.4 Optimal Control Theory

The goal of optimal control theory is to solve for a set of control inputs of a dynamic nonlinear system that will result in system states which will minimize (or maximize) a performance index all while satisfying system dynamics and any defined constraints or boundary conditions [14].

2.4.1 Optimal Control Problem Formulation

Kirk defines three major factors that form an optimal control problem [33]. Defining these will build the foundation for understanding the control methodology outlined in Chapter 3. The first factor in the formulation of an optimal control problem is the mathematical model of the system or process to be controlled [33]. System dynamics are mathematically represented with ordinary differential equations (ODE). The ODEs are commonly written in state variable form. The n number of state variables, or states, of the system at time t are denoted as

$$x_1(t), x_2(t), ..., x_n(t) \tag{14}$$

and the m number of control inputs, or control, at time t are

$$u_1(t), u_2(t), ..., u_m(t) \tag{15}$$

The system is then denoted as a set of n first order ODEs as shown below [33]

$$\begin{aligned}
\dot{x}_1(t) &= f_1(x_1(t), x_2(t), ..., x_n(t), u_1(t), u_2(t), ..., u_m(t), t) \\
\dot{x}_2(t) &= f_2(x_1(t), x_2(t), ..., x_n(t), u_1(t), u_2(t), ..., u_m(t), t) \\
&... \\
\dot{x}_n(t) &= f_n(x_1(t), x_2(t), ..., x_n(t), u_1(t), u_2(t), ..., u_m(t), t)
\end{aligned} \tag{16}$$

In compact notation, states and controls are compiled into vectors so the system dynamics can then be written as

$$\dot{\mathbf{x}}(t) = \mathbf{f}(\mathbf{x}(t), \mathbf{u}(t), t) \tag{17}$$

where any bold variables indicate vectors [33].

The second factor in the optimal control formulation is the physical constraints of the system [33]. Constraints are set on the states and control to enforce the dynamics and boundaries of the search space. Path constraints may consist of inequality or equality constraints depending on the variable and type of restriction being imposed on the system. Boundary conditions are set to limit the problem space on both the states and control. Boundaries reduce the search space required for the non-linear programming (NLP) solver and can aid in convergence on a solution. Together, constraints result in an admissible control and an admissible trajectory.

The third factor in the problem formulation is the performance measure, also referred to as a cost function or objective function (J) [33]. A performance measure

provides the ability to quantitatively assess a system's performance designed to a specific performance measure [33]. Performance measures are chosen either by necessity from the problem or subjectively by the researcher [33].

$$J = \phi(\mathbf{x}(t_f), t_f) + \int_{t_0}^{t_f} L(\mathbf{x}(t), \mathbf{u}(t), t)dt \tag{18}$$

The generic formulation of a cost function is given in Equation (18) where t_0 and t_f are the initial and final times, ϕ is the terminal cost at the boundary, and L, also referred to as the Lagrangian, is the running cost which incurs a value at each time step [33]. Depending on the objective of the problem or the preference of the user, the performance index can be expressed in three different forms. The Mayer form only involves a terminal cost, while the Lagrange form only has the running cost, and the Bolza form includes both a terminal and running cost [34]. Equation (18) is written in Bolza form. There is no correct form of a cost function.

$$\min_{u* \in U} J = t_f \tag{19}$$

$$\min_{u* \in U} J = -\int_{t_0}^{t_f} V dt \tag{20}$$

Examples of common cost functions for hypersonic trajectory optimization problems are final time [16] as shown in Equation (19) in Mayer form, minimizing energy, maximizing terminal velocity [20], or maximizing range [14] as shown in Equation (20) in Lagrange form.

To explicitly define a generic optimal control problem: The goal is to find an admissible control (u) that will cause the system to follow an admissible trajectory (x) which minimizes the cost function when input into the system of ODEs [33]. When this is true u and x are defined as the optimal control and the optimal trajectory,

respectively defined as $u*$ and $x*$. Due to the nature of non-linear problem solutions, it may not be possible to guarantee that $x*$ and $u*$ provide the global optimal solution. The problem solution will converge to a local minimum. However, uniqueness is not guaranteed and other solutions may be found when the initial guess on the states and control are modified. Limiting the scope and range of admissible solutions can be done by subjecting the system and problem to equality constraints, inequality constraints, and boundary conditions [33].

Given the state dynamics, control, cost function, and constraints, many methods exist that are used to solve optimal control problems which can be split into two categories: indirect and direct. Indirect methods require the derivation of a Hamiltonian Boundary-Value problem from the theory of calculus of variations which requires the derivation of first and second-order optimality conditions. For analytical solutions, often times these are systems of nonlinear differential equations and solving the necessary conditions becomes very complicated, if even possible. Direct methods are an approximation of the optimal control problem by parameterizing the states and control using function approximations. The problem is converted to a nonlinear programming (NLP) problem and can be fed into a NLP solver.

Figure 9 summarizes the process of indirect and direct methods. While it is possible to use indirect methods as shown by Grant [20], direct methods are strongly preferred for complicated problems as they take advantage of linear analysis through Gaussian quadrature and polynomial approximation [14].

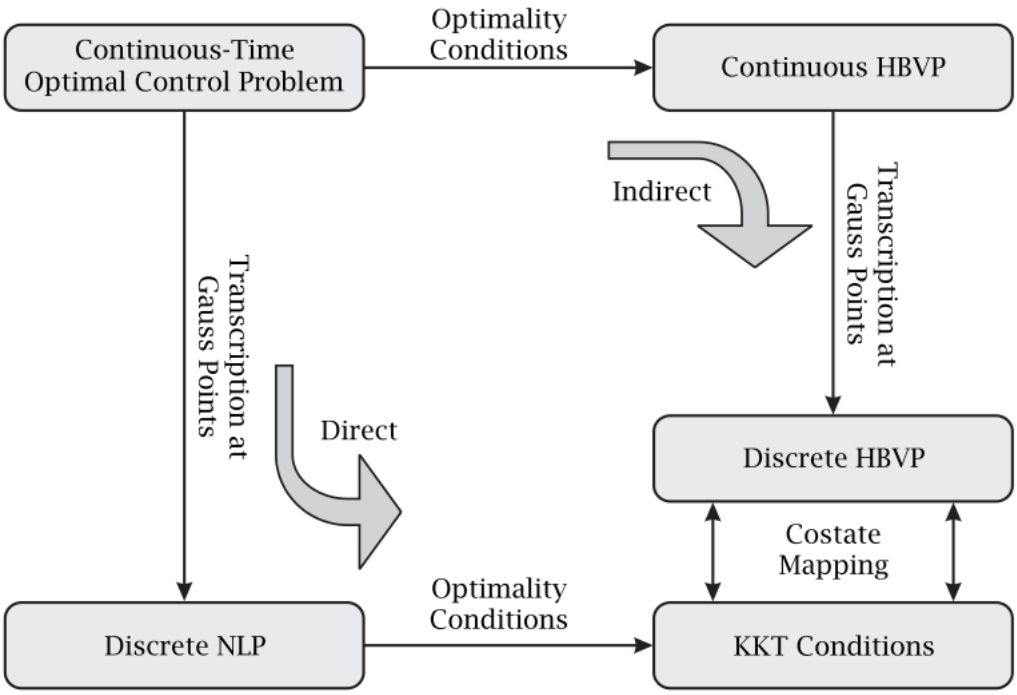

Figure 9. Indirect methods vs direct methods [35].

Direct methods are advantageous due to the ability to apply phases to the problem and the meshing that can occur in the solution. A phased solution can be obtained by formulating the problem into two or more separate, but connected, optimal control problems when the constraints or system dynamics do not have the same definition across the admissible solution space. In other words, a phased solution is essentially a sequence of single-phase optimal control problems that would collectively span the entire problem space [14]. Phases do not need to necessarily be linked sequentially, but still need to relate, as shown in Figure 10. In other words, one phase can be linked to more than just one, sequential phase. More on linking phases can be found in [36].

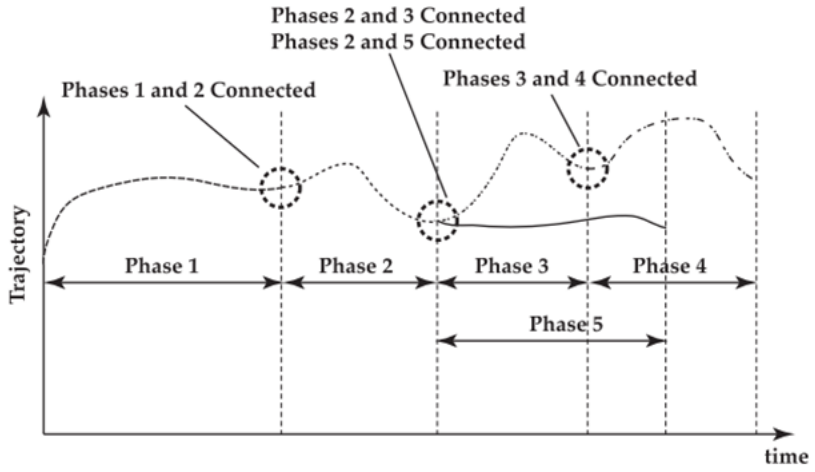

Figure 10. Schematic of phase linkages in a multi-phase optimal control problem [37].

2.4.2 Direct Collocation Methods

Direct collocation methods use the roots of orthogonal polynomials to define the collocation points where a solution to the optimal control problem will be found. The position of collocation points are important to achieving an accurate solution. Previous research has shown that when collocation points are equally spaced, which is the simplest configuration, the polynomial interpolation leads to large errors as the number of collocation points is increased, specifically at endpoints. This exasperated error at the endpoints is referred to as the Runge Phenomenon, as shown in Figure 11.

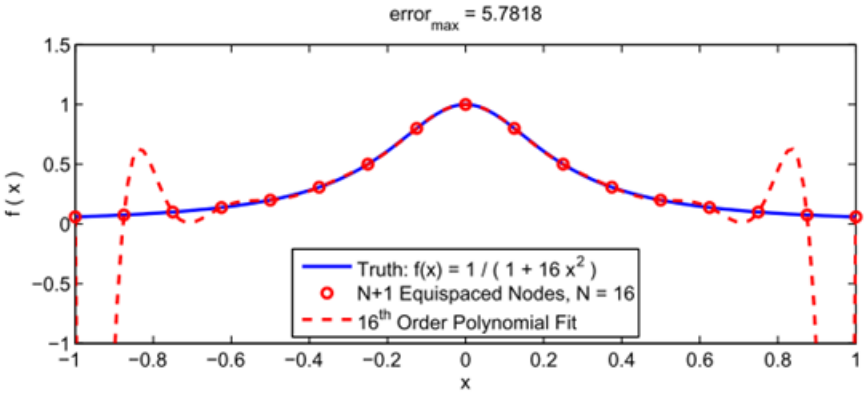

Figure 11. Runge Phenomenon with evenly spaced collocation points [12].

There are three different methods discussed herein for collocation point selection: Legendre-Guass (LG), Lengendre-Gauss-Radau (LGR), and Legendre-Guass-Lobatto (LGL). Figure 12 visually demonstrates the difference between the three collocation methods where the selection is based on which endpoint(s), if any, are included. The choice will affect how the continuity of boundary conditions are met with numerical methods and the "maximum order for high-order polynomials to still obtain an exact result in Gaussian quadrature" [14]. Since Lagrange polynomials are orthogonal, meaning they are easily integrated or differentiated, they can be "invoked at the collocation points to minimize integration errors" [14].

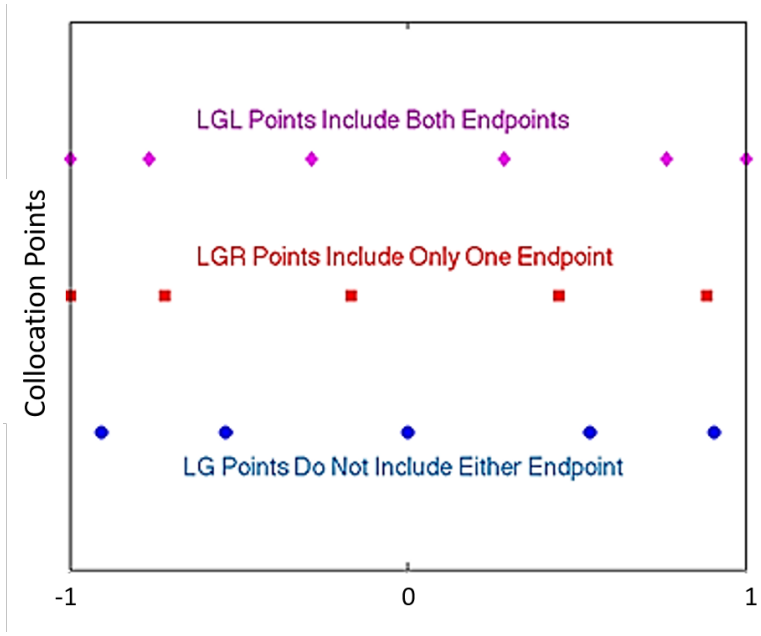

Figure 12. Pseudospectral collocation point selection methods [37].

A few software packages exist that implement a mesh on the solution when solving with direct orthogonal collocation methods. Betts demonstrated that a mesh is developed to decrease the error on the solution by changing the order of the polynomial approximation of the solution, p method, or by increasing the number of intervals in the solution space, h method [34]. Originally, direct collocation methods were developed as h methods (e.g., Euler or Runge-Kutta methods) where the time interval

is divided into a mesh and the state is approximated using the same fixed-degree polynomial in each mesh interval [37]. Software has evolved since to include both p and h methods.

2.4.3 GPOPS-II

Starting near the turn of the century, direct collocation methods gained traction as the preferred method for solving numerical solutions to nonlinear optimal control problems [37]. The solver being used for this research is GPOPS-II. It was created by Patterson and Rao and employs direct orthogonal collocation techniques [37]. GPOPS-II specifically uses the variable-order Gaussian quadrature collocation method that is a PS method of orthogonal basis functions [37].

GPOPS-II meshing utilizes a hybrid method called hp-adaptive Gaussian quadrature collocation method which allows a specific accuracy of numerical approximation to be achieved by either varying the number of points or the degree of the polynomial with each mesh iteration. Therefore, it can capitalize on the exponential rate of convergence for smooth sections of the solution and only increase the number of points in areas of rapid changes due to non-linearities. The largest advantage for the hp-adaptive method is the "significantly smaller finite-dimensional approximation" of the solution [37]. Additionally, since the hp-adaptive method is a direct method, it converts the assumed continuous time problem to a non-linear programming (NLP) problem.

GPOPS-II has two NLP solvers available to the user: interior point optimizer (IPOPT) which uses an interior-point line-search filter method or sparse nonlinear optimizer (SNOPT) which uses a sequential quadratic programming algorithm. GPOPS-II no longer updates or supports SNOPT [37]. GPOPS-II uses the LGR collocation method with the option of differential or implicit integral form. LGR is

chosen by the authors based on their reasoning that "it provides highly accurate state, control, and costate approximations while maintaining a relatively low-dimensional approximation of the continuous-time problem" [37].

Figure 13 summarizes the operations [37]. The user will input an optimal control problem into GPOPS-II and define all the bounds, variables, constraints, etc. The problem is then scaled automatically, per user settings, by calling an optimal control problem scaling algorithm. The scale factors resulting from the scaling algorithm are also used for the NLP. The optimal control problem is then transcribed to an NLP and solved on the initial mesh with an NLP solver (usually, either IPOPT or SNOPT). The NLP approximation is transcribed back into a discrete approximation and the error is estimated. If the error is larger than the user defined tolerance, the process repeats with a new mesh. Otherwise, the program terminates and outputs the solution [37].

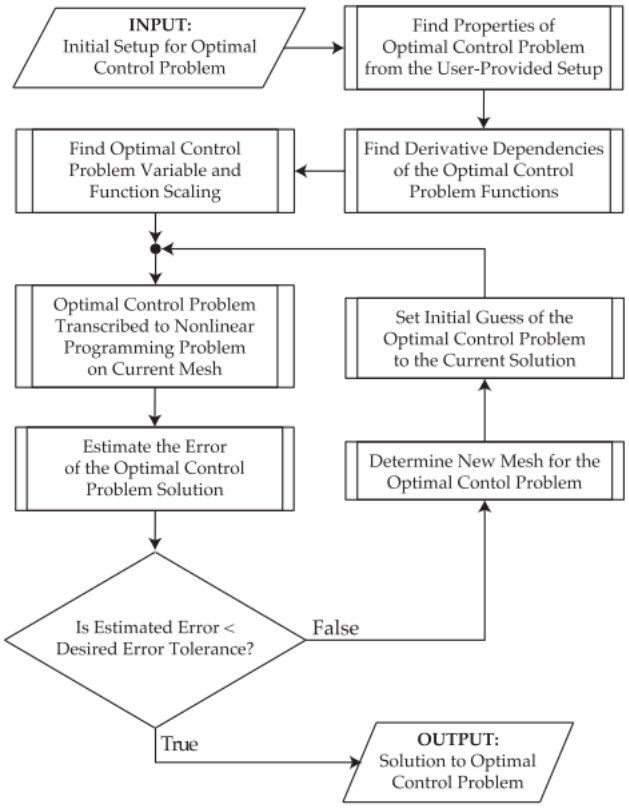

Figure 13. Flow chart of GPOPS operations [37].

2.5 Previous Work

The hypersonic field experienced a resurgence of research around the 2010s. During this time, optimization software and algorithms were also being developed. Trajectory optimization of hypersonic vehicles came into its own research topic to compliment the design process of new hypersonic technologies. This section will discuss some of the relevant research that has been accomplished so far. The compilation of previous projects will provide context for the current study.

Jorris' research objective was to design an optimal reentry trajectory of the Common Aero Vehicle (CAV) that would minimize flight time [12]. The trajectory was also subject to waypoint, no-fly zone, heating, and dynamic pressure constraints. Jorris used the GPOPS algorithm, a psuedospectral optimization technique, to ac-

complish this project implementing 3DOF vehicle dynamics to model a generic HCV and HGV. The HGV vehicle model used was the CAV. The generic HCV included a thrust component calculated to maintain a constant altitude. This simplified the problem and allowed for the use of two dimensional equations. The HGV modeled with the CAV had no thrust. However, it was a more complicated three dimensional (3D) problem. While both had bank angle as the control, the HCV had a normalized bank angle between positive and negative 20 degrees and the CAV had bank angle bound between positive and negative 60 degrees. The lift coefficient was normalized and limited at 2, derived from aerodynamic data tables. The solution was calculated with various methods. A suboptimal baseline trajectory was calculated using bang-level-bang control. Additionally, optimal trajectories via geometric and analytical methods were found for the two dimensional problem set ups. Both optimal solutions, via geometric and analytical methods, were very similar to each other and showed a clear improvement from the baseline technique with minimized flight time among other parameters. Numerical solutions found via the GPOPS algorithm for both the two and three dimensional problems were validated against the analytical solutions as shown in Figure 14 and Figure 15, respectively. The results between the numerical and analytical solutions were approximately equal.

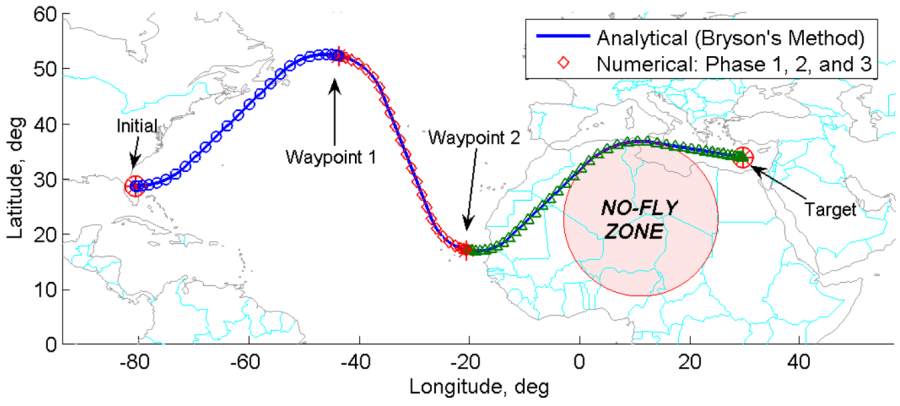

Figure 14. 2D analytical solution using Bryson's method and 3D CAV numerical solution [12].

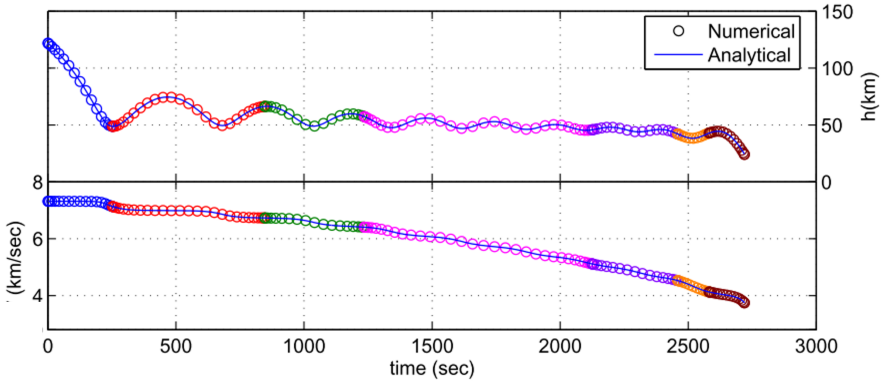

Figure 15. 3D analytical and numerical seven phase solutions [12].

The overall contribution from Jorris' research validated the direct numerical solutions provided by a then-new optimization technique, via GPOPS code, as well as demonstrating efficient user implementation with arbitrary phases, waypoints, and constraints. Follow on from Jorris was work by Karasz in 2008 [38]. He expanded on Jorris' solutions to include an analysis of sensitivity to additional waypoint locations as well as incorporating a slightly higher fidelity model by including the Earth's rotation and 3-dimensional spherical shape in the system dynamics. Karasz ran into days long computation times for convergence. Reducing computation time in addition to incorporating path constraints was recommended. Another suggestion was to attempt "an exercise in applying corrections on top of corrections" [38]. Essentially, Karasz was recommending the process of continuation.

Jorris was involved in research published by Rexius et al. in 2013 along with Anil Rao, one of the GPOPS creators [24]. Their research aimed to fulfill the need of creating optimal flight test trajectories for HGV programs. Jorris' previous work demonstrated the ability of pseudospectral optimal control to find reentry trajectories for the CAV model while including constraints like waypoints, no-fly zones, and aerodynamic heating path constraints [12]. Rexius et al. presented "the implementation of multiple complex models representing a three-stage booster and a hypersonic glide

vehicle (HGV) similar to the CAV within the GPOPS framework" [24]. The problem formulation included constraints on the aerodynamics, aerothermodynamics, aircraft stability, vehicle loads, and the inclusion of no-fly zones. Furthermore, the effect on the aerothermodynamics of three different guidance methodologies were compared. The glide portion of the flight path was split into six phases. The cost function, in mayer form, was set to minimize the stagnation point heat rate, calculated by the Chapman equation, at the end of the first glide phase, defined as the moment "when there is sufficient lift on the glide vehicle to zero the flight path angle," [24]. Aerodynamic look-up tables were utilized and fitted with polynomial interpolation equations. Results focused on the effects of the chosen cost function, constraints, and glide phase guidance methodologies. Results compared the GPOPS optimal solution to the "original" optimal solution. The "original" optimal solution is never explicitly defined by the authors, however, the problem formulation can be assumed unconstrained. The cost function of the "original" solution is undetermined, unless the reader wants to assume it was the same as Jorris' previous work as minimum flight time. The chosen cost function affected the boost profile to reduce the separation altitude by approximately 30 percent as shown in Figure 16. The GPOPS solution with a cost function designed to minimize heat rate reduced the maximum heat rate by approximately 20 percent when compared to the original solution shown in Figure 17.

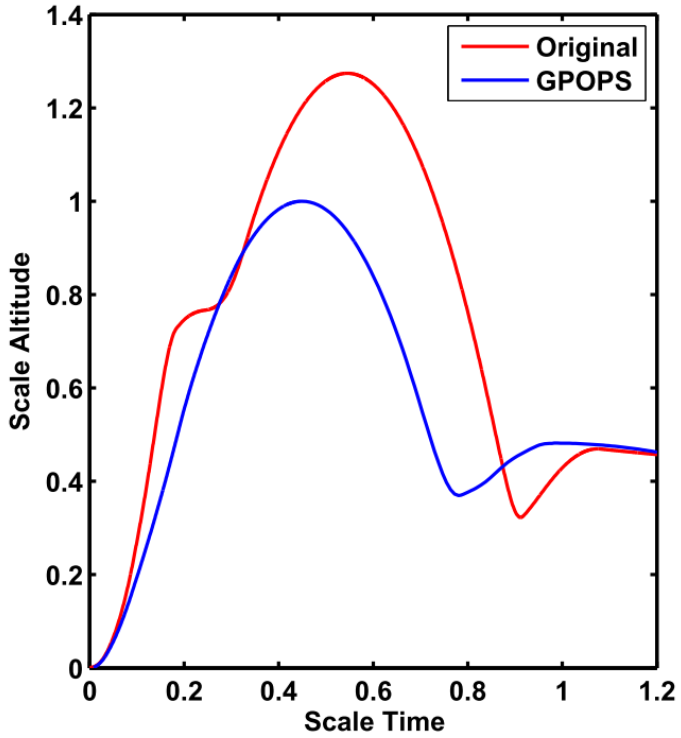

Figure 16. Boost and HGV re-entry altitude profile comparison of the original optimal solution in red vs with the chosen cost function in blue [24].

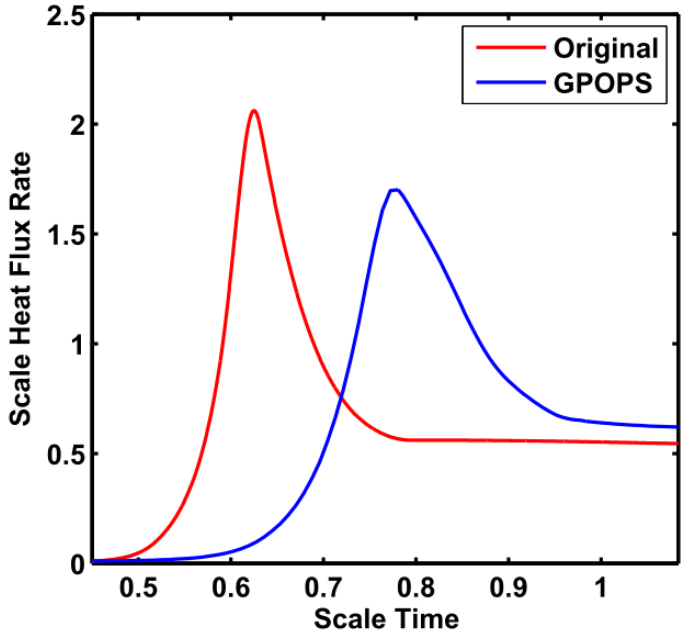

Figure 17. HGV stagnation heat rate comparison calculated with the Chapman equation [24].

One of the largest takeaways from the research was the conclusion that prioritization of the lowest heat rate, but not necessarily the lowest heat load, may be more favorable for an HGV. However, the authors also caveat this recommendation with the recognition of the influence of other important factors or missions. Rexius et al. also noticed challenges with implementing complex aerodynamic tables that result in non-smooth derivatives as well as GPOPS method for auto-scaling. The authors found the internal scaling features of GPOPS to be very sensitive to convergence on a solution with small scaling changes or excessive bounds on the states and control meaning the difference between convergence or not. The recommended remedy to the scaling challenge was either implementing a user-defined auto scaling function or non-dimensionalization. Future work looked to tackle some of their challenges as well as expand research with more cost functions and guidance methodologies.

In 2014, research by Masternak was published in his PhD dissertation with a goal of developing a tool and methodology to generate optimal hypersonic trajectories via optimal control formulation incorporating various path constraints including a heating constraint [14]. An air-breathing hypersonic aircraft with a scram jet was modeled using traditional 3DOF equations of motion and a simple one-dimensional thrust equation for the propulsion system. Thrust and other aerodynamic values were found through aerodynamic look up tables of empirical data for the Generic Hypersonic Aerodynamic Model Example (GHAME). The Chapman model and the NASA MINIVER heating model, a medium fidelity model, were used for calculating the heat rates. Additional path constraints on waypoints, g-limits, and no fly zones were included. Angle of attack, roll angle, and propellant mass flow rate were used as the controls. For a different cost function which included a control penalty, the controls were then angular rates of angle of attack rate, roll angle rate, and propellant mass flow rate. A table of Masternak's various mission formulations is shown in

Figure 18.

Formulation Attributes		Sec 5.2.1	Sec 5.2.2	Sec 5.2.3	Sec 5.2.4	Sec 5.2.5	Sec 5.2.6	Sec 5.2.7	Sec 5.2.8	Sec 5.2.9	Sec 5.2.10
OBJECTIVE FUNCTION	Maximum Range	x									
	Minimum Time		x		x					x	
	Minimum Time with Control Penalty			x		x	x	x	x		x
BOUNDARY CONDITIONS	Start Fixed (Takeoff)	x	x	x	x	x	x	x	x	x	x
	End Variable (Overflight)	x									
	End Fixed (Overflight)		x	x					x	x	
	End Fixed (Landing)				x	x	x	x			x
	Waypoint Variable (Refuel)						x	x	x		x
	Waypoint Variable (sensor on)								x		
PATH CONSTRAINTS	Fuel-Air Ratio	x	x	x	x	x	x	x	x	x	x
	Dynamic Pressure	x	x	x	x	x	x	x	x	x	x
	Mach Number									x	
	g-limits							x			
	No-fly zone							x	x		
	Sensor								x		
	Temperature									x	x

Figure 18. Masternak's research scenario attributes [14].

Overall the results proved the ability of using GPOPS-II to generate multiple optimal trajectories for an air breathing vehicle with various mission priorities and path constraints fairly rapidly. Figure 19 shows the altitude and velocity profiles of the trajectory. Masternak added a caveat that lengthy run times could be expected for most stressing scenarios.

Moving forward, Masternak discussed implementing higher fidelity models for the vehicle, i.e. 6 DOF EOMs, the aerothermal model, and better propulsion models especially for the transition phase from turbine to ramjet to scramjet. He also recommended against using NASA's MINIVER aerothermal model due to its incompatibility with MATLAB and consequently, GPOPS-II. Masternak's research is relevant

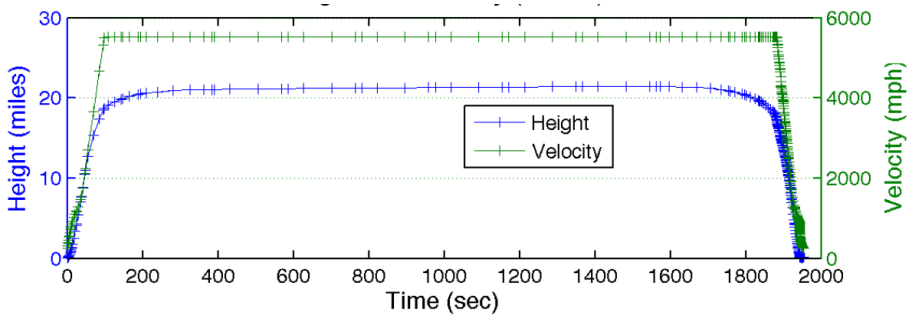

Figure 19. Altitude and velocity of optimal trajectory of minimum time with climb, cruise, and land [14].

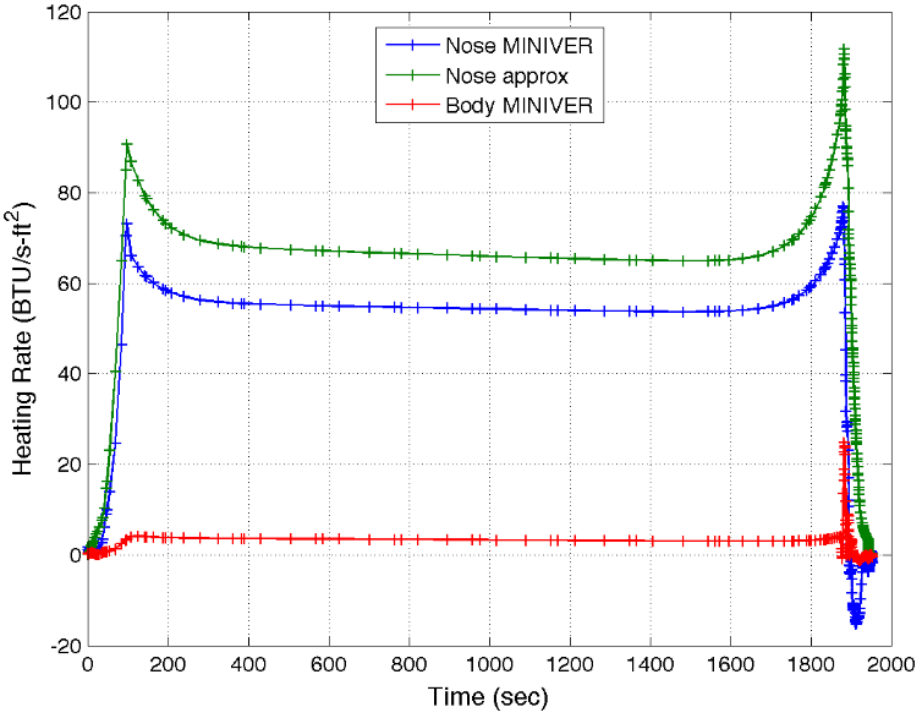

Figure 20. Heating rates of optimal trajectory of minimum time with climb, cruise, and land [14].

to this research due to the similarities in goals. While certain specifics of the two projects may be different, Masternak's results develop intuition.

In 2015, a paper was published by Rizvi et al. on determining the optimal burnout conditions for a hypersonic boost-glide vehicle trajectory and conducting a heat load analysis of various vehicles [9]. Three different vehicle shapes, listed in descending order of lift-to-drag ratios in the hypersonic regime, were compared: a waverider similar to DARPA's X-41 CAV, a wing-body configuration, and a lifting-body design. The waverider configuration has the ability of a trim L/D ratio above 3 at hypersonic speeds. A wing-body shape gets a trim L/D above 2 and a lifting-body design gets slightly above one. The problem formulation was very similar to the set-up of this research effort with three degree of freedom equations of motion, assumptions of a spherical, non-rotating Earth, and a focus on the reentry glide phase of flight. Lift and drag coefficients for each vehicle used curve-fitted equations from aerodynamic data and assumed to be functions of angle of attack only. Initial conditions were specified for a missile launch pad, since the boost phase was included in simulations. The burnout velocity of the two stage rocket was around 3.7 km/s. The burnout velocity was applied to all vehicle simulations. Final conditions were based off traditional penetration requirements of a conventional warhead. Therefore, a final vehicle radius, speed, and flight path angle were defined. Path constraints on the system were the stagnation point heating rate calculated from an equation given by Scott et al. [39] in Equation (21), extremely similar to the Chapman model, and dynamic pressure.

$$\dot{Q} = C\rho^{0.5}V^{3.05} \tag{21}$$

In Equation (21), the heat rate is $\dot{Q}$, ρ is density, and V is the velocity. C is a proportionality constant, which is based on the nose radius and vehicle material. The maximum heating rate $\dot{Q}_{max}$ constraint was determined to be 4 MW/m^2 from

the maximum temperature of around 2900 K at which a carbon-carbon composite material can retain its properties [9].

$$T_w = \left(\frac{\dot{Q}}{\sigma \epsilon_{TH}} \right)^{\frac{1}{4}} \tag{22}$$

Assuming the surrounding are in radiative equilibrium, the vehicle surface temperature can be linked directly to the heating rate with Equation (22), known as the Stefan-Boltzmann Law [18], where the gas temperature T_g is much less than the wall temperature T_w [40]. The Stefan-Boltzmann constant, σ is 5.67e-8 $\frac{W}{m^2 K^4}$ and surface emissivity, ϵ, is estimated at 0.8. A table from Rizvi et al. shows some of the linked values between a maximum heating rate and a maximum temperature [40]. The dynamic pressure constraint was calculated from the terminal conditions.

Table 2. Maximum temperature values corresponding to the maximum heat rate limits [40].

$\dot{Q}_{max}$	T_{max}
(MW/m^2)	$(^\circ C)$
3.5	2,690
3.0	2,580
2.5	2,450
2.0	2,305
1.5	2,125
1.0	1,895

Heat load was calculated via the integration of heat rate. Controls for the vehicles were bank angle and angle of attack. The cost functions were maximizing down-range and cross-range, equivalent to maximizing the final longitude and latitude, respectively. The researchers also used hp-adaptive pseudospectral methods via the GPOPS-II software. Previous studies by Rizvi et al. "showed that the integrated heat load can be reduced by as much as 50 percent with a penalty of only 10 percent in the overall down-range" [9]. Results discussed the optimal burnout conditions and trajectories for each vehicle for a medium range application. Medium range

was considered to be around 2,000 km. Optimal trajectories, with optimal burnout conditions were found for the waverider while meeting all path constraints. Both the down-range and cross-range of the waverider configuration were higher than the other configurations. The integrated heat load for the waverider configuration was found to be approximately five times higher than a wing-body configuration and an order of magnitude higher than the lifting body configuration. The heat load was found to increase exponentially with lift-to-drag ratio due to the increased flight time as shown in Figure 21.

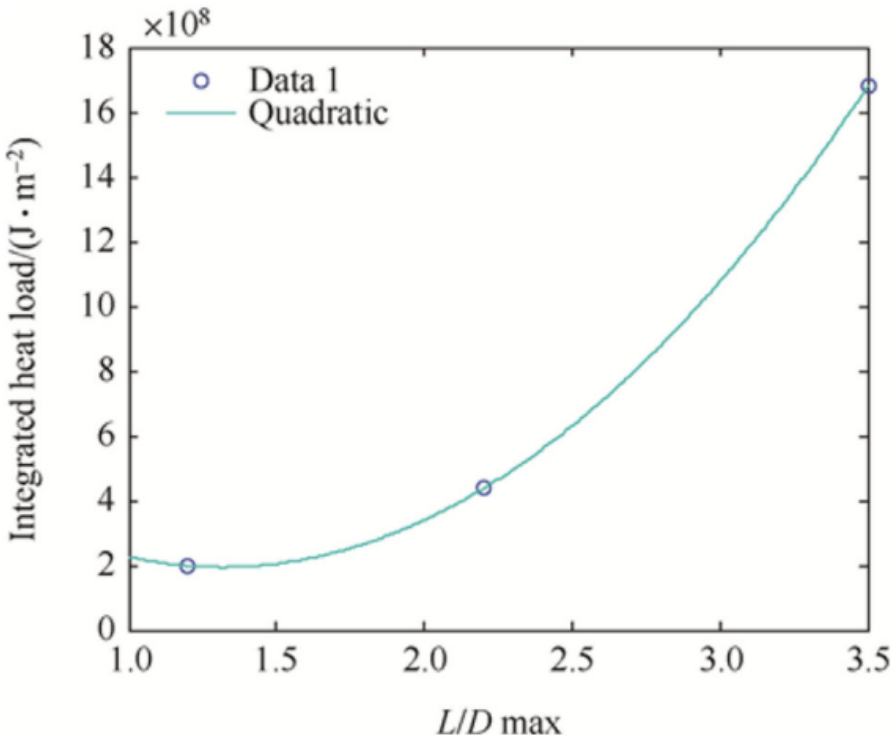

Figure 21. Integrated heat load vs lift-to-drag ratio with a burn out speed of 3.7 km/s and a down range of 1,600 km [9].

In a 2019 paper published by Hood et al., research was conducted on rapid hypersonic trajectory optimization comparing convergence speeds between various model fidelities [13]. The system dynamics were represented with 3DOF equations with the assumptions of a non-rotating Earth and no thrust to model an HGV. The vehicle

model of the HGV was a modified X-43 accompanied by aerodynamic look up tables. Two key results were established: "First, we discovered that aerodynamic surrogates facilitate convergence for a pseudospectral optimizer, and thus allow for a much more accurate solution with a small increase in computation time" and "noted the importance of considering additional vehicle constraints based on behavior demonstrated in a higher fidelity simulation when writing optimization algorithms that employ a lower-fidelity model."

Corey Lee's research in 2020 accomplished solving for HGV optimal trajectories using reinforcement learning through artificial intelligence (AI) [41]. The AI was able to generate trajectories for both a two dimensional and three dimensional (3D) problem set up using 3DOF reentry equations of motion to model the system dynamics. The trajectories were subject to various constraints, including acceleration, heating, and dynamic pressure. The AI solutions were validated against GPOPS-II code. However, the AI did not produce converged results. Lee explains that "convergence [of AI] would take weeks." Therefore, the AI solution cannot be confirmed to be the optimal solution. For the three dimensional GPOPS-II solution, a convergence was not pursued because it was determined that a better initial guess is required, which was outside the scope of the project. This research will share similarities with Lee's project in terms of the project goal in generating trajectories, with the difference of achieving convergence via GPOPS-II instead of AI. The issue that Lee ran into of needing a better initial guess will be addressed with the method of continuation. Continuation inherently will provide more sophisticated guesses with each iteration.

More recently published is research by Coulter et al. in 2021 [16]. Coulter's paper presented preliminary results that proved the feasibility of the proposed approach to incorporating high-fidelity aerothermodynamic models with hypersonic trajectory optimization. An unpowered X-43 without fins was used as the generic hypersonic

vehicle model. One of the goals the researchers set out to prove was the ability to calculate aerodynamic values in lieu of relying on aerodynamic tables which are costly or computationally time consuming. L/D values were generated using an in-house Modified Newtonian Theory (MNT) code to calculate the pressure on each panel and use it to solve for lift and drag. The L/D values qualitatively matched X-43 data. The aerodynamic values were used to calculate the heat rate via Eckert's Reference Enthalpy Method. Two simulations were run on GPOPS-II code both with and without path constraints on heat rate, normal load, and dynamic pressure. The equations of motions were dimensionless, which significantly reduced the challenge of scaling in GPOPS-II. While non-dimensionalizing may be convenient, it can quickly become laborious when continuously changing or appending new additions to the current problem formulation. The cost function was aimed at maximizing the cross range, i.e. maximum latitude. While both time based and energy based approaches were discussed, results were only presented from the energy based approach. The results demonstrated the effectiveness of the researcher's proposed method of "combining the [MNT] and Eckert's reference enthalpy method with a pseudospectral optimal control method" [16]. The optimal heat rate profile calculated with Eckert's reference enthalpy method is shown in Figure 22. The heat rate was set as a path constraint with a maximum value of 7.5×10^6 W/m^2. Coulter and colleagues stated that their future work will look to match the dynamic pressure and g-loading models' fidelity to that of the heat rate model. Additionally, research will aim to increase the vehicle model fidelity and incorporate a CFD solver [16].

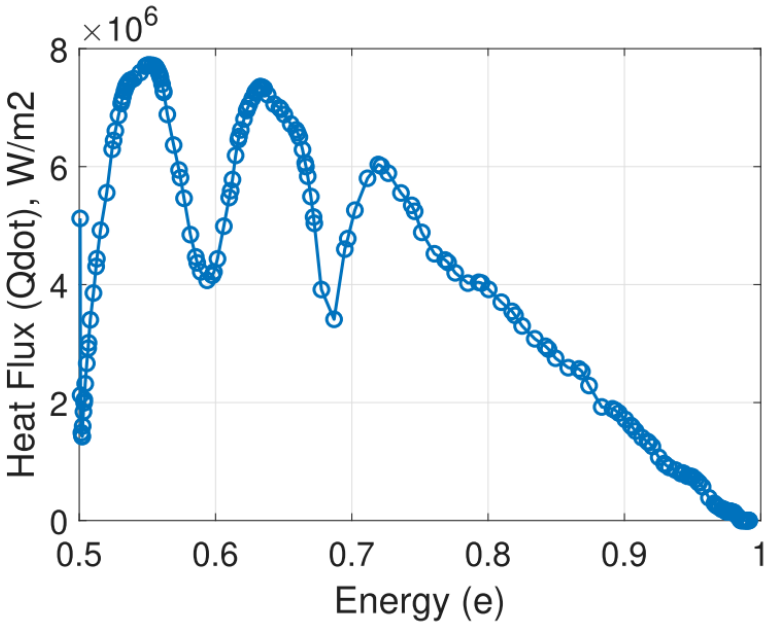

Figure 22. Optimal heat rate profile [16].

2.6 Overview

The research effort herein is based off the knowledge and tools discussed throughout this chapter. The hypersonic trajectory optimization problem is a revived and growing field of research. Commissioned by AFRL to solve an open ended problem allowed for the flexibility to try a new methodology via the process of continuation, further discussed in Chapter III. Continuation is the attempted solution for the challenge encountered by Lee [41] of convergence issues with GPOPS-II code likely due to the seed solution provided. From the literature review conducted by this author, the current research effort is the first effort of implementing continuation for a hypersonic trajectory optimization problem. While the literature review may not be all encompassing, additions to the field of hypersonic research are valued by the scientific community and a national priority [2].

III. Methodology

This chapter is divided into two sections, with each corresponding to the research objectives underpinning this thesis. Specifically, the first section corresponds to the first research objective of utilizing the continuation process for solving a complicated problem formulation. The second section focuses on the comparison of aerothermodynamic models solved via the continuation method.

3.1 The Process of Continuation

The hypersonic trajectory optimization problem was solved via direct orthogonal collocation methods utilizing the GPOPS-II algorithm while implementing the method of continuation. The first research objective focuses on solving an optimal trajectory for maximizing the range of a hypersonic glide vehicle (HGV) during its glide phase. The characteristics of the chosen vehicle model are utilized in the equations of motion (EOMs) to provide a more realistic solution. Incorporation of vehicle characteristics increases the fidelity of the model. For example, calculating lift and drag require the area of the vehicle. A generic glide vehicle was modeled where the vehicle's properties were based on the Common Aero Vehicle [32] and typical lifting body values. A second HGV was also modeled after the High-speed Army Reference Vehicle (HARV) [5]. The HARV was chosen because it was created with the mission of providing a model "suitable for foundational research to allow for focused collaboration" [5]. Due to the adaptable nature of the HARV, no aerodynamic tables are provided with the model. Figure 8, as shown in Section 2.3, illustrates one possible configuration of the HARV with a conical nose and four tail fins.

$$g = g_0(\frac{R_e}{r})^2 \tag{23}$$

$$\rho = \rho_0 \exp^{-\beta(r-Re)} \tag{24}$$

$$L = \frac{C_L V^2 \rho S}{2} \tag{25}$$

$$D = \frac{C_D V^2 \rho S}{2} \tag{26}$$

Gravity was calculated as a function of the vehicle's radial position with Equation (23) while atmospheric density was calculated with a simple exponential relationship in Equation (24). Earth's gravitational constant is g_0 and defined as 9.8 m/s^2, R_e is the Earth's radius at 6371 km, ρ_0 is the density at sea level at 1.225 kg/m^3, β is a scale height set at 0.14, S is the wetted area of the vehicle, and V is the vehicle speed. Atmospheric density was calculated with an exponential model in Equation (24). The coefficients of lift and drag required for Equations 25 and 26 remained as constants. Lift and drag were calculated with Equations 25 and 26.

For the first few iterations of code using the CAV-inspired HGV model, the coefficient of lift was set to 2 and the coefficient of drag was set to 1. These values were chosen to represent a lifting body with a L/D that is greater than 1. The mass was set as 1000 kg and the wetted area, S, as 4.4 m^2. The HARV characteristics assumed a lift coefficient of 0.01 and a drag coefficient of 0.7 due to the vehicle configuration resembling a missile. These lift and drag values were chosen from common values of rocket missiles [42]. The mass was set to 150 kg and the wetted area as 2 m^2 [43]. The dynamics of the system are represented in the code with first order differential equations of motion.

3.1.1 Equations of Motion

The equations of motion are common trajectory reentry equations. The equations of motion were derived with the following assumptions: a constant Earth rotation ω, drag parallel and opposite to velocity, lift perpendicular to velocity, and the gravity vector parallel to the vehicle position vector. The vehicle is modeled as a pseudo-point mass. In a physical system, the coefficient of lift and drag would be based on the vehicle's orientation, however, inclusion of orientation based aerodynamic forces is beyond the scope of the current investigation. The vehicle was assumed to have no thrust representing the glide phase of an HGV. The rotation of the Earth was assumed to be negligible. Neglecting Earth's rotation is valid due to the difference in relative speeds between a hypersonic vehicle and the Earth's rotation. The simplified 3D state dynamics are as follows [44]:

$$\dot{r} = V\sin(\gamma) \tag{27a}$$

$$\dot{\theta} = \frac{V\cos(\gamma)\cos(\psi)}{r\cos(\phi)} \tag{27b}$$

$$\dot{\phi} = \frac{V\cos(\gamma)\sin(\psi)}{r} \tag{27c}$$

$$\dot{V} = -\frac{D}{m} - g\sin(\gamma) \tag{27d}$$

$$\dot{\gamma} = \frac{L}{Vm}\cos(\sigma) - \frac{g}{V}\cos(\gamma) + \frac{V}{r}\cos(\gamma) \tag{27e}$$

$$\dot{\psi} = \frac{L\sin(\sigma)}{m\cos(\gamma)V} - \frac{V}{r}\cos(\gamma)\cos(\psi)\tan(\phi) \tag{27f}$$

where the vehicle's position vector is r, longitude is θ, latitude is ϕ, speed is V, flight path angle is γ, and heading angle is ψ. The bank angle is defined as σ. The EOMs presented are three degree of freedom equations that model vehicle trajectories in either endo- or exo-atmospheric environments.

3.1.2 Continuation

Continuation is the method of solving a less complex problem and using its solution to seed a more complicated problem, then using the subsequent solution to seed an even more complicated problem. The process is repeated until a solution is found for the problem at the desired level of complexity. Continuation is beneficial for hypersonic trajectory optimization as complexities can be slowly added into the problem formulation while maintaining tractable solutions.

Figure 23 shows an overview of the continuation process with the bold yellow text highlighting the changes between each step. The initial seed fed into the first round of GPOPS-II code was a Fourth-Order Runge-Kutta (RK4) solution for the generic hypersonic vehicle, labeled as "Step 0" in Figure 23. The RK4 method is an iterative method that generates approximate solutions to ordinary differential equations. The RK4 solution was used as the initial seed due to the method's simple propagation of dynamic equations without a cost function, bounds on parameters, path constraints, or any other limitations. The solution of the first set of GPOPS-II code, referred to as the GPOPS code-1 and labeled as "Step 1" in the flowchart, was used to seed the next iteration of the optimal solution. The second iteration of GPOPS-II code, which also used the generic hypersonic vehicle characteristic data, is referred to as GPOPS code-2 and labeled "Step 2" in the flowchart. The next iteration of GPOPS-II code, "Step 3", used HARV characteristic data and is referred to as GPOPS HARV. The specifics of the GPOPS-II codes are covered in the following section on Problem Formulation.

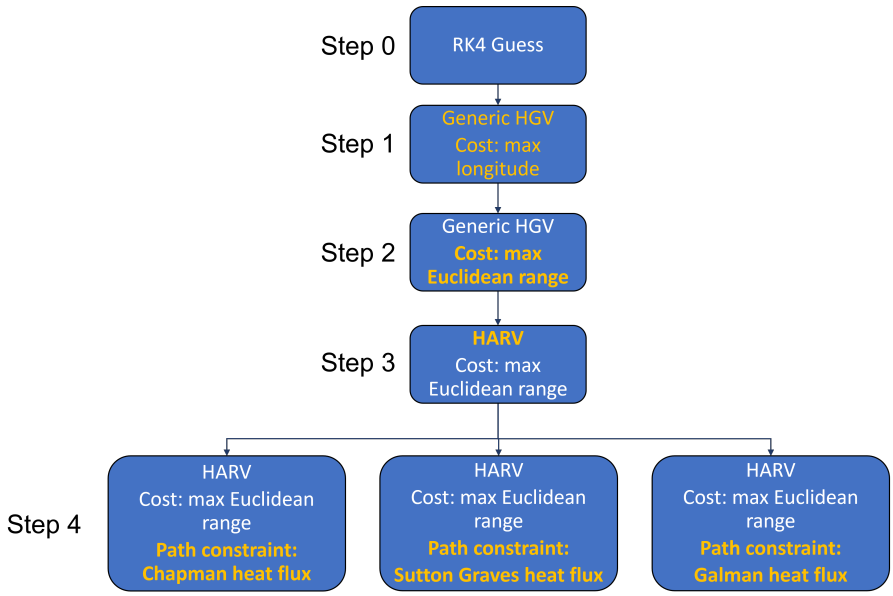

Figure 23. An overview of the continuation process.

3.1.3 Problem Formulation

The generic optimal control problem formulation consists of a system modelled with ordinary differential equations (ODEs), bounds, and a cost function. A cost function, or performance measure, provides the ability to quantitatively assess a system's performance with respect to a specific performance measure [33]. The goal of an optimization problem is to find the control that will minimize or maximize the performance index.

Both GPOPS code-1 and GPOPS code-2 had the same dynamics and vehicle model. The system was modeled with three-dimensional three degree of freedom (3D 3DOF) EOMs. The states ($\mathbf{x}$) were vehicle position, measured from the center of the Earth, latitude, longitude, speed, flight path angle, and heading angle. The state derivatives were described in Equations 27a through 27f.

$$\mathbf{x} = \begin{bmatrix} r \\ \theta \\ \phi \\ V \\ \gamma \\ \psi \end{bmatrix} \tag{28}$$

The control ($\mathbf{u}$) was bank angle.

$$\mathbf{u} = \sigma \tag{29}$$

Bounds on the variables in the code for GPOPS code-1 is summarized in Table 3 while Table 4 summarize bounds for GPOPS code-2 and HARV. The altitude bound is expressed through the vehicle position radius with the lower bound being the Earth's radius and the upper bound being the initial radius of the vehicle. For GPOPS code-1, the upper bound was 100km above the Earth's radius. Altitude, or vehicle position radius, was bound to the continuum flow region, assumed to be under 100 km in altitude, where lift and drag may be calculated using aerodynamic principles.

Table 3. Variable bounds for GPOPS code-1.

Variable	**Units**	**Min**	**Max**
Time (t)	seconds	0	7000
Vehicle position radius (r)	km	6371	6471
Speed (V)	km/s	0.01	8
Longitude (θ)	radian	-π	π
Latitude (ϕ)	radian	-$\pi/2$	$\pi/2$
Flight path angle (γ)	radian	-$\pi/2$	$\pi/2$
Heading angle (ψ)	radian	0	2π
Bank angle (σ)	radian	-$\pi/3$	$\pi/3$

The initial vehicle position radius for GPOPS code-1 converged upon 6437 km.

For GPOPS code-2 and GPOPS HARV, the initial vehicle position radius was fixed at the converged initial radius in GPOPS code-1 at 6437 km or 66 km in altitude.

Table 4. Variable bounds for GPOPS code-2 and HARV.

Variable	Units	Min	Max
Time (t)	seconds	0	7000
Vehicle position radius (r)	km	6371	6437
Speed (V)	km/s	0.01	8
Longitude (θ)	radian	-π	π
Latitude (ϕ)	radian	-$\pi/2$	$\pi/2$
Flight path angle (γ)	radian	-$\pi/2$	$\pi/2$
Heading angle (ψ)	radian	0	2π
Bank angle (σ)	radian	-$\pi/3$	$\pi/3$

The setup of all the GPOPS-II code iterations was configured with the setting options in Table 5. Details on the settings can be found in the GPOPS-II User Guide [36].

Table 5. GPOPS-II mesh and setup options.

Option	Setting
mesh.method	hp-PattersonRao
mesh.tolerance	1×10^{-4}
setup.nlp.solver	snopt
setup.scales.method	automatic-bounds
setup.method	RPM-Integration

The cost function of GPOPS code-1 was maximizing longitudinal range, as a converged solution could easily be obtained for the continuation process. This cost function was arbitrarily chosen as a starting point for the optimization algorithm. Longitudinal range can be found as a cost function in other literature [45][14] as

$$\min_{u* \in U} J = -\theta. \tag{30}$$

No path constraints were enforced during this iteration in Step 1. Table 6 shows the set up for the initial and final conditions in the problem for GPOPS code-1. The

initial vehicle radius, latitude, and longitude are left free to allow the algorithm to converge on an optimal starting position for the given cost function. The final latitude and longitude was set to the coordinates of the Kwajalein Atoll US military base in the Marshall Islands.

Table 6. Initial and final conditions for GPOPS code-1.

Variable	Units	Initial	Final
Time (t)	seconds	0	free
Vehicle position radius (r)	km	free	6381
Speed (V)	km/s	free	free
Longitude (θ)	radian	free	2.9274
Latitude (ϕ)	radian	free	0.1522
Flight path angle (γ)	radian	free	free
Heading angle (ψ)	radian	free	free
Bank angle (σ)	radian	free	free

$$\min_{u*\in U} J = -(x_2 - x_1)^2 + (y_2 - y_1)^2 + (z_2 - z_1)^2 \tag{31}$$

The cost function for GPOPS code-2, which used the solution from GPOPS code-1 as the initial seed, was maximizing the Euclidean range as shown in Equation (31).

$$x = r\cos(\phi)\cos(\theta) \tag{32}$$

$$y = r\cos(\phi)\sin(\theta) \tag{33}$$

$$z = r\sin(\phi) \tag{34}$$

The states were converted into the Cartesian plane with Equations 32-34 and a simple Euclidean distance was calculated for the cost function. The subscripts 1 and 2 denote initial and final positions, respectively. Although the Euclidean distance is not a realizable flight path, it is directly related to the true flight path as described by the system dynamics. In other words, even though the Euclidean range is not a feasible

flight path, the trajectory solution will be accurate since the system dynamics are not violated in the state solution.

For GPOPS code-2 and HARV iterations, in Steps 2 and 3 of Figure 23, no path constraints were enforced on the system. The initial and final conditions on the problem for GPOPS code-2 and GPOPS HARV are listed in Table 7. The problem was free final time, fixed final state, specifically fixing the final radial position, latitude, and longitude. Additionally, the initial radial position of GPOPS code-2 and GPOPS HARV was fixed based off the initial radial position of the GPOPS code-1 result which was 66 km above the Earth's surface.

Table 7. Initial and final conditions for GPOPS code-2 and HARV.

Variable	Units	Initial	Final
Time (t)	seconds	0	free
Vehicle position radius (r)	km	6437	6381
Speed (V)	km/s	free	free
Longitude (θ)	radian	free	2.9274
Latitude (ϕ)	radian	free	0.1522
Flight path angle (γ)	radian	free	free
Heading angle (ψ)	radian	free	free
Bank angle (σ)	radian	free	free

The goal was to find where the vehicle should start its glide phase to maximize range given a fixed initial altitude and still achieve the fixed final target. The fixed initial altitude was arbitrarily chosen as the mission scenario for this research effort.

3.2 Comparing Aerothermodynamic Models

The next step in the continuation process was to include a path constraint on the stagnation point heat rate calculated with different aerothermodynamic models for comparison. Three models of similar fidelity were compared: the Chapman model [6], the Sutton Graves model [7], and the Galman model [8]. Each model calculated the stagnation point heating rate at the nose throughout the flight path. The ef-

fective nose radius was 0.03 m. The aerothermodynamic models were set as path constraints in the system with a limit on the maximum heating rate. Figure 24 is a progression of Figure 23 which shows each iteration of the continuation process for the three aerothermodynamic models. Each iteration follows the same logic described in Section 3.1.2 where the solution of the previous step is the seed for the next step.

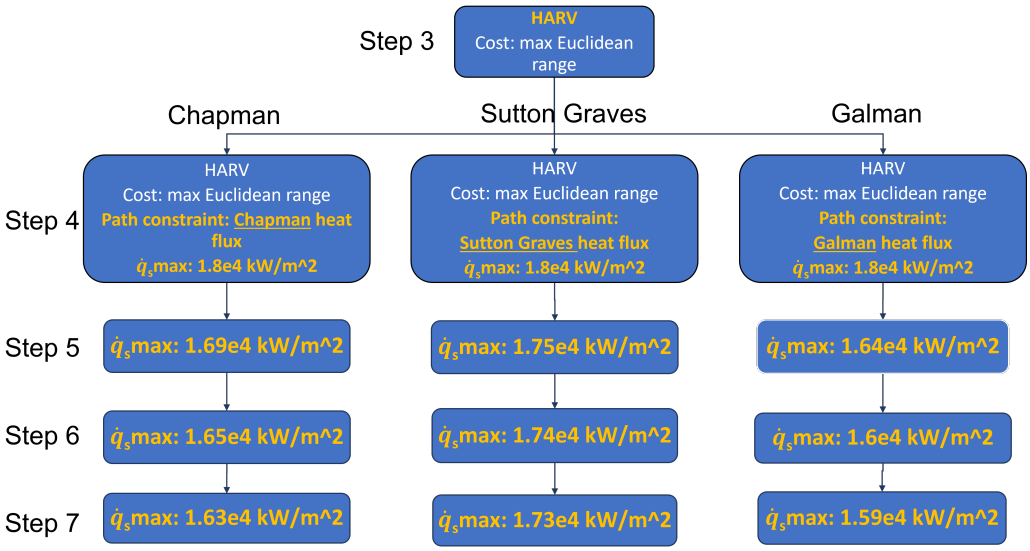

Figure 24. Flowchart of the continuation process with aerothermodynamic heating models.

The heating rate limit, $\dot{q}_s$max, for Step 4 was determined from calculating the heating rate profile from the GPOPS HARV solution in Step 3 with each method. The heating rate limits for Steps 5-7 varied across the different aerothermodynamic models according to the maximum value achieved from each model in Step 4. The GPOPS-II code and problem formulation for Steps 4-7 maintained the same variable bounds and set up as the GPOPS HARV code in Step 3, detailed in Section 3.1.3, with the addition of a path constraint. The lower bound for the path constraint on $\dot{q}_s$min was set at 0.01 kW/m^2. The upper bounds on $\dot{q}_s$max for each iteration in the continuation process can be found in Figure 24.

The generalized Chapman method calculates stagnation point heating rate with

Equation (35) where the blue term is the "hot wall correction" term and is frequently neglected in hypersonic flow due to the freestream enthalpy, h_∞, being much larger than the wall enthalpy ($h_\infty >> h_w$) [6] [18].

$$\dot{q_s} = \frac{C}{\sqrt{R_n}}(\rho_\infty)^m(V_\infty)^n\left(1 - \frac{h_w}{h_\infty}\right) \tag{35}$$

The constant, C, is derived for the problem and m and n are usually determined by the planet's atmosphere. The version of the Chapman equation commonly found in literature is Equation (36) without the hot wall correction term [18] [6].

$$\dot{q_s} = 1.63 \times 10^{-4}\left(\frac{\rho}{R_n}\right)^{\frac{1}{2}} V^3 \tag{36}$$

Density is defined as ρ, R_n is the effective nose radius, and V is the vehicle speed. The exponents of $\frac{1}{2}$ and 3 correspond to m and n from Equation (35) for Earth.

The Sutton Graves method is very similar in make up to the Chapman method [7] [18]. Equation (37) is the version used for Earth where the constant was determined by the planet's atmosphere.

$$\dot{q_s} = 1.7415 \times 10^{-4}\left(\frac{\rho}{R_n}\right)^{\frac{1}{2}} V^3 \tag{37}$$

The only notable difference between the Chapman model and the Sutton Graves model is the constant out front which has the units of $(\mathrm{kg}^{1/2}\mathrm{m}^2)/\mathrm{s}^3$. Lastly, the final aerothermodynamic model compared in this research effort was the Galman model [8]. The Galman model was used in an article in 1961 by Barry Galman, which explored vehicles returning from orbit. The heating rate was calculated using an equation similar to Equation (38) for the glide portion of the reentry trajectory of a lifting body.

$$\dot{q_s} = 11.35377\,(2R_n)^{-\frac{1}{2}}\left(3.18\rho^{\frac{1}{2}}\right)\left(V^{3.2}\right)1 \times 10^{-9} \tag{38}$$

Equation (38) has been modified so the output is given in SI units of kW/m^2. The same variables are employed for the Galman model as with the Chapman and Sutton Graves models.

$$\mathbf{Q} = \int_{t_0}^{t_f} \dot{q}_s dt \tag{39}$$

The heat load, $\mathbf{Q}$, for the vehicle was also calculated by integrating the heat rate on the system throughout its trajectory for each aerothermodynamic model with Equation (39). The integration of the heating rate profile was conducted with the cumulative trapezoidal numerical integration command in MATLAB.

3.3 Chapter Summary and Expectations

The methods described in this chapter were aimed at demonstrating two research objectives with the first research objective being the utilization of the continuation process and the second being the comparison of aerothermodynamic models. To accomplish the first objective, a simple RK4 solution of a hypersonic glide vehicle trajectory was the initial seed to the first GPOPS-II problem formulation which had a cost function of maximizing longitudinal range of a generic HGV. The solution of the first GPOPS-II solution was used as the seed to the next iteration of code which had a cost function of maximizing Euclidean range. The solution of maximized Euclidean range was the seed for the next iteration of code which used a different vehicle model, the HARV, but still aimed to maximize Euclidean range. To accomplish the second objective, the HARV solution was used to seed the next iterations of code each with a path constraint on the stagnation point heating rate on the vehicle's nose. The stagnation point heating rate was calculated with three different aerothermodynamic models and each iteration of code further lowered the maximum heat rate limit. The heat load of each trajectory with each aerothermodynamic model was also calculated.

The continuation process is expected to alleviate the challenge of providing GPOPS-II code with a sufficient guess to solve a complicated problem. Additionally, this methodology should demonstrate the adaptability of the algorithm paired with the continuation process. The final range of the solution from Step 3 is expected to be larger than the range calculated from Step 1. A difference in trajectories and heating rate profiles are expected between each aerothermodynamic model. Due to the constants in Equations 36 and 37, a higher maximum heating rate and higher overall heat load is expected from the Sutton Graves model.

IV. Results and Analysis

Preamble

The process of continuation was successfully implemented with the GPOPS-II algorithm. All code was written in the MATLAB R2017b software and run on an HP Elitebook with an Intel Core i7 8th generation processor. Converged solutions were found for each iteration. The trajectory results differed between each aerothermodynamic model. The expectation of the Sutton Graves model predicting the highest maximum heat rate and heat load was shown in the results. The lowest heat rate was found from the converged solution with the Galman model. The results are presented in two sections that correspond to the organization from Chapter III: the results from utilizing the continuation process and the comparison of aerothermodynamic models. The chapter wraps up with an analysis of the presented results.

4.1 Utilizing Continuation

The process of continuation applied to the GPOPS-II algorithm successfully converged on optimal solutions based on the given criteria as indicated by the exit flags of "0 –finished successfully" and "1 –optimality conditions satisfied" from SNOPT for all iterations. Figures 25 and 26 clearly show the difference in trajectories between each iteration of code. The GPOPS-II algorithm is sensitive to the initial seed [37] which explains the similar graph shapes between the RK4Guess and the GPOPS code-1 solutions since the RK4Guess solution was used as the initial seed for GPOPS code-1. The trajectories from Steps 0-2 exhibited a traditional skipping trajectory expected in vehicles with lift-to-drag ratios near or greater than one as was modeled with the generic HGV model. While the skipping in Step 2, GPOPS code-2, is subdued, it is still present. As the continuation process progressed to the iteration of the GPOPS

HARV trajectory, the skipping in the altitude trajectory had been eliminated, as was observed in Figure 25, since the HARV model had a lift-to-drag ratio set near zero.

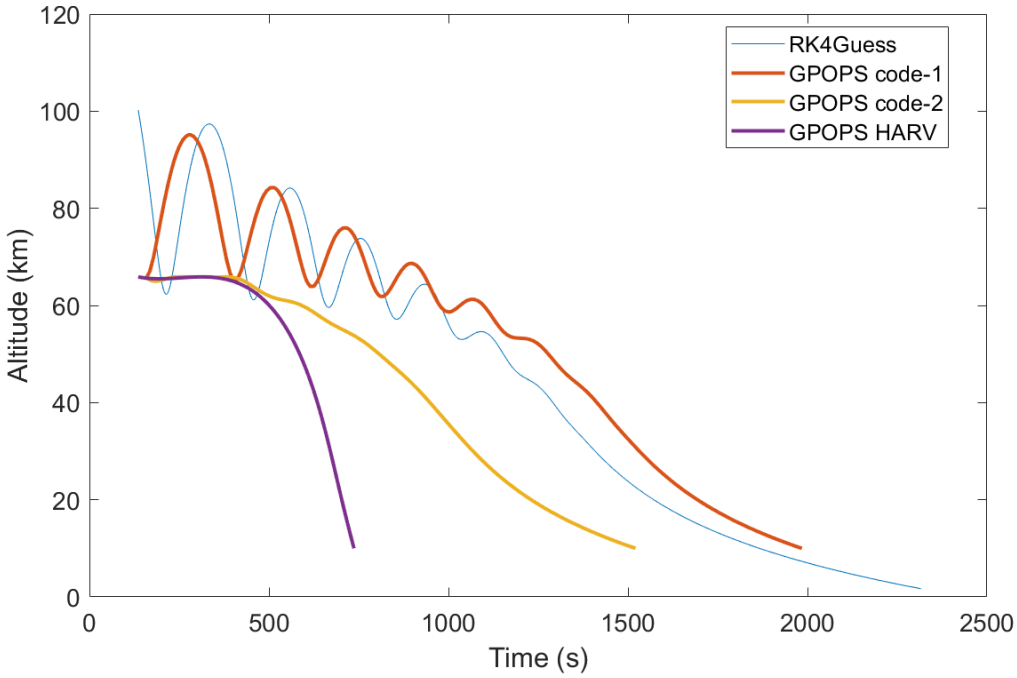

Figure 25. Altitude trajectory of hypersonic vehicle.

Figure 26 illustrates that the GPOPS-II codes solved for the optimal initial latitude and longitude for the vehicle to maximize its range while still ending on the fixed position. The initial latitude and longitude did not reach the bounds of the variables set in Table 6, indicating that the initial points are optimal for the problem formulation. GPOPS code-1 resulted in an initial altitude of 66 km, which was then used as the initial altitude for the next two iterations.

Figure 26 shows the difference in ranges of each iteration. The Euclidean range was increased 1.6% from 3,342 km in GPOPS code-1 to 3,397 km for GPOPS HARV through the continuation process. While this may seem like a small increase, it is due to the fixed initial altitude for GPOPS code-2 and GPOPS HARV. Since the HARV model had a lift-to-drag ratio of approximately 0.01, the best way to increase range would have been to start at a higher altitude due to the low amount of lift the vehicle

can generate. However, for the mission scenario used in this research effort the initial altitude was fixed for the GPOPS HARV solution and despite a fixed initial altitude, the algorithm was able to provide a larger Euclidean range. The objective for GPOPS code-1 was to maximize longitude only. Figure 26 confirms the objective as very little variation was shown in the latitude direction. With GPOPS code-2, the objective transitioned to maximize the Euclidean range. The change in latitude was more significant given the flexibility with the additional dimensions of the cost function. Finally, when incorporating the HARV data with maximizing Euclidean range, the largest distance was acquired. Many factors such as the weight and aerodynamic properties of the vehicle as well as the speed profile of the HARV contributed to its converged trajectory. A majority of the HARV trajectory was at a higher speed than the generic HGV solutions as can be observed in Figure 28. The ranges demonstrate that continuation allowed for a maximum range trajectory solution for the vehicle specific properties given a generic starting trajectory with a propagated solution.

The control history of the HARV, shown with the purple line in Figure 27, shows bang-bang control for the entire flight path. Bang-Bang control indicates an optimal solution. However, bang-bang control is not necessarily a realistic control to implement in flight. To alleviate this issue, implementing bank angle as a state and bank angle rate as the control would produce a realizable input for the bank angle of the vehicle, effectively applying a rate limit.

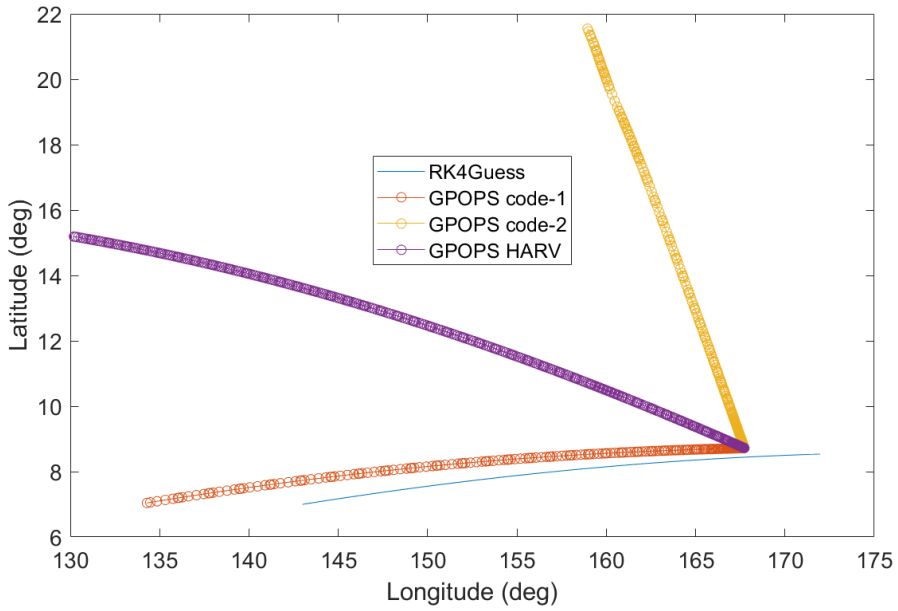

Figure 26. Latitude and longitude of vehicle over time.

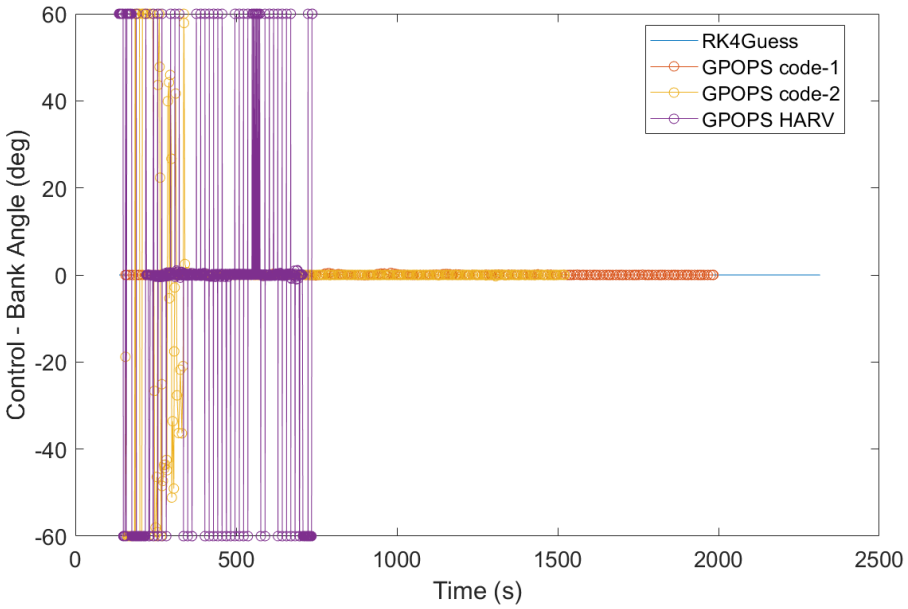

Figure 27. Control as bank angle of vehicle over time.

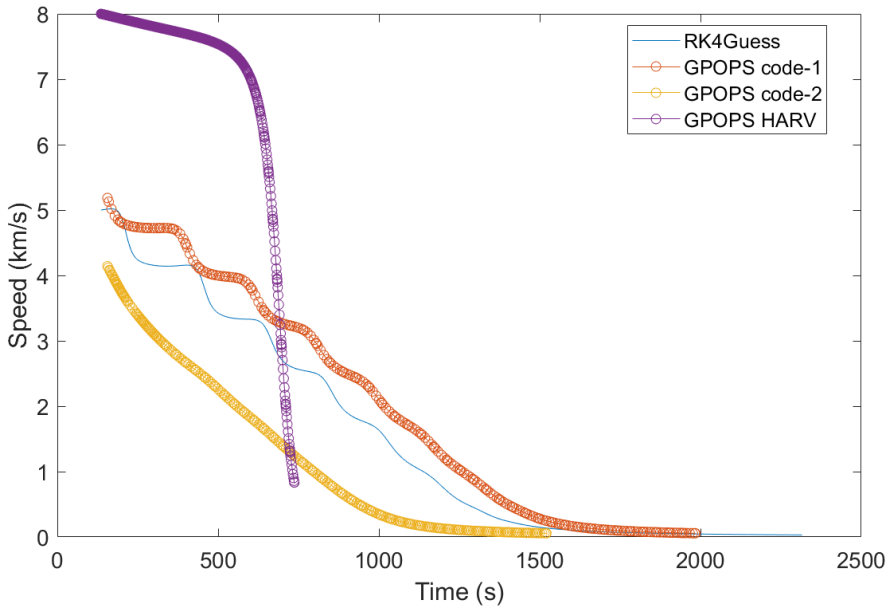

Figure 28. Speed of vehicle over time.

The speed of the vehicle decreased as it approached its final destination for every iteration as shown in Figure 28 due to the influence of drag. Figure 29 shows each term of the vehicle acceleration from Equation (27d) for the GPOPS HARV solution plotted on the same graph. The drag term dominates the change in speed, calculated with Equation (27d). Evaluating Equation (26) for drag reveals two non-constant terms: density and speed. Equation (24) for density gives values as expected with decreased altitudes resulting in exponentially increased density values. Plotting the $V^2\rho$ term from Equation (26) for drag in Figure 30 illustrates the coupled dynamics. A parabolic graph is present with a peak when the vehicle is at a speed of 3.4 km/s and an altitude approximately at 24 km where the density is 4.26×10^7 kg/km^3. These conditions occur around 600 seconds into the trajectory which is also where the largest deceleration of the vehicle occurs. The steepest slope of the speed graph for the GPOPS HARV solution can be observed around the 600 second mark in Figure 28.

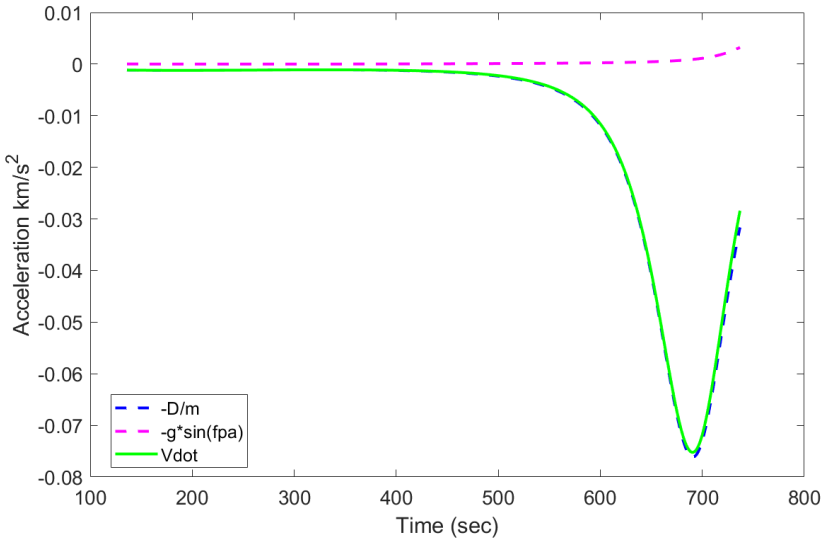

Figure 29. Contribution of Equation (27d) from the GPOPS HARV data.

The significant differences between the simple iterative Runge-Kutta guess and the follow on optimized solutions shows the power of continuation. The code took just under 100 seconds to complete all iterations of the continuation process from Steps 0-3.

4.1.1 Including a Path Constraint

The continuation process was utilized with code that included the addition of a path constraint. The path constraint was appended on to the GPOPS HARV code to limit the maximum heating rate of the vehicle trajectory. Steps 4-7 from the flowchart in Figure 24 used the continuation process, accomplished by incrementally decreasing the heat rate limit, with the intent of finding the lowest heating rate limit enforceable that would allow for a converged trajectory. Figures 31 and 32 show the evolution of the continuation process applied to code with the Chapman model. The lowest heat rate limit imposed on the system that still resulted in a converged trajectory was 1.63×10^4 kW/m^2 shown with the purple line in Figure 31. The converged trajectory solution from the higher limit was used to seed the next iteration of code with a lower

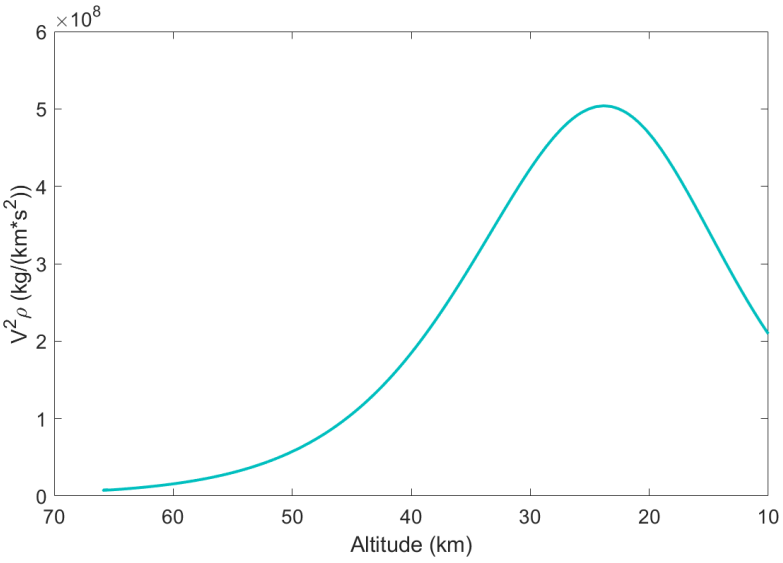

Figure 30. $V^2\rho$ **term from Equation (26) for drag with GPOPS HARV data.**

heat rate limit.

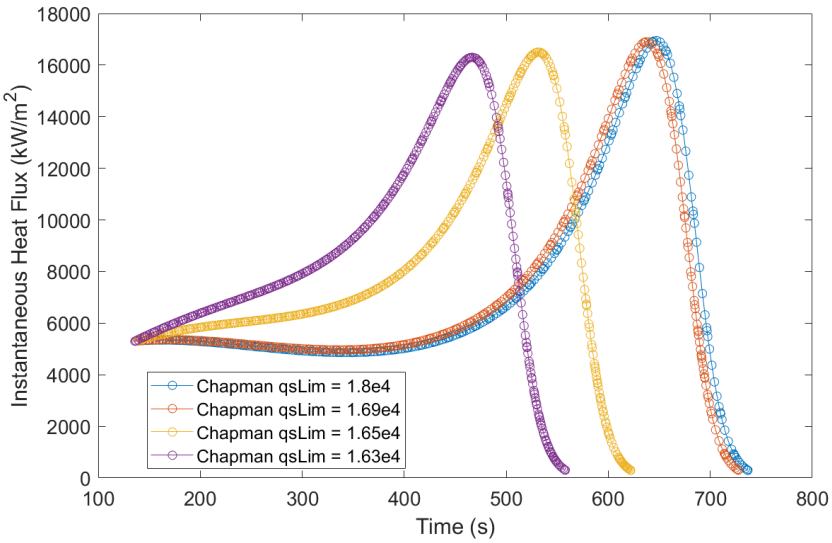

Figure 31. Stagnation point heating rate profiles of continuation Steps 4-7 calculated with the Chapman model.

The resulting altitude trajectories from the various heat rate limits are shown in Figure 32. A longer flight time would be expected to achieve a lower maximum heat rate from the reasoning that a lower heat rate limit warrants a shallower, and

therefore, longer glide path. However, the results from GPOPS-II code show the opposite. With lower heat rate limits, the flight times were reduced. The other aerothermodynamic models exhibited the same unexpected trend across Steps 4-7 as well. For the Chapman model, Step 4's flight time was 737 seconds while Step 7's flight time was 558 seconds, around 180 seconds shorter.

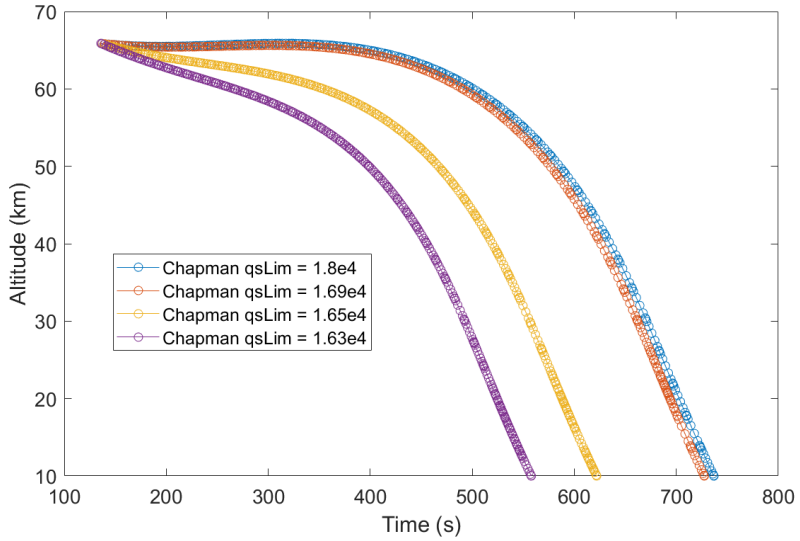

Figure 32. Altitude trajectory of continuation Steps 4-7 calculated with the Chapman model.

The reason for the unexpected steeper trajectories has to do with coupled system dynamics. Figure 33 shows the speeds of the converged trajectories from Steps 4-7 with the Chapman model. The steeper trajectories like the yellow and purple graphs of Steps 6 and 7, respectively, observed in Figure 32, reach lower speeds sooner as observed in Figure 33. Equation (36) for the Chapman model has density and speed as non-constant terms. Focusing on the speed term, V^3, the following logic can be reasoned: lower speed values would result in lower heat rate calculations when using Equation (36). The analysis at the end of Section 4.1 explains how speed changes which is influenced by coupled dynamics. Density is the other non-constant term influencing the heat rate calculations in Equation (36) and also has competing

interests. To decrease speed, density must be increased, but to decrease the heat rate, density must be decreased. Additionally, to decrease speed, the speed term in Equation (26) for drag must increase, but to decrease the heat rate, speed must be decreased. The coupled dynamics are why the peak heat rates occur at some combination of speed and density. For example, the maximum stagnation point heat rate from Step 7 with the Chapman model occurs when the vehicle is going 6 km/s at an approximate altitude of 37 km where the density was 6.40×10^6 kg/km^3.

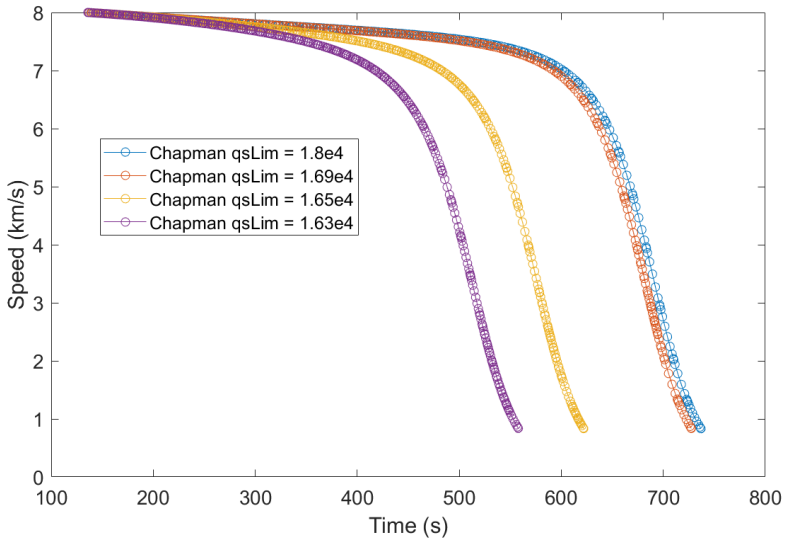

Figure 33. Speed history of continuation Steps 4-7 calculated with the Chapman model.

The same iterative continuation process as described for the Chapman model above was also applied to code with each of the other aerothermodynamic models. The same analysis was accomplished for each of the other two aerothermodynamic models as well and the same trends in the data were concluded. The run time for code of all the iterations from Steps 4-7, with the Chapman model was around 19 seconds, with the Sutton Graves model was approximately 18 seconds, and with the Galman model was around 14 seconds.

4.2 Comparing Aerothermodynamic Models

Three aerothermodynamic models were used to calculate the stagnation point heating rate at the nose of the HARV. Various heating rate limits were imposed on the system. For comparison, the heating rate for the GPOPS HARV solution, without any path constraints, was also calculated. A summary of some key data points can be found in Table 8. The maximum heating rates for the Step 3 GPOPS HARV solution shown in Figure 34 were $1.694\,70 \times 10^4$ kW/m^2 for the Chapman model, $1.811\,70 \times 10^4$ kW/m^2 for the Sutton Graves model, and $1.649\,50 \times 10^4$ kW/m^2 for the Galman model. The next iteration, Step 4, used a baseline maximum limit heat rate chosen for all three models based on the maximum heating rates achieved from the GPOPS HARV trajectory. The value chosen was 1.80×10^4 kW/m^2.

Table 8. Step 3-7 results from each aerothermodynamic model.

		Step 3	Step 4	Step 5	Step 6	Step 7
Chapman	**Flight time (sec)**	737	737	727	622	558
	$q_{smax}lim$ **(kW/m²)**	N/A	1.8×10^4	1.69×10^4	1.65×10^4	1.63×10^4
	q_{smax} **(kW/m²)**	1.69×10^4	1.70×10^4	1.69×10^4	1.65×10^4	1.63×10^4
	Euclidean Range (km)	3,397	3,397	3,388	3,295	3,248
Sutton Graves	**Flight time (sec)**	737	708	612	585	543
	$q_{smax}lim$ **(kW/m²)**	N/A	1.8×10^4	1.76×10^4	1.75×10^4	1.74×10^4
	q_{smax} **(kW/m²)**	1.694×10^4	1.8×10^4	1.76×10^4	1.75×10^4	1.74×10^4
	Euclidean Range (km)	3,397	3,370	3,287	3,267	3,237
Galman	**Flight time (sec)**	737	737	714	610	580
	$q_{smax}lim$ **(kW/m²)**	N/A	1.8×10^4	1.64×10^4	1.60×10^4	1.59×10^4
	q_{smax} **(kW/m²)**	1.694×10^4	1.6498×10^4	1.64×10^4	1.60×10^4	1.59×10^4
	Euclidean Range (km)	3,397	3,397	3,375	3,285	3,263

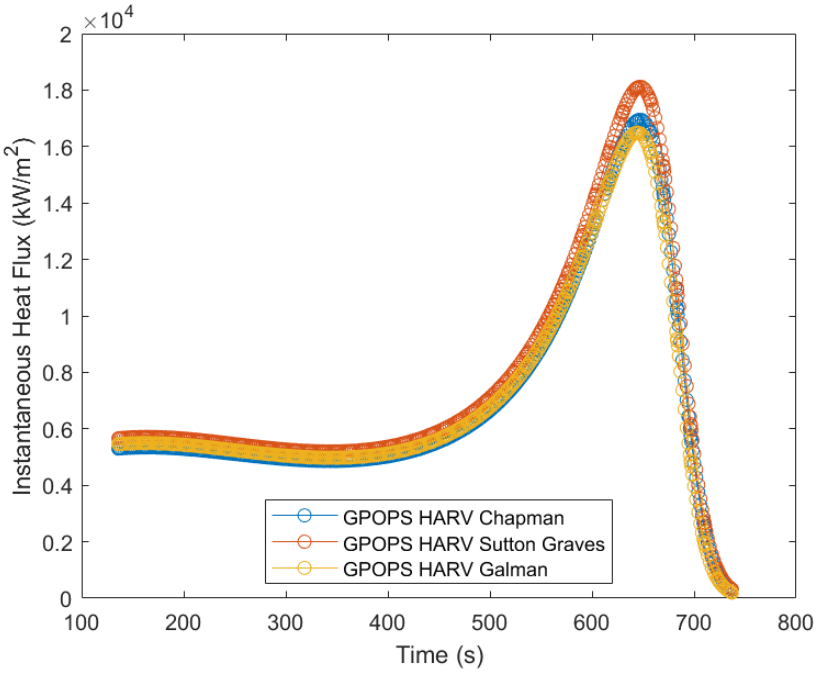

Figure 34. Stagnation point heating rates calculated with each aerothermodynamic model for the GPOPS HARV solution.

With the heat rate limit set at 1.80×10^4 kW/m^2 for Step 4 for all three aerothermodynamic models, the maximum heat rate for the solutions with each model is shown in Figure 35. The maximum heat rate values were 1.6951×10^4 kW/m^2 for the Chapman model, 1.80×10^4 kW/m^2 for the Sutton Graves model, and $1.649\,80 \times 10^4$ kW/m^2 for the Galman model. The maximum heat rate values for the Chapman and Galman models were slightly higher (around 0.001%) than the maximum values achieved in Step 3 due to the heat rate limit being higher.

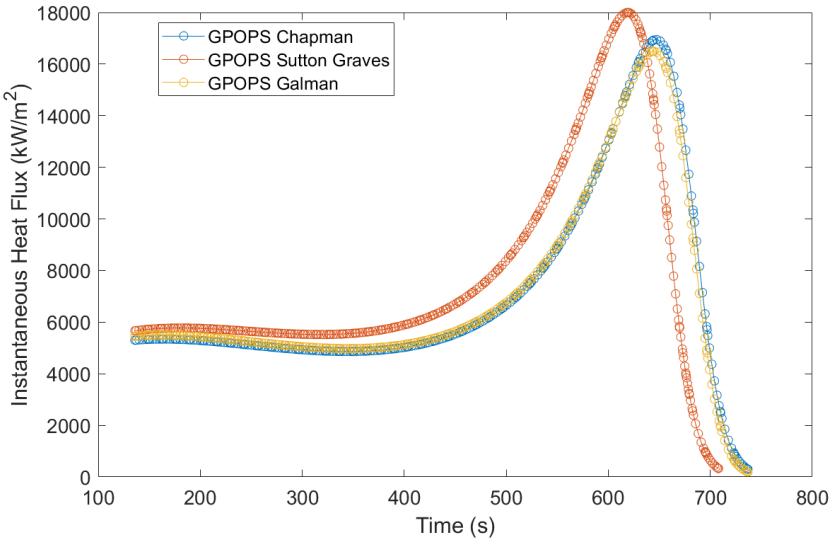

Figure 35. Heating rate profile with a maximum heating rate of $1.80 \times 10^4 kW/m^2$.

The maximum heat rate limit was decreased through each iteration of the continuation process for Steps 4-7 to find the lowest heat rate limit with a converged solution. Figure 36 shows the heat rate from each aerothermodynamic model of the solution from the last iteration, Step 7. Each model achieved a different maximum instantaneous heat rate limit with the Galman model having the lowest maximum heat rate of 1.59×10^4 kW/m^2 and the Sutton Graves model having the highest of 1.74×10^4 kW/m^2, around 9% higher. Table 9 was created using the Stefan-Boltzman Law with Equation (22) in Section 2.5 to find the corresponding surface temperature for various stagnation point heating rate values [18] [40]. The heat rate values presented in Table 9 are the maximum heat rate limits chosen for Step 4-7 across all three aerothermodynamic models.

Table 9. Corresponding surface temperature values of stagnation point heating rates.

$\dot{q}_s$ $\left(\frac{kW}{m^2}\right)$	Temperature (K)	Temperature (°C)
1.8e4	4463	4190
1.75e4	4432	4159
1.74e4	4426	4152
1.73e4	4419	4146
1.69e4	4393	4120
1.65e4	4367	4094
1.64e4	4361	4087
1.63e4	4354	4081
1.60e4	4334	4061
1.59e4	4327	4054

As mentioned in Section 2.5, a carbon-carbon composite material would be able to withstand a maximum heat rate of 4 MW/m^2 which corresponds to a maximum temperature around 3000 K. At the lowest heat rate limit of 15.9 MW/m^2, the maximum temperature of 4327 K would be too high. Peak stagnation point heat rates from other literature are much lower as well. Masternak reported a maximum nose heat rate of approximately 1.3 MW/m^2, reference "Sec 5.2.5" for the problem formulation in Figure 18 without a temperature path constraint [14]. Meanwhile for the problem formulation with a temperature constraint of 2255 K, see details in Figure 18 for "Sec 5.2.10", a maximum nose heat rate of approximately 667 kW/m^2 was experienced [14]. Makkapatti et al. presented results that remained under their maximum heat rate limit set at 400 kW/m^2 [23]. The largest maximum heat rate found from the literature review conducted in Chapter II was from Coulter et al. with a maximum

heat rate just under 7.5 MW/m^2 [16]. Although reported maximum heat rate values were higher, it is important to note that the vehicle models represented had higher lift-to-drag ratios enabling convergence upon different trajectories unattainable by the HARV model.

Contradictory to the trend found across Steps 4-7 discussed with Figures 31-33, the results within a step demonstrated that a lower maximum heat rate had a longer flight time, as expected in Figure 36. Flight time for the solution with the Galman model was around 580 seconds, while flight time for the system with the Sutton Graves model was around 540 seconds (approximately 7% less).

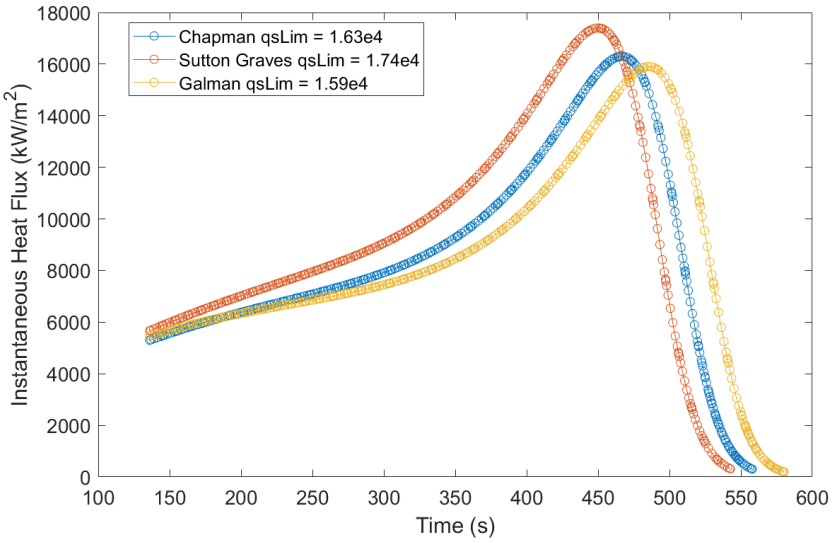

Figure 36. Stagnation point heating rate profiles from each aerothermodynamic model from Step 7, the last iteration in the continuation process.

A shorter flight time would indicate a steeper flight path. The altitude trajectories of each model from the last iteration are shown in Figure 37. The solution with the Sutton Graves model, in red, began descending sooner than the other trajectories. Following the same analysis as made for Figures 31-33, the next step in analysis was to look at the speed profiles for the systems with each aerothermodynamic model from Step 7, which are presented in Figure 38. The trend across speeds is also contradictory

to the findings in Figure 33. However, the analysis and explanation from Section 4.1.1 is still valid. The trend observed in Step 7 across the various aerothermodynamic models directly highlights the difference between each model. At the same speed, each model will predict a different stagnation point heat rate on the vehicle nose. For example, at 5 km/s the vehicles from each system were approximately at 31 km of altitude but each aerothermodynamic model predicted a different stagnation point heating rate. The Chapman model predicted 1.44×10^4 kW/m^2, the Sutton Graves model estimated 1.53×10^4 kW/m^2, and the Galman model approximated 1.37×10^4 kW/m^2 given the same speed and altitude. The difference between each model is also why the Galman model was able to meet a lower maximum heat rate limit than the Sutton Graves model.

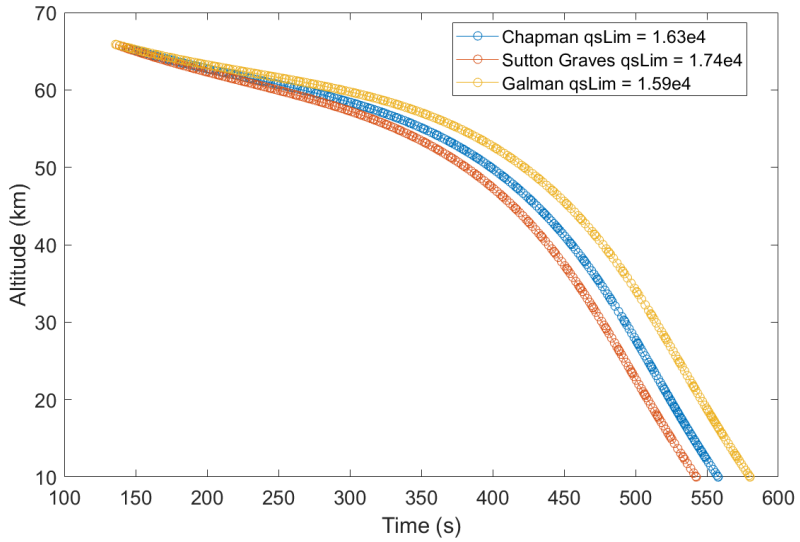

Figure 37. Altitude trajectories of Step 7, the last iteration in the continuation process.

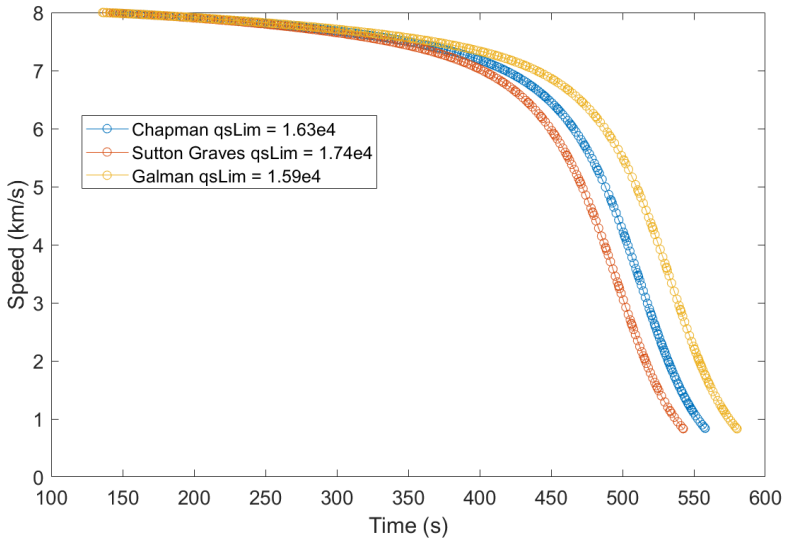

Figure 38. Speed history of Step 7, the last iteration in the continuation process.

A shorter flight time would also indicate a shorter range which is confirmed in Figure 39. The x-axis progresses with larger range values starting on the left. Ranges from Steps 3-7 from the continuation flowchart, in Figure 24, are shown for systems for all three aerothermodynamic models as well as the maximum heat rate values. As a reminder, while the problem formulation in Step 3 for GPOPS HARV did not include a path constraint, the heating rate values were calculated post hoc with each aerothermodynamic model applied to the trajectory solution. The different starting points of Step 3 calculated with each aerothermodynamic model also clearly show the differences between each model's over or under prediction relative to one another as previously discussed with Figures 37 and 38. Analyzing the Chapman and Galman lines, the first two data points appear coincident on Figure 39, with the remaining three points showing a decrease in range. Steps 3 and 4 had very similar values as shown in the q_{smax} rows for the Chapman and Galman models in Table 8.

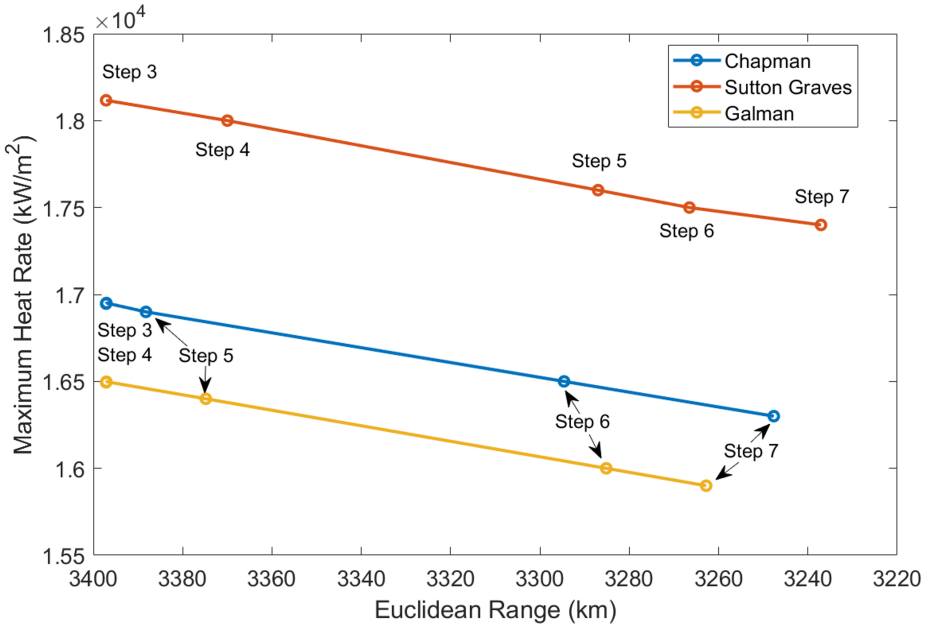

Figure 39. Euclidean range achieved vs heat rate of each aerothermodynamic model from each iteration starting with GPOPS HARV.

The difference between ranges achieved in Steps 3 and 7 was around 4% with each aerothermodynamic model. The general trend from the systems with each aerothermodynamic model showed that a decreased maximum heat rate limit, i.e. a more constrained problem, corresponds to a shorter range.

4.2.1 Heat Loads

Heat loads for each trajectory were calculated by integrating the heat rate values over the flight time. Heat load and heat rate are both important for determining what temperatures the external material on the vehicle would have to survive. Heat rate provides the highest amount of heat the material would have to withstand for a brief moment while heat load is the total amount of energy the material would experience for the duration of the flight.

Figures 40 and 41 show the heat load on the vehicle for the duration of the flight. The heat load graphs show steeper increases in heat load accumulation around 600

seconds in Figure 40 and 450 seconds in Figure 41 which correlated to the peaks in Figures 35 and 36, respectively. The peak is not as sharp in Figure 36 hence the smoother curves in 41. The final heat load values for Step 4 solutions were lower in the Step 7 solutions.

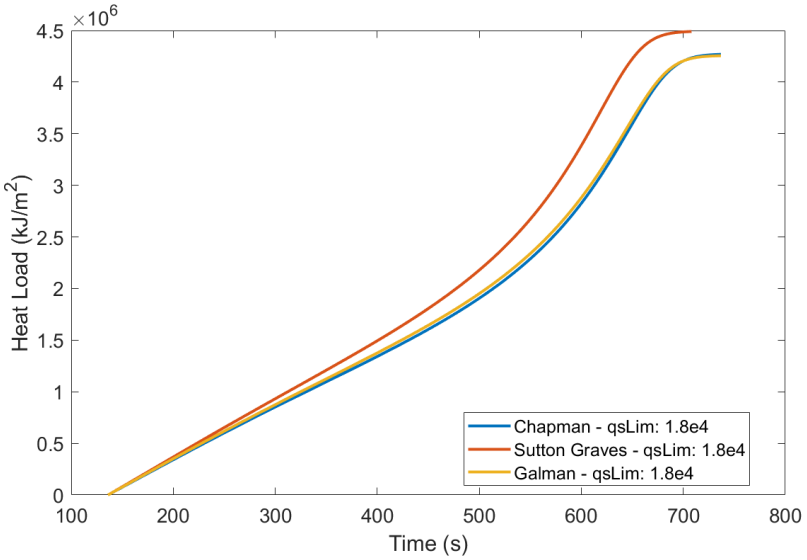

Figure 40. Integrated heat load of each of the three aerothermodynamic models of Step 4 trajectory solutions with a maximum heating rate limit of 1.80×10^4 kW/m^2.

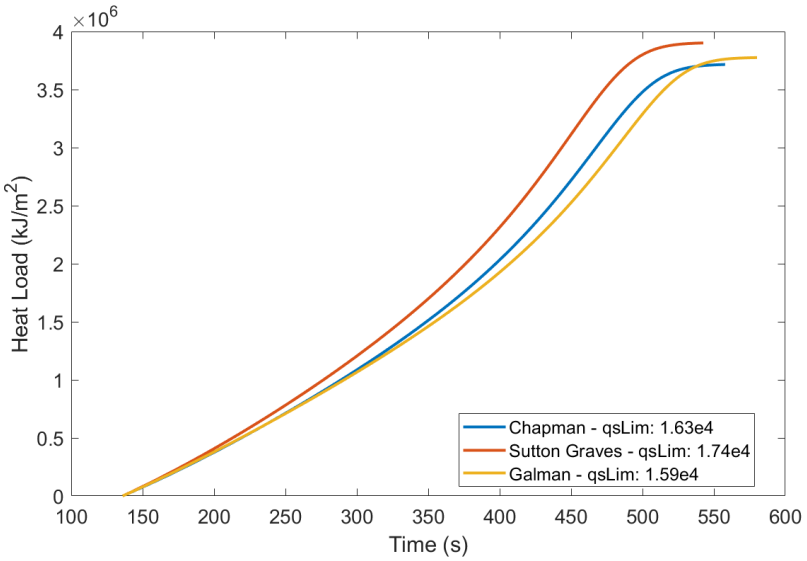

Figure 41. Integrated heat load of each of the three aerothermodynamic models of Step 7 trajectory solutions with various maximum heating rate limits on each model.

Figure 42 shows the resulting maximum heat load accumulated at the end of the flight versus the maximum heat rate the vehicle experienced during its trajectory. Unsurprisingly, the trajectory solution with the Sutton Graves model had the highest heat load in the last iteration of the continuation process as well as the highest maximum heat rate compared to the solutions with the other aerothermodynamic models. The lowest heat load was experienced by the vehicle trajectory with the Galman method.

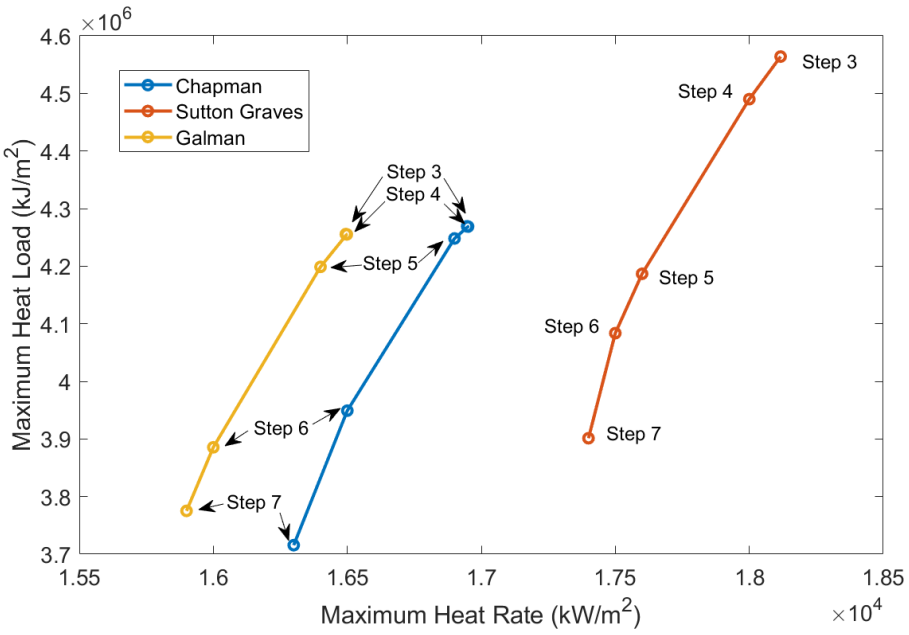

Figure 42. Maximum heat load vs maximum heat rate of each aerothermodynamic model from each continuation iteration starting with GPOPS HARV (Steps 3-7).

4.3 Analysis

The achievement of a converged solution of a HARV model with a path constraint from beginning with a simple iterative Runge-Kutta guess shows the power of continuation. The ranges from each converged trajectory demonstrate that continuation allowed for a maximum range trajectory solution for the vehicle specific properties given a generic starting trajectory with a propagated solution. The bang-bang con-

trol profile of the vehicle bank angle is not feasible to fly, and one method discussed was to add bank angle as an additional state and make bank angle rate the control, thereby, imposing a rate limit. The code took just under 120 seconds to complete all iterations of the continuation process from Step 0-7 regardless of which aerothermodynamic model used to calculate heat rates. In the last iteration, Step 7, a higher limit on the heat rate with the Sutton Graves model compared to the other models resulted in the shortest flight time and the shortest range. A higher heat rate limit resulted in a steeper glide path. The steeper flight path with the HARV model meant less flight time and therefore, a shorter range than the system with the Galman model with a longer flight time and longer range. The system with the Galman model resulted in a 7% longer flight time and a 26 km longer range despite being given the lowest heat rate limit of the three aerothermodynamic models.

The reason the Galman model was able to achieve the lowest maximum heat rate of the three aerothermodynamic models is because of the model's under-prediction of stagnation point heating rates, relatively speaking. The aerothermodynamic models in this research effort can only be analyzed relative to each other because there is no experimental data or CFD analysis currently to compare results to. Therefore, of the three models in this research, the Sutton Graves model over-predicts while the Galman model under-predicts and the Chapman model gave results consistently between the two.

The expected result of lowering the maximum heat rate limit was a longer flight time. However, this was not observed in the results from Steps 4 to 7, for all aerothermodynamic models. The unexpected results were due to the coupling of several equations with the largest influence coming from the density and speed variables. The combination of altitude and speed at 37 km and 6 km/s, respectively, produced the highest stagnation point heat rates for a 0.03 m radius nose in Step 7 across all

aerothermodynamic models.

Concluded from the analysis on Figure 39, a trade off is required between range and maximum heat rate experienced by the vehicle depending on the mission since lowering the maximum heat rate reduced the flight path range. In regards to heat load, while Figure 42 showed a trend of a lower maximum heat rate resulting in a lower maximum heat load, that trend is not necessarily true for every case. There can be a case where one vehicle has a higher maximum heat rate but a lower maximum heat load than another vehicle. Finally, through the continuation process, the trajectory solutions with each aerothermodynamic model experienced decreases in both maximum heat rates and maximum heat load values through the iterative continuation process.

V. Conclusions

5.1 Summary of Research

The recent development of maneuverable hypersonic vehicles has spurred an increase of research in the field. Hypersonic weapons have advantages over traditional ballistic missiles. Hypersonic weapons are able to maneuver during flight and stay at lower altitudes which makes detection more challenging when compared to traditional ballistic trajectories. Direct orthogonal collocation methods were employed to solve for an optimized hypersonic trajectory via the pseudospectral solver called GPOPS-II. The process of continuation was applied since the hypersonic trajectory optimization problem is a complicated problem and the GPOPS-II algorithm requires a sufficient seed input. Continuation enabled the use of a simple seed and a simple initial problem that was then propagated to reach the solution for a more complex problem. The continuation process alleviated the need for providing a sufficient initial seed to a very complicated problem. Each step in the continuation process was required to reach the final iteration in this research. Three dimensional (3D), three degree of freedom (3DOF) equations of motion (EOMs) with the assumptions of no thrust and a non-rotating Earth were the system dynamics. Bank angle was set as the control. Converged solutions were produced for the glide phases of two HGVs, one generic lifting body based on the CAV model and the HARV with the continuation process.

Iterations of code began with a simple Fourth-Order Runge-Kutta (RK4) iteration of the generic HGV, which was used to seed the first iteration of GPOPS-II code. The first iteration of GPOPS-II code optimized the trajectory to maximize longitudinal range. The solution was used to seed the next iteration of GPOPS-II code which optimized its solution to maximize the Euclidean range. The next iteration of

unconstrained GPOPS-II code presented an optimized solution also to maximize the Euclidean range with the difference of using HARV characteristics.

The flight path of the solutions with the generic HGV model followed skipping trajectories, typical of lifting bodies. The influence of the seed was observable with the similar general shape of the converged solution. Each iteration in the continuation process showed a perceptible difference between trajectories, observable in Figures 25-28.

The converged solution of the HARV model was used to seed the next iterations of the continuation process with an appended path constraint on the maximum stagnation point heat rate on the nose of the vehicle. The stagnation point heating rate was calculated with three aerothermodynamic models of similar fidelity via the Chapman model, the Sutton Graves model, and the Galman model. Each iteration of the continuation process decreased the maximum heat rate limit imposed on the vehicle. The lowest heat rate predictions were from the Galman model while the highest estimates were from the Sutton Graves model. The Chapman model consistently approximated heat rate results between the other two models. The lowest heat rate limit achieved with a converged solution was 15.9 MW/m^2 from the system with the Galman model which corresponds to a temperature of around 4,300 K. Even the lowest achieved maximum heating rate of 15.9 MW/m^2 was an order of magnitude larger than any maximum heat rate value found in previous literature. However, the HARV vehicle model had a significantly lower lift-to-drag ratio making certain trajectories that would allow for a lower maximum heat rate value unachievable. One way to reach lower the heat rate limits would be to model a higher lift-to-drag ratio. The HARV can be modeled with a higher lift-to-drag ratio using a higher fidelity model. Another option for modeling a higher lift-to-drag ratio is by choosing a different vehicle model. Additionally, it is important to acknowledge the inaccuracies of the stagnation point

heat rate models as discussed in Section 2.2 in work by Bettinger [25]. CFD would be a helpful realization tool to validate aerothermodynamic model estimates in the future.

When comparing aerothermodynamic models there was an expectation that a lower maximum heat rate limit would result in a longer flight time. The logic behind this expectation was based on the assumption that a lower maximum heat rate limit would require the vehicle to fly a shallower glide path to its terminal position taking more time. The analysis of the coupling of systems explained why the results exhibited a trend contrary to the expectation. Competing interests on the speed and density variables influenced the convergence.

Finally, heat load from each aerothermodynamic model was calculated by integrating the heat rates across the total flight time. A larger maximum heat rate corresponded to a larger maximum heat load at the end of the flight across all aerothermodynamic models with the HARV model. However, a trajectory with a higher maximum heat rate does not necessarily have to result in a higher overall heat load. The results presented from this research effort do not encompass all scenarios.

5.2 Research Impact

The largest contribution of this research was demonstrating the utility of the continuation process exhibited with the ease of implementation of continuation for various problem formulations. The continuation process alleviated a common issue of providing the GPOPS-II algorithm with a sufficient guess to a complicated problem. Solutions to optimal trajectories with HARV data require either an intelligent guess to initiate the algorithm or utilization of the continuation process. Converged solutions were achieved for each iteration in the continuation process. The Sutton Graves model produced the highest, most conservative stagnation point heating rate

estimates while the Galman model approximated the lowest heat rates. However, all aerothermodynamic models produced estimations within the same magnitude. Therefore, without CFD confirmation or another method of validation, a recommendation cannot be made as to which aerothermodynamic model is more accurate; only the differences can be stated. The largest takeaway from the results is the demonstration of the effectiveness of the process of continuation for solving a complicated hypersonic trajectory optimization problem.

5.3 Future Work

There are many directions that the current research can be taken in. The exploration of various mission scenarios is important to expand the scope of the simulation tool. Changing and enhancing the system can be accomplished in many ways to include adding a rate law for a more realistic control history, increasing the fidelity by adding lift and drag calculations, and extending the problem formulation to include the launch phase of flight, to name a few. With changes, it is crucial to note the sensitivity of the GPOPS-II algorithm to variable bounds. The effects of minor changes on variable bounds, whether the bounds are too big or too small, is a commonly encountered challenge for determining convergence. This challenge can be alleviated with non-dimensionalization of the problem, although it comes with its own challenges. While this research effort did not find bounds to be a limiting factor of convergence, it is a possibility to acknowledge for the future.

5.3.1 Constraints

The next step in research would be incorporating more constraints on the system to achieve higher fidelity results. The natural progression would be to include higher fidelity aerothermodynamic models such as Eckert's reference enthalpy method, as

mentioned in Section 2.2. Reference enthalpy or reference temperature methods take into account compressibility effects in a simplified manner via some reference temperature inside the boundary layer [1]. These methods are better suited for slender bodies [16] and preferred for analysis due to simplicity of application to hypersonic problems [1]. A CFD analysis, another higher fidelity model, of heating rates and temperatures at significant points, like maximums, along the flight path would provide a layer of accuracy and validation. Additionally, the vehicle can experience enormous forces at high speeds that would need to be constrained to ensure its survival. Load and dynamic pressure path constraints would address those forces [23]. All aforementioned constraints appended to the system will work to achieve more realistic, accurate results.

5.3.2 Lift and Drag

Including variable coefficients of lift and drag would increase model fidelity. There are multiple ways to include non-constant coefficients of lift and drag. The two main avenues are aerodynamic look-up tables [12] [13] [14] or surface pressure distribution calculations [15] [16]. Aerodynamic look-up tables can be acquired via empirical data or from CFD analysis. Empirical data is compiled from flight test data, however, these aerodynamic look-up tables are only convenient when available. CFD uses various modeling techniques to calculate and produce the required aerodynamic look-up tables. However, CFD is computationally expensive. Different methods of varying fidelities can be used to calculate surface pressure distributions. Lift and drag can be extracted from the surface pressure distribution equations which can be incorporated into GPOPS-II and calculated within the code. Since empirical data is not available for the vehicle models used in this research effort, future work will need to calculate coefficients of lift and drag.

5.3.3 Phases of Flight

Finally, expanding the scope of the project to include additional phases of flight like the launch and terminal phases is another progression. Terminal conditions that replicate similar values found in missiles should be considered for improving result accuracy. Additionally, expanding code to incorporate a HCV model would warrant appending a cruise phase of flight. Cruise and launch phases of flight have different dynamics which can easily be accommodated with the GPOPS-II algorithm via phasing. Particularly, the addition of a propulsion model is required for the launch and cruise phases. The end goal of the continuation process is to have a complete feasible result of the entire flight path of a hypersonic vehicle. This work is important to furthering the knowledge of hypersonic trajectories and the coordination of various disciplines.

Appendix A. Additional Result Plots

Steps 4-7 of Chapman Model

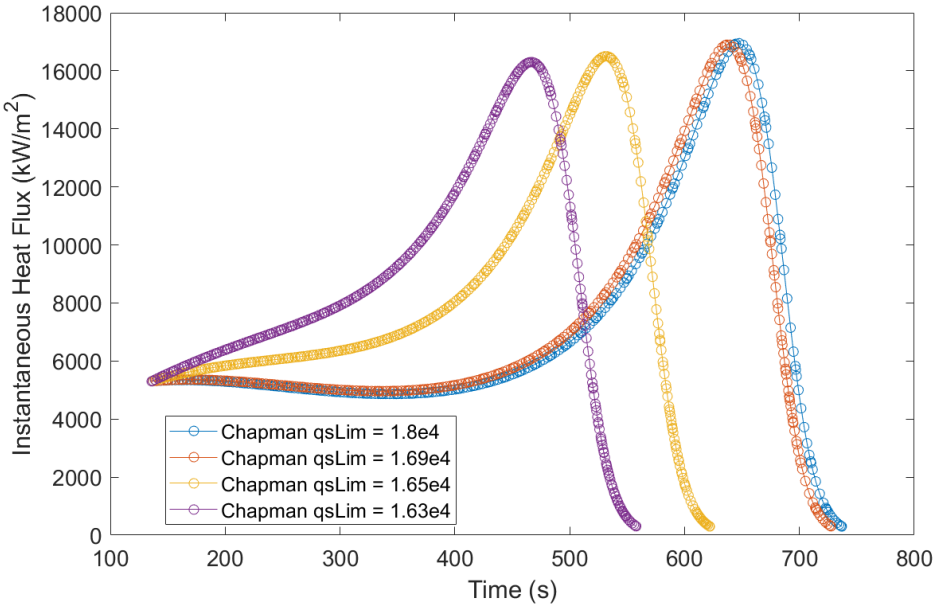

Figure 43. Steps 4-7: Stagnation point heat rate calculated with Chapman model.

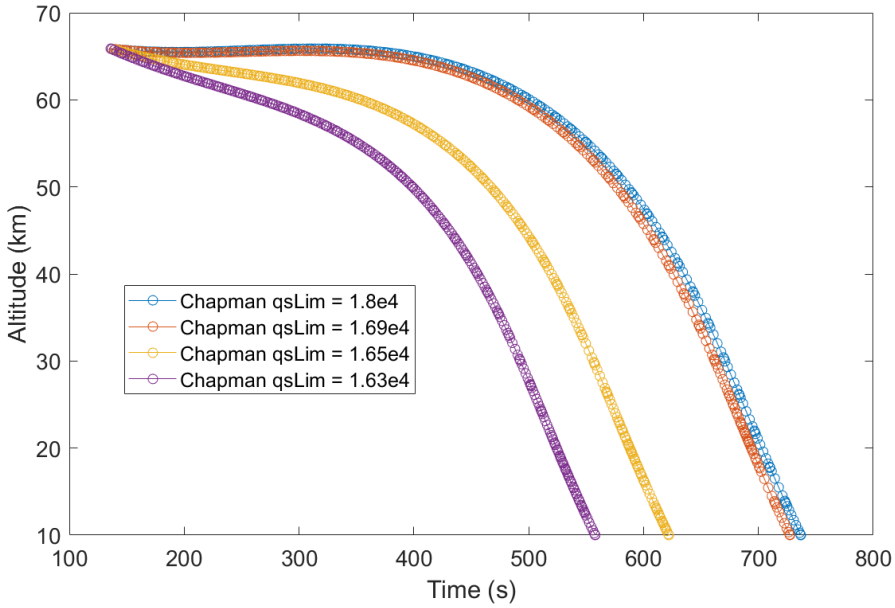

Figure 44. Steps 4-7: Altitude trajectories of system with Chapman model.

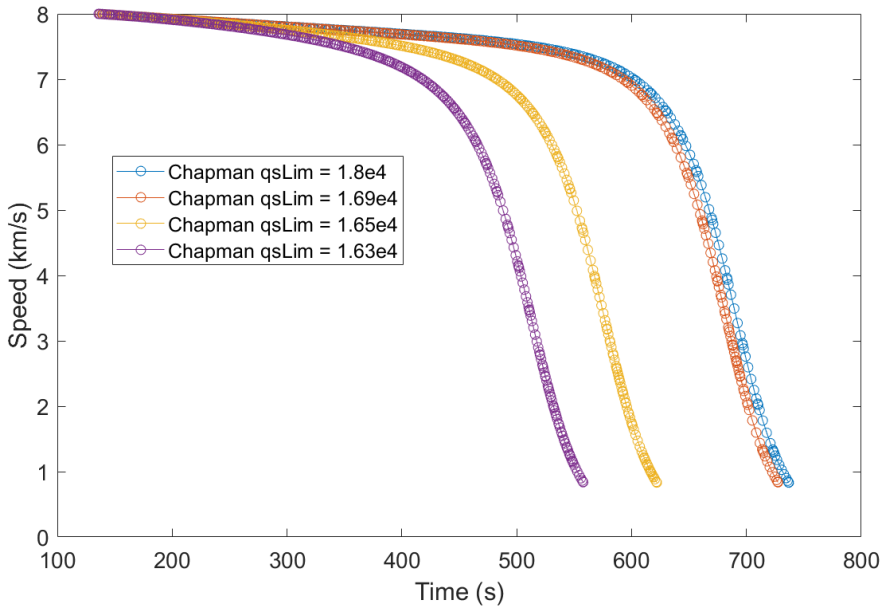

Figure 45. Steps 4-7: Speed profiles of system with Chapman model.

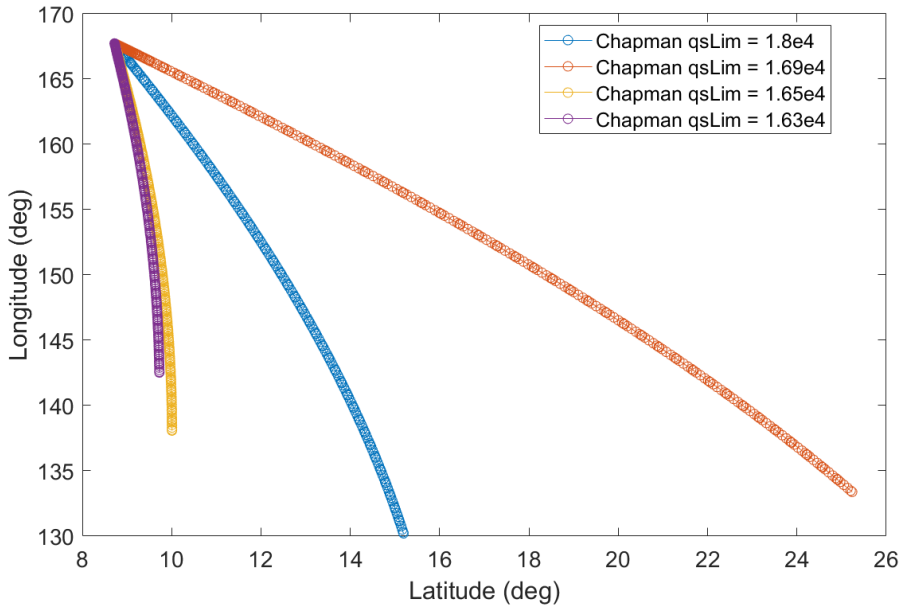

Figure 46. Steps 4-7: Vehicle position of system with Chapman model.

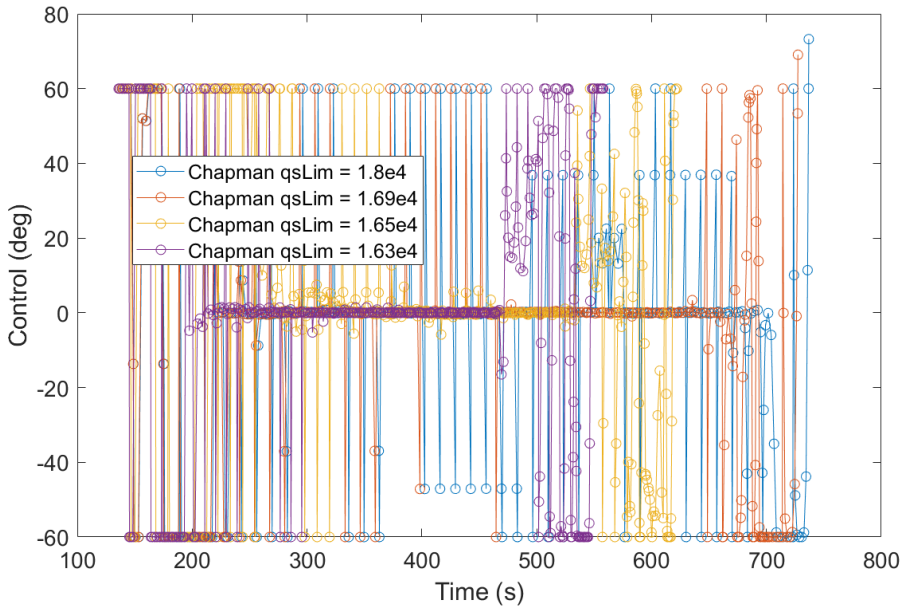

Figure 47. Steps 4-7: Control history of system with Chapman model.

Steps 4-7 of Sutton Graves Model

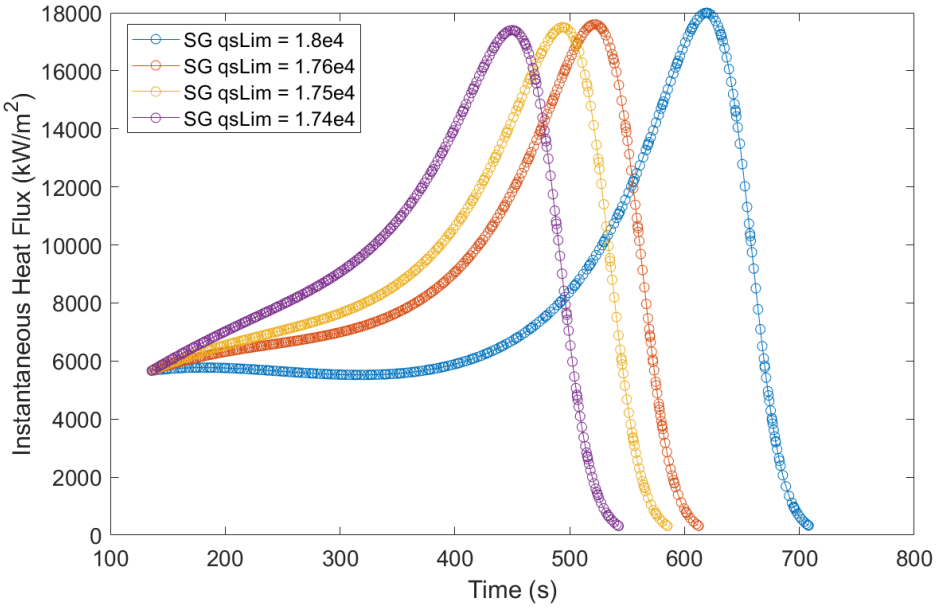

Figure 48. Steps 4-7: Stagnation point heat rate calculated with Sutton Graves model.

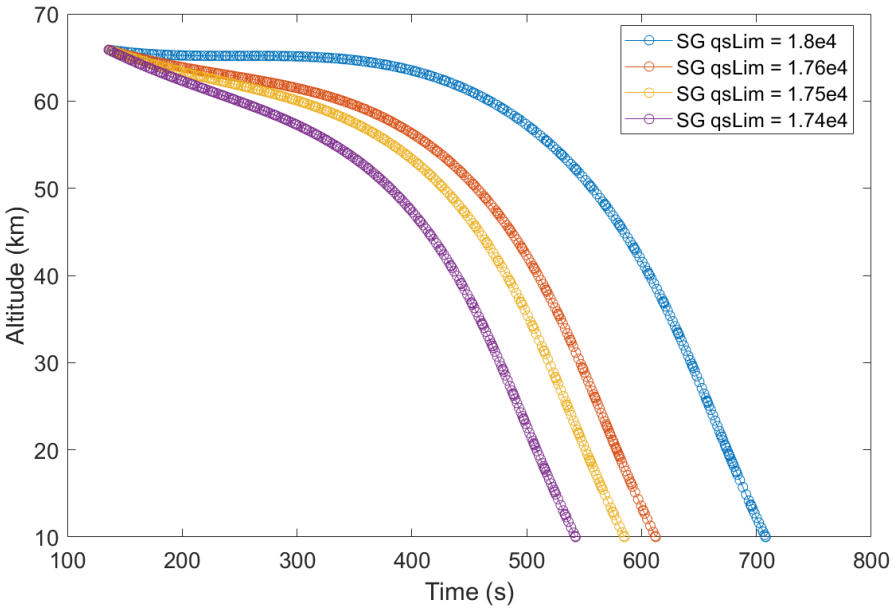

Figure 49. Steps 4-7: Altitude trajectories of system with Sutton Graves model.

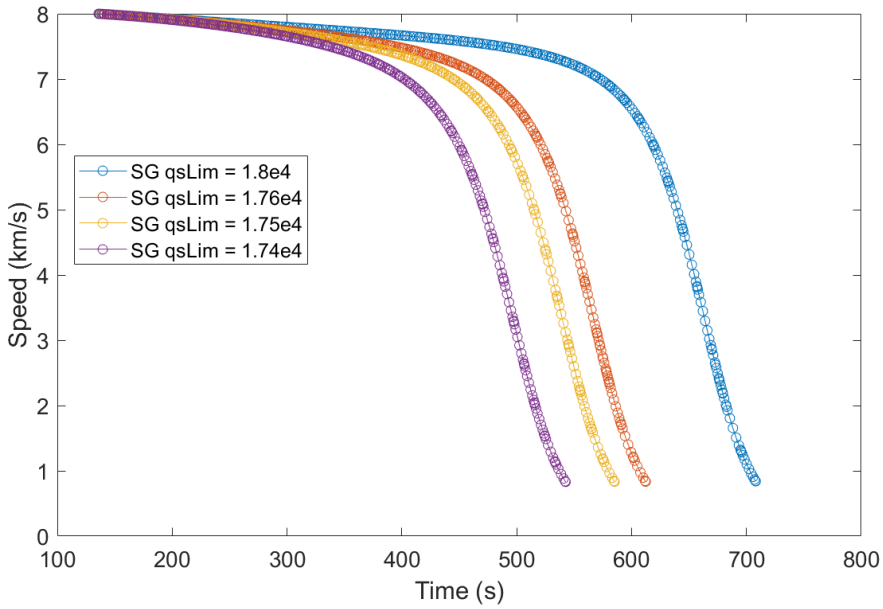

Figure 50. Steps 4-7: Speed profiles of system with Sutton Graves model.

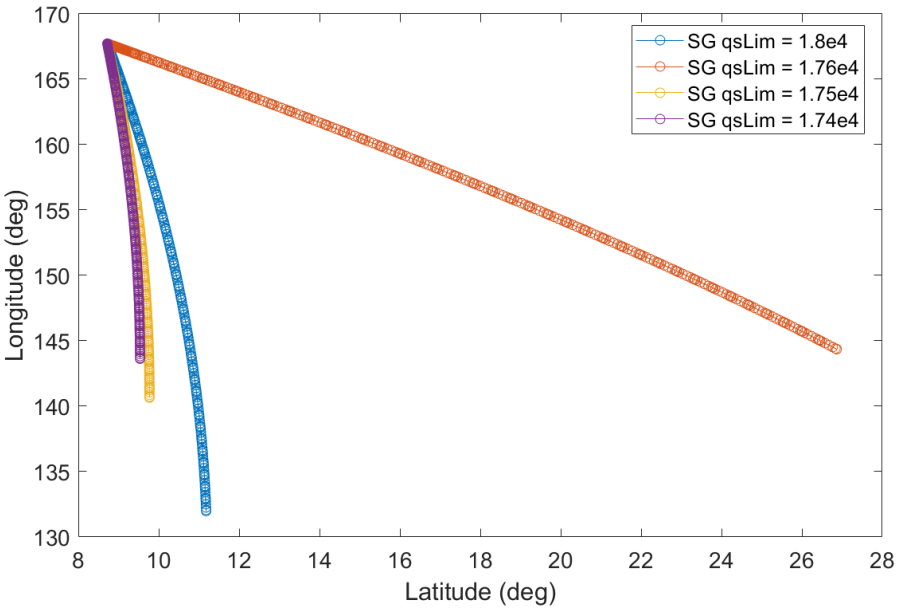

Figure 51. Steps 4-7: Vehicle position of system with Sutton Graves model.

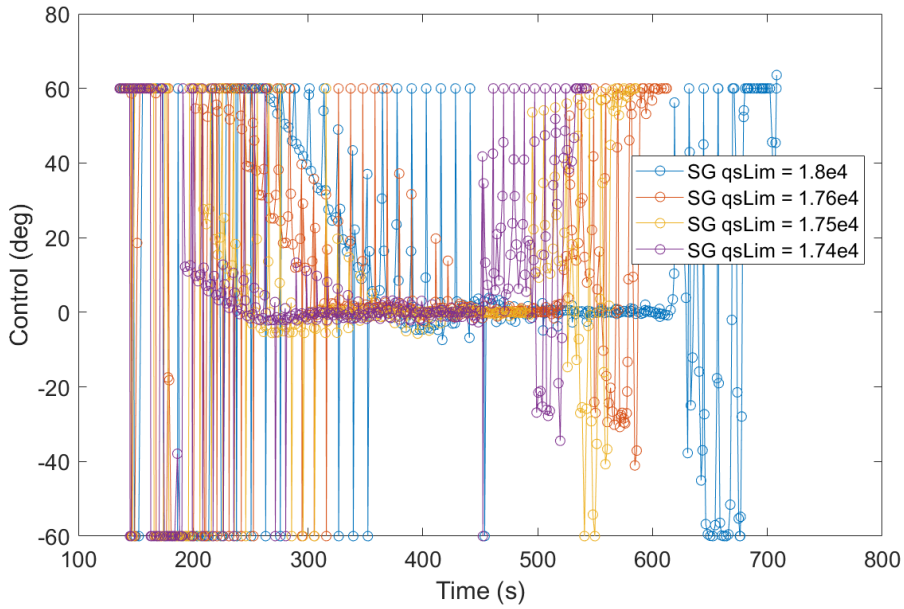

Figure 52. Steps 4-7: Control history of system with Sutton Graves model.

Steps 4-7 of Galman Model

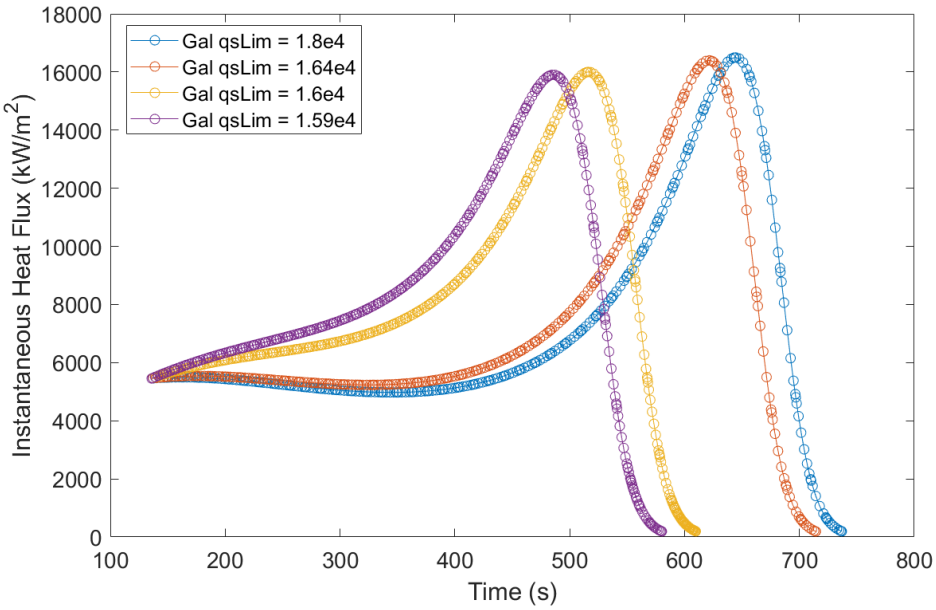

Figure 53. Steps 4-7: Stagnation point heat rate calculated with Galman model.

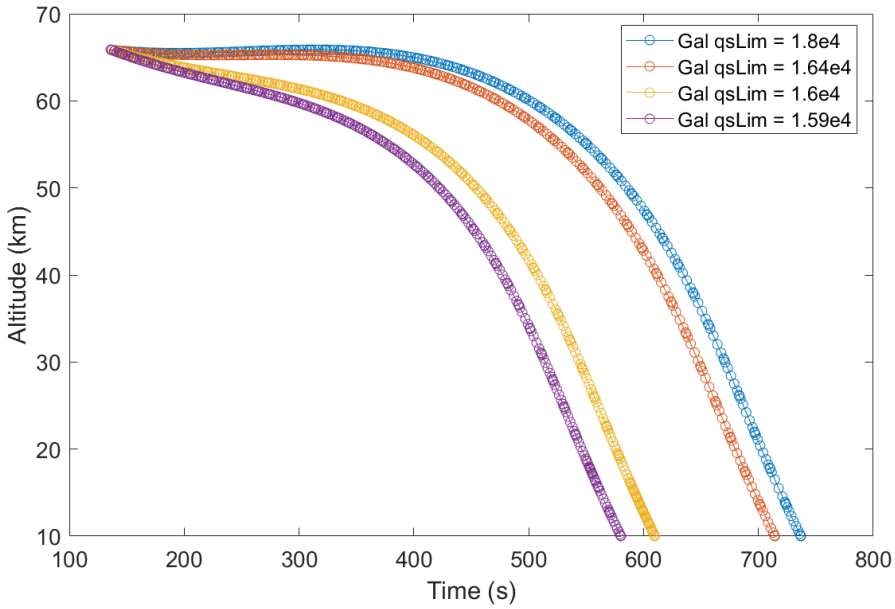

Figure 54. Steps 4-7: Altitude trajectories of system with Galman model.

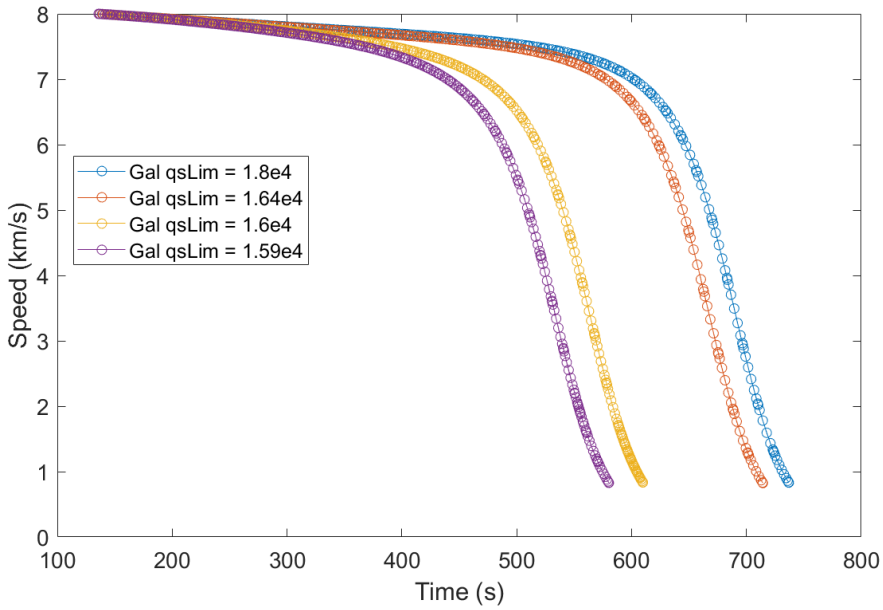

Figure 55. Steps 4-7: Speed profiles of system with Galman model.

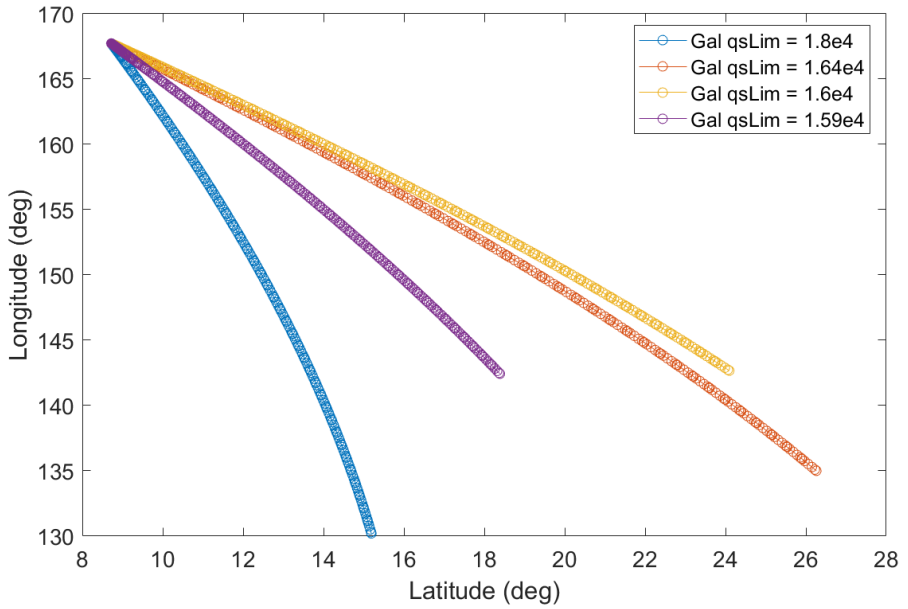

Figure 56. Steps 4-7: Vehicle position of system with Galman model.

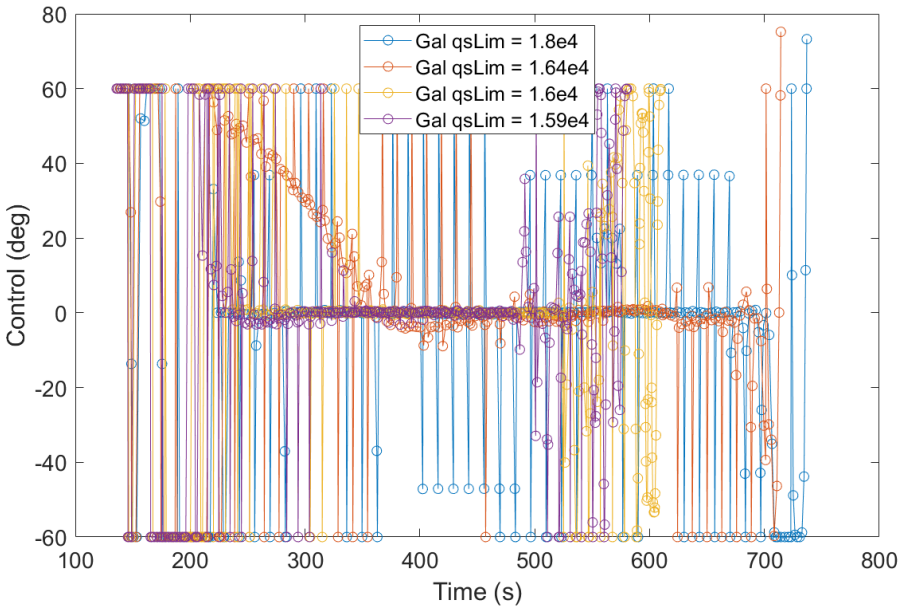

Figure 57. Steps 4-7: Control history of system with Galman model.

Appendix B. Exploration of different problem definition in Step 2

Results of Steps 0-3 with a different problem definition/mission scenario:

- Step 1: free initial states, fixed final
- Modified Step 2: **free initial altitude**, free initial latitude and longitude, fixed final
- Modified Step 3: fixed initial altitude from Modified Step 2, free initial lat/lon, fixed final

Changing Step 2 to allow for a free initial altitude resulted in the converged solution starting at the upper bound of 100 km in altitude.

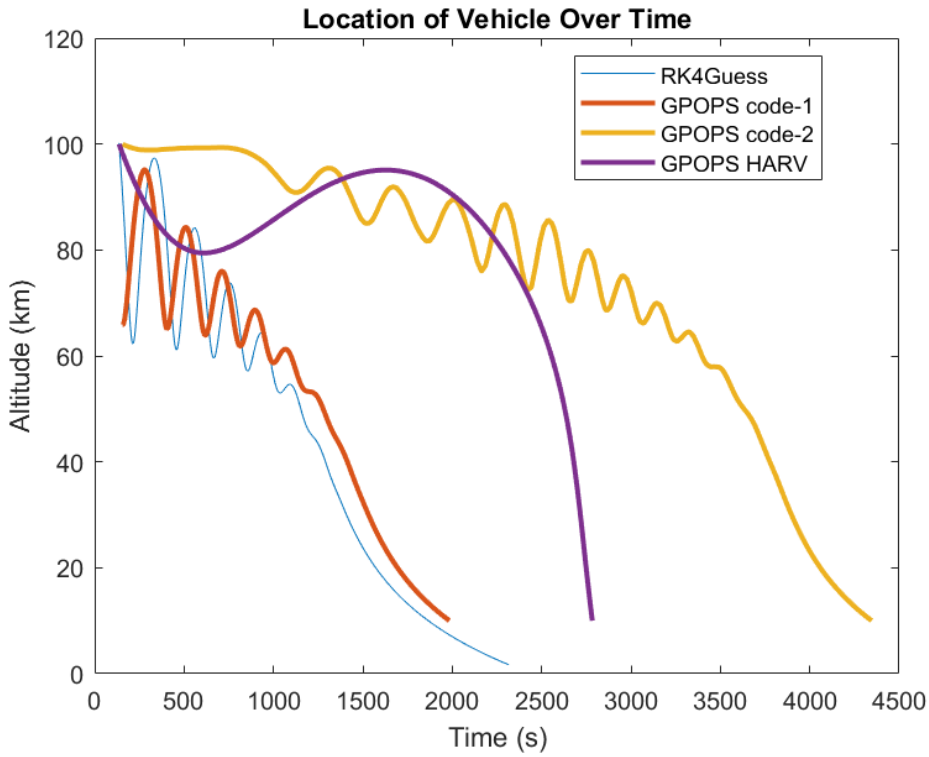

Figure 58. Altitude trajectories of modified Steps 0-3.

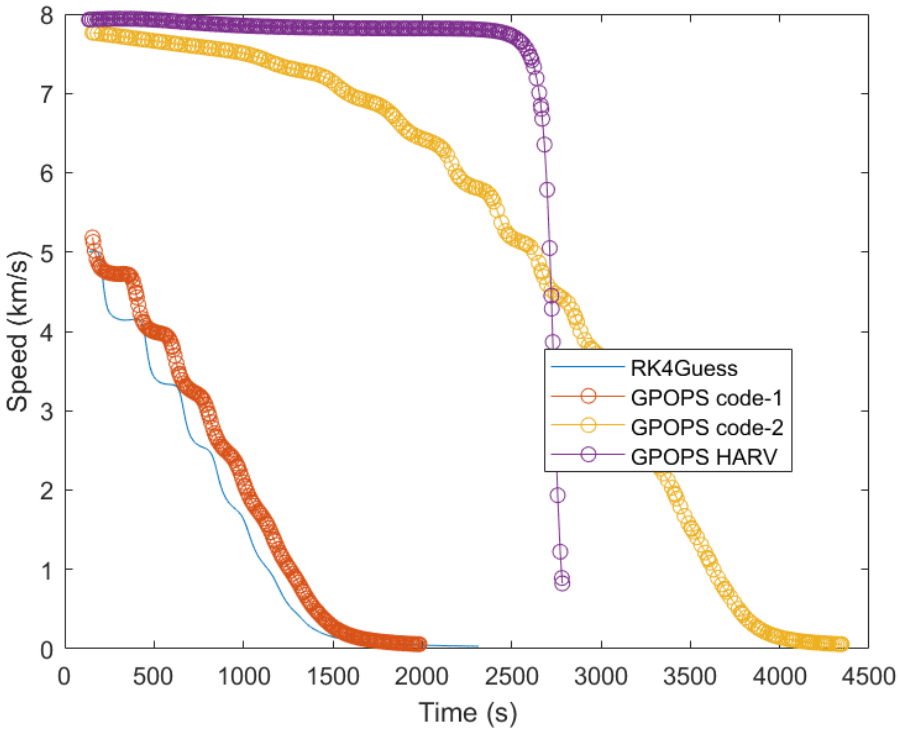

Figure 59. Speed profiles of modified Steps 0-3.

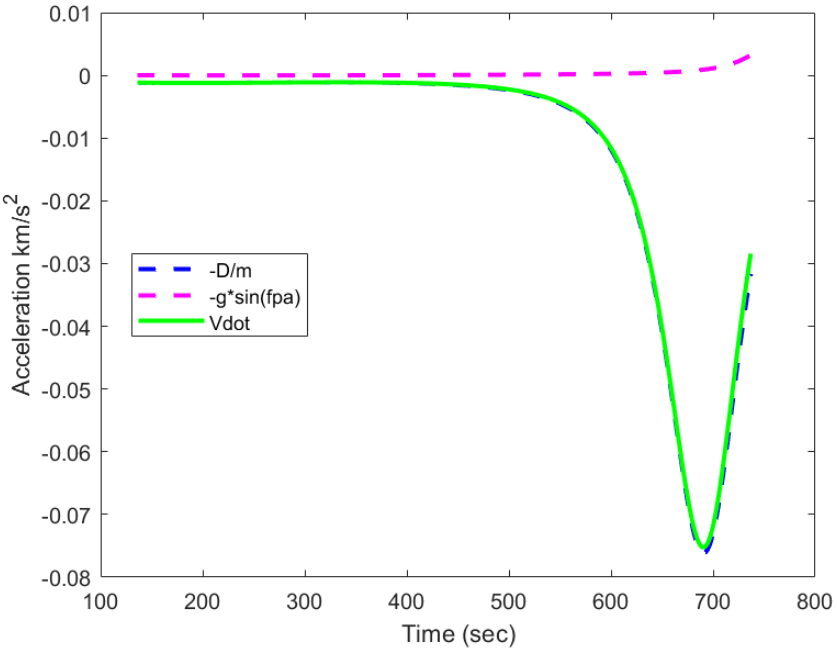

Figure 60. Acceleration components of modified Step 3.

Step 1's cost function was to maximize the longitudinal range while Modified Step 2's cost function was to maximize Euclidean range. Modified Step 2, GPOPS code-2, had a range of 12,190 km which was approximately 265% larger than Step 1's range of 3,342 km.

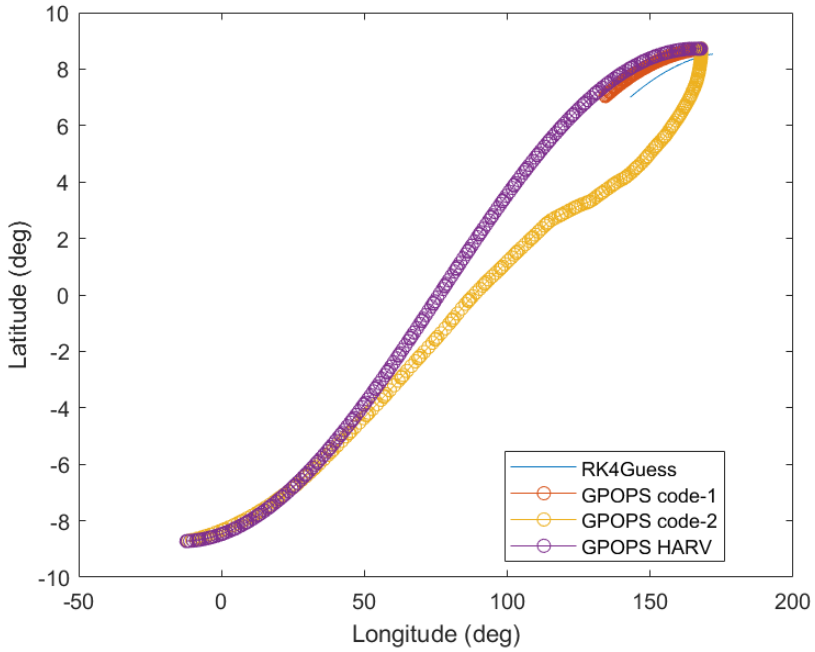

Figure 61. Vehicle position of modified Steps 0-3.

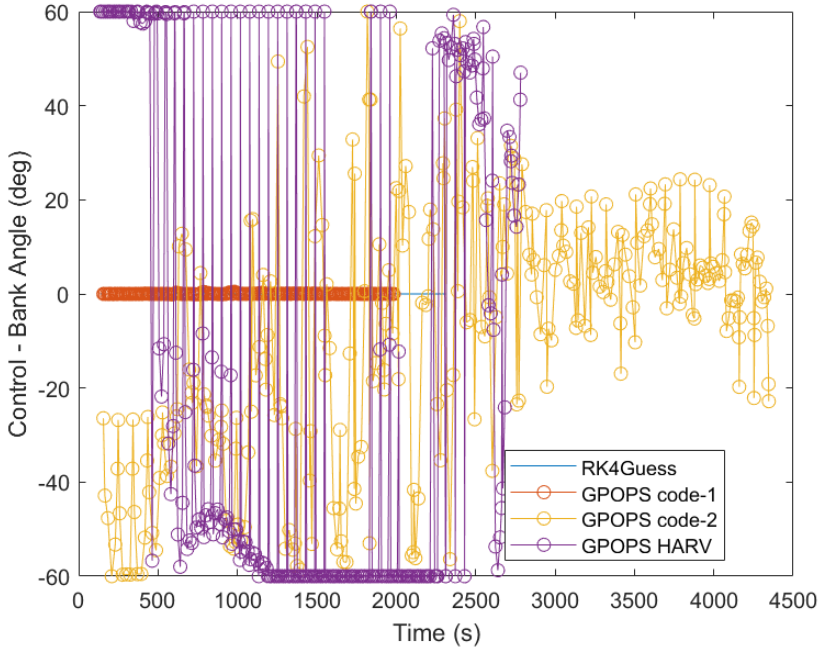

Figure 62. Control history of modified Steps 0-3.

Modified Step 3's stagnation point heat on the HARV nose was calculated with three aerothermodynamic models. The largest difference in trajectories between Step 3 and Modified Step 3 was the dive just past 500 seconds of flight time. Figure 63 shows a small increase, a bump, in stagnation point heat rate values just past 500 seconds.

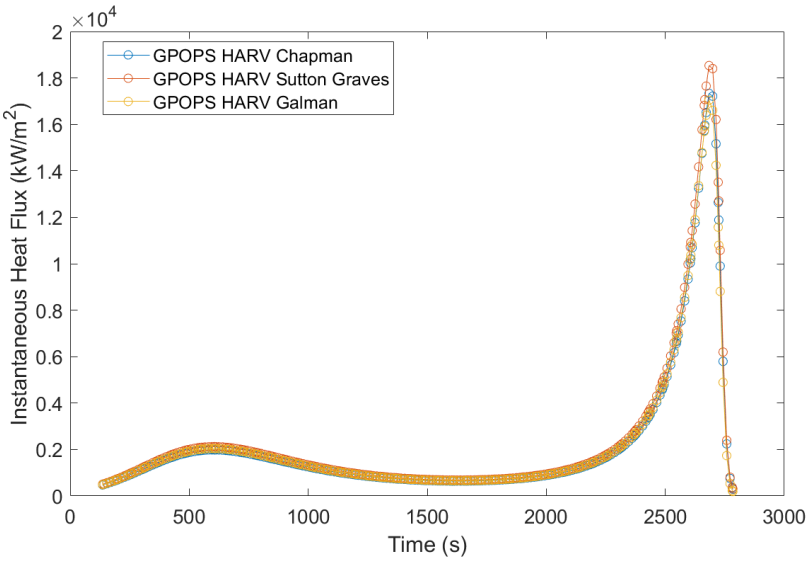

Figure 63. Modified Step 3: stagnation point heat rate on vehicle nose calculated with three aerothermodynamic models.

Appendix C. IEEE Conference Paper

Paper submission to the 2023 IEEE Aerospace Conference held in Big Sky, Montana from March 5^{th}-11^{th}. This annual conference features aerospace experts from various career fields making headway in research. The conference is aimed at promoting an interdisciplinary knowledge of aerospace systems.

Direct Collocation Methods for Hypersonic Trajectory Optimization by the Process of Continuation

Noor Khan
Department of Aeronautics and Astronautics
Air Force Institute of Technology
Wright Patterson Air Force Base, OH 45433
noor.khan@afit.edu

Michael Zollars & Robert MacDermott
Department of Aeronautics and Astronautics
Air Force Institute of Technology
Wright Patterson Air Force Base, OH 45433
michael.zollars@afit.edu; robert.macdermott@afit.edu

***Abstract*—An algorithm was created to optimize trajectories of hypersonic glide vehicles with selected cost functions by applying the process of continuation to direct orthogonal collocation methods. The trajectory was optimized to maximize the range of launch position given a fixed terminal location. The process of continuation was used to address the complexity of the model whereby less complex solutions were used to seed increasing complex modeling in an iterative fashion. The hypersonic glide vehicle system dynamics were modeled with three-dimensional, three degree of freedom equations of motion assuming no thrust and a non-rotating Earth for the states defined as vehicle radial position, latitude, longitude, speed, flight path angle, and heading angle. The control for the system was placed on the bank angle of the vehicle. The results presented here are the foundational stages of ongoing research. Use of the continuation method enabled rapid generation of optimized trajectories. Differences noted between iterations of the continuation process showed the evolution of vehicle trajectories based on the problem formulations. The continuation method was demonstrated as an effective tool for optimization.**

TABLE OF CONTENTS

1. INTRODUCTION

In today's strategic environment, there is an ever-increasing need for the development of simulation programs to accurately model the maneuverability of high-speed vehicles [1]. Globally, hypersonic vehicle programs have become active in multiple nations. In the United States, the advancement of new high-speed maneuverable weapons is part of the conventional prompt global strike program, which has been around since the early 2000s [2]. Due to the complexity of the hypersonic systems and the requirement for testing, near term deployment is not feasible without accurate and robust modeling. Hypersonic vehicles fall into three general classes: ballistic reentry vehicles, glide vehicles, and cruise vehicles. The difference in trajectories can be observed in Figure 1. Ballistic missiles follow a parabolic trajectory, with minimal control and will operate exo-atmospherically, while glide and cruise vehicles operate endo-atmospherically for the majority of their trajectory. Glide vehicles do not utilize propulsion after launch while cruise vehicles engage in powered flight. Endo-atmopsheric flight provides an advantage for hypersonic glide and cruise vehicles due to the ability to maneuver during flight. The maneuverability allows for a broader range of applications. An endo-atmospheric flight path may result in delayed detection from a terrestrial based radar due to a limiting line of sight, as illustrated in Figure 2. A radar would not detect a low flying vehicle until much later in its flight path, thus compressing the timeline for any counter measures.

Hypersonic vehicle trajectories are split into three main phases: launch, midcourse, and terminal. During endo-atmospheric flight, the same dynamics model may be employed for all types of hypersonic vehicles. Both the midcourse and terminal phases are endo-atmospheric for glide and cruise vehicles. Utilization of the same dynamics model across different phases and aircraft models allows for flexibility while using the process of continuation. Continuation is the process of solving a less complicated problem and using it as the initial seed to a more complicated problem. Simulated path trajectory solutions are solved with direct orthogonal collocation methods which are popular in this field, due to the ability to easily accommodate multiple phases. For example, including the launch phase, in addition to the midcourse and terminal phase, would warrant an additional phase with different dynamics. Each set of dynamics correlating to each phase must satisfy continuity of the states, control, and time for the complete trajecotry through the implementation of event constraints. Another multi-phase approach may be considered for a single phase of flight. For example, the midcourse phase may be divided into segments based on researcher interest, specific constraints only applicable to a certain section of the trajectory, or others.

2. BACKGROUND

Research in hypersonic trajectory optimization incorporates multiple disciplines. Knowledge of hypersonic flow, aerothermal models, vehicle models, and optimal control theory among other topics are required. Many different methods for solving hypersonic trajectories have been explored, from indirect optimization methods to neural networks [4]. Each has their advantages and short-comings. Deep neural networks or machine-based learning have shown promise with viable results [4][5]. The primary issues with machine-based learning are the time required and the quantity of data needed to train the algorithm [6]. Any changes to the mission profile or modifications of the vehicle may require a new set of training data for the algorithm. Therefore, flexibility is of paramount importance for a widely applicable program that can respond to changing circumstance and rapidly generate new trajectories. One of the challenges of research with hypersonics is the unique aspects of the flow regime.

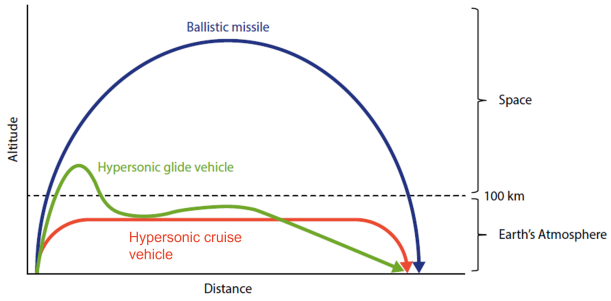

Figure 1: **Trajectories of a ballistic missile, a hypersonic glide vehicle (HGV), and a hypersonic cruise vehicle (HCV) [3].**

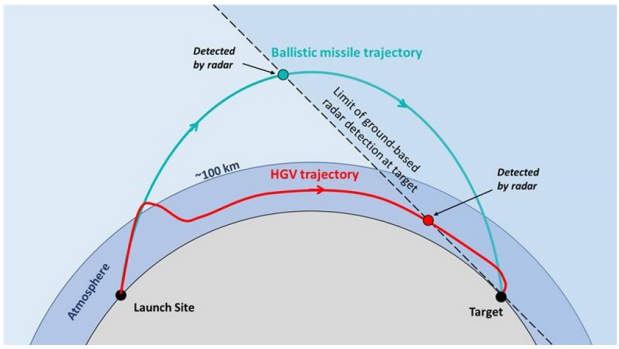

Figure 2: **Radar detection of a ballistic missile vs a hypersonic glide vehicle (HGV) [1].**

Hypersonic flow fields differ significantly from subsonic and even supersonic flows. The defining characteristic of hypersonic flows is that the kinetic energy of the freestream is large compared to the internal thermodynamic energy of the fluid particles [7]. Different physical phenomena occur when the kinetic energy transforms. Anderson [8] identified several defining phenomena that illustrate the differences between hypersonic flow and slower flow regimes, among which include thin shock layers, the entropy layer, viscous interactions, and high temperature flow. The flow field will experience high temperatures in the thousands of Kelvin. At these high temperatures, the flow field's molecules will experience chemical reactions and thus be in a chemical non-equilibrium as well as exciting the internal energies of the molecules resulting in a thermodynamic non-equilibrium. The imbalance of internal and translational energies of the molecules means a hypersonic vehicle will encounter extreme aerothermodynamic heating.

Another challenge with hypersonic bodies is integrating the coupled disciplinary sub-systems into a model with constraints to produce rapid, robust, and optimal trajectories [9]. Summarized in Figure 3 are two methods for solving optimal control problems: indirect and direct [10]. The indirect method solves a two-point boundary value problem by solving the necessary conditions for optimality. Derivatives for each condition of optimality must be found to solve a problem. While indirect methods uses gradient based techniques to solve for the derivatives, direct methods take advantage of numerical linear algebra. As the problem's complexity grows, the solution for the derivatives for the necessary conditions of optimality becomes intractable. Therefore, indirect methods are only feasible for a relatively simple problem and solution set. In a hypersonic trajectory optimization problem, the nonlinear system dynamics, constraints, and bounds make it intractable for using indirect methods. Therefore, direct methods are necessary for realistic optimal hypersonic trajectory optimization solutions. Direct methods use Gaussian quadrature, which solves the problem exactly at defined collocation points. Between those points, the solution is approximated with Legrange polynomials [11]. Gaussian quadrature is used to approximate the running cost and is fundamental to direct collocation methods.

GPOPS-II is a direct orthogonal collocation algorithm that incorporates a phased structure for the solution based on different dynamic models or system parameters [12]. Work by Jorris [13], Masternak [14], and Coulter [9] among others, used GPOPS II for hypersonic trajectory optimization. The aforementioned research projects resulted in feasible solutions. Each had a slight variation on the type of vehicle, the assumptions implemented on the equations of motion, and the optimal control problem formulation i.e. the cost function, bounds, and constraints. The results from such projects develop intuition for feasible trajectories.

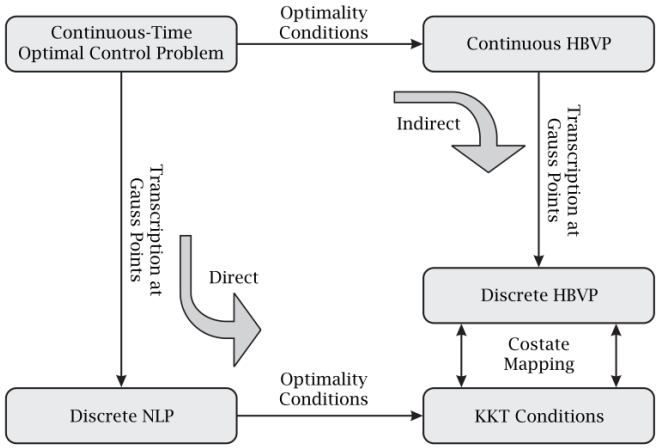

Figure 3: **Indirect vs direct methods of optimal control theory [10].**

3. METHODS

The hypersonic trajectory problem was solved via direct orthogonal collocation methods utilizing the GPOPS-II algorithm while implementing the method of continuation. The project presented in this paper focused on solving an optimal trajectory for maximizing the range of a hypersonic glide vehicle (HGV) during its glide phase. The characteristics of the chosen vehicle model are utilized in the equations of motion to provide a more realistic solution. Incorporation of vehicle characteristics increases the fidelity of the model. For example, calculating lift and drag require the reference area of the vehicle. This project modeled a generic vehicle without an engine. The vehicle's properties were based on the Common Aero Vehicle [15]. A second HGV was also modeled after the High-speed Army Reference Vehicle (HARV) [16]. The HARV was chosen because it was created with the mission of providing a model "suitable for foundational research to allow for focused collaboration" [16]. Due to the adaptable nature of the HARV, no aerodynamic tables are provided with the model. Figure 4 shows one possible

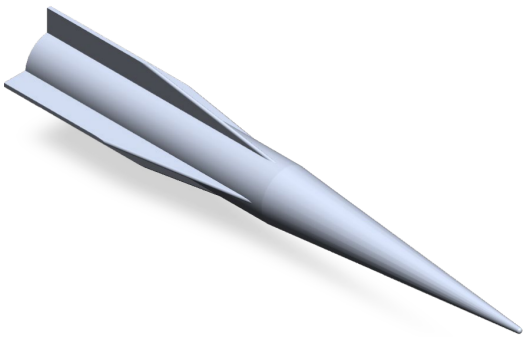

Figure 4: **HARV configuration with a conical nose and four fins [16].**

configuration of the HARV with a conical nose and four tail fins.

Gravity was calculated as a function of the vehicle's radial position while atmospheric density was calculated with a simple exponential relationship. The coefficients of lift and drag remained as constants. For the first few iterations of code using the CAV-inspired model, the coefficient of lift was set to 2 and the coefficient of drag was set to 1. These values were chosen to represent a lifting body with a L/D that is greater than 1. The mass was set as 1000 kg and the wetted area as 4.4 m^2. The HARV characteristics assumed a lift coefficient of 0.01 and a drag coefficient of 0.7. These lift and drag values were chosen from common values of rocket missiles [17]. The mass was set to 150 kg and the wetted area as 2 m^2 [18]. The dynamics of the system are represented in the code with first order differential equations of motion.

The gravitational acceleration of the vehicle was calculated with Equation 1. Atmospheric density was calculated with an exponential model in Equation 2. Lift and drag were calculated with Equations 3 and 4.

$$g = g_0(\frac{R_e}{r})^2 \tag{1}$$

$$\rho = \rho_0 \exp^{-\beta(r-Re)} \tag{2}$$

$$L = \frac{C_L V^2 \rho S}{2} \tag{3}$$

$$D = \frac{C_D V^2 \rho S}{2} \tag{4}$$

Earth's gravitational constant, g_0, is defined as 9.8 $\frac{m}{s^2}$, R_e is the Earth's radius at 6371 km, ρ_0 is the density at sea level at 1.225 $\frac{kg}{m^3}$, β is a scale height set at 0.14, and S is the reference area of the vehicle.

Equations of Motion

The equations of motion (EOMs) used herein are common trajectory reentry equations. The equations of motion were derived with the following assumptions: a constant Earth rotation ω, drag parallel and opposite to velocity, lift perpendicular to velocity, and the gravity vector parallel to the vehicle position vector. The vehicle is modeled as a pseudo-point mass. In a physical system, the coefficient of lift and drag would be based on the vehicle's orientation, however, inclusion of orientation based aerodynamic forces is beyond the scope of the current investigation. The vehicle was assumed to have no thrust representing the glide phase of an HGV. The rotation of the Earth was assumed to be negligible. Neglecting Earth's rotation is valid due to the difference in relative speeds between a hypersonic vehicle and the Earth's rotation. The simplified 3D equations of motion are as follows:

$$\dot{r} = Vsin(\gamma) \tag{5a}$$

$$\dot{\theta} = \frac{Vcos(\gamma)cos(\psi)}{rcos(\phi)} \tag{5b}$$

$$\dot{\phi} = \frac{Vcos(\gamma)sin(\psi)}{r} \tag{5c}$$

$$\dot{V} = -\frac{D}{m} - gsin(\gamma) \tag{5d}$$

$$\dot{\gamma} = \frac{L}{Vm}cos(\sigma) - \frac{g}{V}cos(\gamma) + \frac{V}{r}cos(\gamma) \tag{5e}$$

$$\dot{\psi} = \frac{Lsin(\sigma)}{mcos(\gamma)V} - \frac{V}{r}cos(\gamma)cos(\psi)tan(\phi) \tag{5f}$$

where the vehicle's position vector is r, longitude is θ, latitude is ϕ, speed is V, flight path angle is γ, and heading angle is ψ. The bank angle is defined as σ.

Continuation

Continuation is the method of solving a less complex problem and using its solution to seed a more complicated problem, then using the subsequent solution to seed an even more complicated problem. The process is repeated until a solution is found for the problem at the desired level of complexity. Continuation is beneficial for hypersonic trajectory optimization as complexities can be slowly added into the problem formulation while maintaining tractable solutions.

Continuation was used for this research effort over four iterations of the problem formulation. The initial seed fed into the first round of GPOPS-II code was a Fourth-Order Runge-Kutta (RK4) solution for the generic hypersonic vehicle. The RK4 method is an iterative method that generates approximate solutions to ordinary differential equations. The solution of the first set of GPOPS-II code, referred to as the GPOPS code-1,was used to seed the next iteration of the optimal solution. The second iteration of GPOPS-II code, which also used the generic hypersonic vehicle characteristic data, is referred to as GPOPS code-2. The last iteration of GPOPS-II code presented in this paper used HARV characteristic data and is referred to as GPOPS HARV. The specifics of the GPOPS-II codes are covered in the section on Problem Formulation.

Problem Formulation

The generic optimal control problem formulation consists of a system modelled with ordinary differential equations (ODEs), bounds, and a cost function. A cost function, or performance measure, provides the ability to quantitatively

assess a system's performance [11]. The goal of an optimization problem is to find the control that will minimize or maximize the performance index. The cost function is chosen either by necessity from the problem or subjectively by the researcher [11].

Both the GPOPS code-1 and GPOPS code-2 had the same dynamics and vehicle model. The system was modeled with three-dimensional three degree of freedom (3D 3DOF) EOMs, defined in Equations 5a-5f. The states ($\mathbf{y}$) were vehicle position from the center of the Earth, latitude, longitude, speed, flight path angle, and heading angle.

$$\mathbf{y} = \begin{bmatrix} r \\ \phi \\ \theta \\ V \\ \gamma \\ \psi \end{bmatrix} \tag{6}$$

The control ($\mathbf{u}$) was bank angle.

$$\mathbf{u} = \sigma \tag{7}$$

Bounds on the variables in the code for the GPOPS code-1, code-2, and HARV are summarized in Table 1. The altitude bound is expressed through the vehicle position radius with the lower bound being the Earth's radius and the upper bound being the initial radius of the vehicle. For GPOPS code-1, the upper bound was 100km above the Earth's radius. r0 in this case happened to be 6437 km. Altitude, or vehicle position radius, was bound to the continuum flow region where lift and drag may be calculated using aerodynamic principles.

Table 1: **Variable bounds for GPOPS code-1, code-2, and HARV**

Variable	Min	Max
Time (t) - seconds	0	7000
Vehicle position radius (r) - km	6371	r0
Speed (V) - km/s	0.01	8
Longitude (θ) - radian	-π	π
Latitude (ϕ) - radian	-$\pi/2$	$\pi/2$
Flight path angle (γ) - radian	-$\pi/2$	$\pi/2$
Heading angle (ψ) - radian	0	2π
Bank angle (σ) - radian	-$\pi/3$	$\pi/3$

The setup of all the GPOPS-II code iterations was configured with the options in Table 2. Details on the settings can be found in the GPOPS-II User Guide [19].

Table 2: **GPOPS-II Mesh and Setup Options**

Option	Setting
mesh.method	hp-PattersonRao
mesh.tolerance	1×10^{-4}
setup.nlp.solver	snopt
setup.scales.method	automatic-bounds
setup.method	RPM-Integration

The cost function of the GPOPS code-1 code was maximizing longitudinal range as a converged solution could easily be obtained for the continuation process. This cost function was arbitrarily chosen as a starting point for the optimization algorithm. Longitudinal range can be found as a cost function in other literature [20][14].

$$\min_{u*\in U} J = -\theta \tag{8}$$

No path constraints were enforced during this iteration. Table 3 shows the set up for the initial and final conditions on the problem in the GPOPS code-1. The initial vehicle radius, latitude, and longitude are left free to allow the algorithm to converge on an optimal starting position for the given cost function. The final latitude and longitude was set to the coordinates of the Kwajalein Atoll US military base in the Marshall Islands.

Table 3: **Initial and final conditions for GPOPS code-1**

Variable	Initial	Final
Time (t) - seconds	0	free
Vehicle position radius (r) - km	free	6381
Speed (V) - km/s	free	free
Longitude (θ) - radian	free	2.9274
Latitude (ϕ) - radian	free	0.1522
Flight path angle (γ) - radian	free	free
Heading angle (ψ) - radian	free	free
Bank angle (σ) - radian	free	free

The cost function for the GPOPS code-2, which used the solution from GPOPS code-1 as the initial seed, was maximizing the Euclidean range as shown in Equation 9. The states were converted into the Cartesian plane with Equations 10-12 and a simple euclidean distance was calculated for the cost function.

$$\min_{u*\in U} J = -(x_2 - x_1)^2 + (y_2 - y_1)^2 + (z_2 - z_1)^2 \tag{9}$$

$$x = rcos(\phi)cos(\theta) \tag{10}$$

$$y = rcos(\phi)sin(\theta) \tag{11}$$

$$z = rsin(\phi) \tag{12}$$

The subscripts 1 and 2 denote initial and final positions, respectively. Although the Euclidean distance is not a realizable flight path, it is directly related to the true flight path as described by the system dynamics. In other words, even though the euclidean range is not a feasible flight path, the trajectory solution will be accurate since the system dynamics are not violated in the state solution.

For the GPOPS code-2 and HARV solutions, no path constraints were enforced on the system. The initial and final conditions on the problem for GPOPS code-2 are listed in Table 4. The problem was free final time, fixed final state, specifically fixing the final radial position, latitude, and longitude.

The goal was to find where the vehicle should start its glide phase to maximize range and still meet the fixed final target.

Table 4: **Initial and final conditions for GPOPS code-2 and HARV**

Variable	Initial	Final
Time (t) - seconds	0	free
Vehicle position radius (r) - km	6437	6381
Speed (V) - km/s	free	free
Longitude (θ) - radian	free	2.9274
Latitude (ϕ) - radian	free	0.1522
Flight path angle (γ) - radian	free	free
Heading angle (ψ) - radian	free	free
Bank angle (σ) - radian	free	free

The initial radial position of GPOPS code-2 and GPOPS HARV was fixed based off the initial radial position of the GPOPS code-1 result which was 66 km above the Earth's surface.

4. RESULTS

The process of continuation applied to the GPOPS algorithm successfully converged on optimal solutions based on the given criteria as indicated by the exit flags of "0 – finished successfully" and "1 – optimality conditions satisfied" from GPOPS-II for all iterations. Figures 5 and 6a clearly show the difference in trajectories between each iteration of code. The GPOPS-II algorithm is sensitive to the initial seed [12] which explains the similar graph shapes between the RK4Guess and the GPOPS code-1 since the RK4Guess was used as the initial seed for the GPOPS code-1. As the continuation process reaches the GPOPS HARV trajectory, it is seen in Figure 5 the skipping in the path trajectory has been eliminated since previous iterations had L/D values greater than one to represent a lifting body, while the HARV data had an L/D value less than one.

Figure 6a illustrates that the GPOPS-II codes solved for the optimal initial latitude and longitude for the vehicle to maximize its range while still ending on the fixed position. The initial latitude and longitude did not reach the bounds of the variables set in Table 1, indicating that the initial points are optimal for the problem formulation. GPOPS code-1 resulted in an initial altitude of 66 km, which was then used as the initial altitude for the next two iterations.

Figure 6a shows the difference in ranges of each iteration. Through the continuation process the Euclidean range was increased from 3,342 km in GPOPS code-1 to 3,397 km for GPOPS HARV. The objective for GPOPS code-1 was to maximize longitude only. Figure 6a confirms the objective as very little variation is shown in the latitude direction. With GPOPS code-2, the objective transitions to maximize the Euclidean range. The change in latitude is more significant given the flexibility with the additional dimensions of the cost function. Finally, when incorporating the HARV data with maximizing Euclidean range, the largest distance was acquired. Many factors such as the weight and aerodynamic properties of the vehicle as well as the speed profile of the HARV contributed to this final trajectory. A majority of the HARV trajectory was at a higher speed than the generic HGV solutions as can be observed in Figure 6c. Mainly, the ranges demonstrate that continuation allowed for a maximum range trajectory solution to the vehicle specific properties given a generic starting trajectory with a propagated solution.

The control history of the HARV, shown with the purple line in Figure 6b, shows bang-bang control for the entire flight path. Bang-Bang control indicates an optimal solution. However, bang-bang control is not necessarily a realistic control to implement in flight. To alleviate this issue, implementing bank angle as a state and bank angle rate as the control would produce a realizable input for the bank angle of the vehicle, effectively applying a rate limit.

The speed of the vehicle decreased as it approached its final destination for every iteration as shown in Figure 6c due to the influence of drag. Figure 7 shows each term of the vehicle acceleration, Equation 5d, for the GPOPS HARV solution plotted on the same graph. The drag term dominates the change in speed, calculated with Equation 5d. Approximately 600 seconds into the trajectory, the drag is seen to increase as the vehicle approaches the Earth's surface due to the increased density, calculated with Equation 2.

The significant differences between the simple iterative Runge-Kutta guess and the follow on optimized solutions shows the power of continuation. The code took just under 100 seconds to complete all iterations of the continuation process on an HP Elitebook with an Intel Core i7 8th generation processor.

5. CONCLUSION

The recent development of maneuverable hypersonic vehicles has spurred an increase of research in the field. Hypersonic weapons have advantages over traditional ballistic missiles. Hypersonic weapons are able to maneuver during flight and stay at lower altitudes which makes detection more challenging when compared to traditional ballistic trajectories. Direct orthogonoal collocation methods were employed to solve for an optimized hypersonic trajectory via the pseudospectral solver called GPOPS-II. The process of continuation was applied since the hypersonic trajectory optimization problem is a complicated problem and the GPOPS-II algorithm requires a sufficient seed input. Continuation enabled the use of a simple seed and a simple initial problem that was then propagated to reach the solution for a more complex problem.

Two HGVs were modeled in the continuation process to accomplish the converged trajectory of the HARV model. Converged solutions were produced for the glide phases of two HGVs, one generic lifting body based on the CAV model and the HARV, both without constraints. Three dimensional (3D), three degree of freedom (3DOF) equations of motion (EOMs) with the assumptions of no thrust and a non-rotating Earth were the system dynamics. Bank angle was set as the control.

Iterations of code began with a simple Fourth-Order Runge-Kutta (RK4) iteration of the generic HGV, which was used to seed the first iteration of GPOPS-II code. The first iteration of GPOPS-II code optimized the trajectory to maximize longitudinal range. The solution was used to seed the next iteration of GPOPS-II code which optimized its solution to maximize the Euclidean range. The last iteration of GPOPS-II code presented an optimized solution to maximize the Euclidean range with the difference of using HARV characteristics. Converged solutions were achieved for each iteration in the continuation process. The flight path of the generic HGV followed a skipping trajectory, typical of lifting bodies. The influence of the guess fed into the code was observable with the general shape of the solution. Each iteration in the continuation process showed a perceptible difference. The final

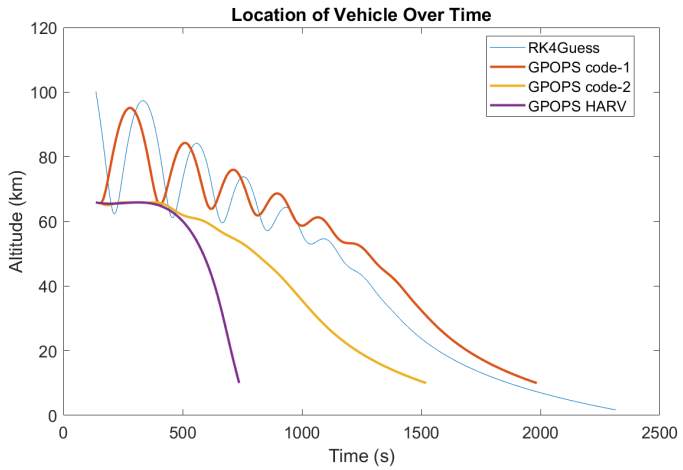

Figure 5: **Altitude trajectory of hypersonic vehicle.**

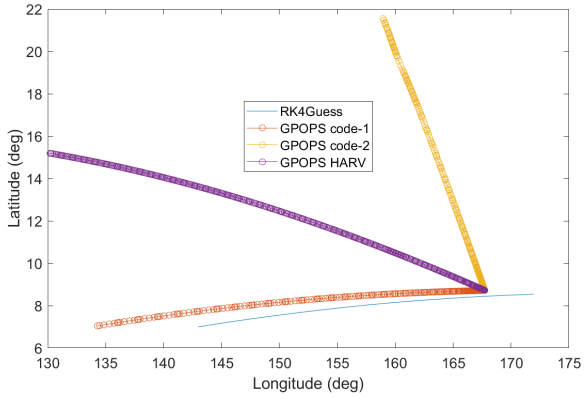

(a) Latitude and longitude of vehicle over time.

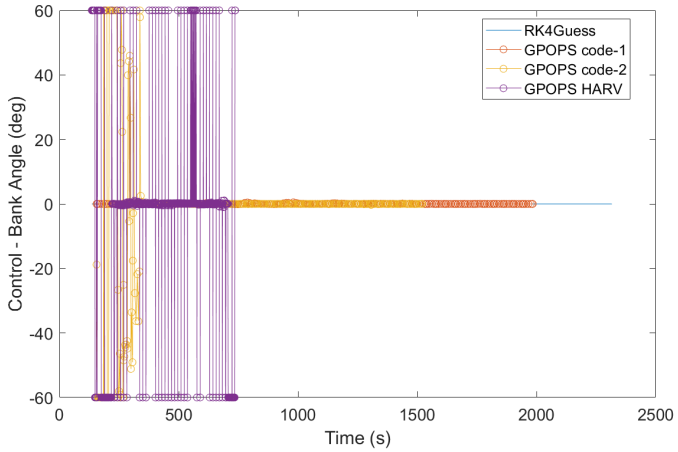

(b) Control as bank angle of vehicle over time.

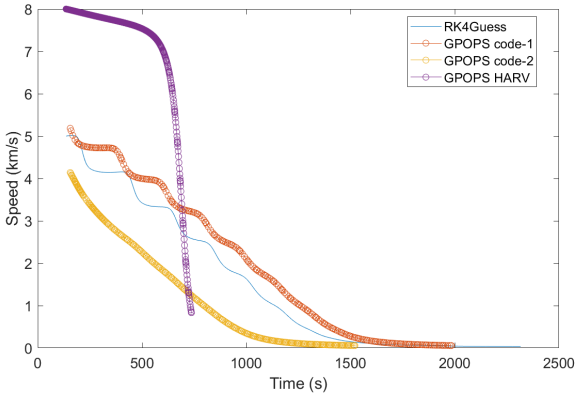

(c) Speed of vehicle over time.

Figure 6: **Results of trajectories of the vehicle position (a), control (b), and speed profile (c).**

solution compared to the initial RK4 guess was noticeably different. The results in Figures 5 and 6 show promise for future use of continuation.

The largest contribution of this research was demonstrating the utility of the continuation process. This effort exhibited the ease of implementation of continuation for various problem formulations. The continuation process alleviated a common issue of providing the GPOPS-II algorithm with a sufficient guess to a complicated problem. Solutions to optimal trajectories with HARV data require either an intelligent guess to initiate the algorithm or utilizing the method of

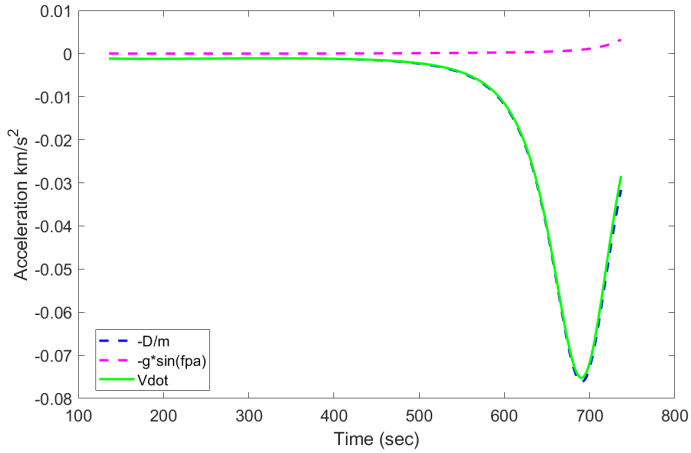

Figure 7: **Each component of Equation 5d from the GPOPS HARV data.**

continuation.

6. Future Work

There are many directions that the current project can be taken in. Some of these include adding a rate law for a more realistic control history, increasing the fidelity by adding lift and drag calculations, and extending the scope to include the launch phase of flight, to name a few. It is also important to note the sensitivity of the GPOPS-II algorithm to variable bounds. A common challenge encountered are the effects of minor changes on variable bounds, whether the bounds are too big or too small, being the reason for convergence. This problem can be eliminated with non-dimensionalization of the problem. While this research effort did not find bounds to be a limiting factor of convergence, it is important to acknowledge for the future.

Constraints

The next step in research would be incorporating constraints on the system to achieve higher fidelity results. The temperatures experienced by a vehicle during hypersonic flight are extreme and must be modeled. The project aims to compare the resultant trajectory with the implementation of various aerothermal heating models. The aerothermal models will be incorporated as path constraints with a maximum heat flux not to be exceeded. Chapman [21], Sutton-Graves [22], and Galman [23] equations are three simple heat flux equations that are comparable. A higher fidelity aerothermal heating model would be Eckert's reference enthalpy.

Reference enthalpy or reference temperature methods take into account compressibility effects in a simplified manner via some reference temperature inside the boundary layer [8]. These methods are better suited for slender bodies [9] and preferred for analysis due to simplicity of application to hypersonic problems [8].

Additionally, the vehicle can experience enormous forces at high speeds that would need to be constrained to ensure its survival. Load and dynamic pressure path constraints would address those forces [24]. All aforementioned constraints appended to the system will work to achieve more realistic results.

Lift and Drag

Including variable lift and drag values would increase model fidelity. There are multiple ways to include non-constant lift and drag. The two main avenues are aerodynamic look-up tables [13] [25] [14] and surface pressure distribution calculations [26] [9]. Aerodynamic look-up tables can be acquired via empirical data or from CFD analysis. Empirical data is compiled from flight test data. Empirical look-up tables are convenient but only when available. CFD analysis is another method to achieve aerodynamic look-up tables. CFD uses various modeling techniques to calculate and produce the required look-up tables. Different equations of varying fidelities can be used to calculate surface pressure distributions. Lift and drag can be extracted from the surface pressure distribution equations which can be incorporated into GPOPS-II and calculated within the code. Since empirical data is not available for the vehicle models used in this research effort, future work will include lift and drag calculations with a surface inclination method called Lee's Modified Newtonian Method (MNT).

Phases of Flight

Finally, expanding the scope of the project to include additional phases of flight like the launch and terminal phases is another progression. Additionally, incorporating a cruise phase of flight can be achieved. These phases of flight have different dynamics which can easily be accommodated with the GPOPS-II algorithm. Particularly the addition of a propulsion model is required for the launch and cruise phases. The end goal of the continuation process is to have a complete feasible result of the entire flight path of a hypersonic vehicle. This work is important to furthering the knowledge of hypersonic trajectories and the coordination of various disciplines.

Acknowledgments

The authors thank the Air Force Research Laboratory for funding this project.

References

[1] K. M. Sayler, "Hypersonic weapons: Background and issues for Congress," *Key Congressional Reports for*

July 2019. Part I, pp. 161–194, 2019.

[2] A. F. Woolf, "Conventional prompt global strike and long-range ballistic missiles: Background and issues (updated)," *Key Congressional Reports for August 2019: Part IX*, pp. 181–264, 2020.

[3] S. R. Aarten, "The Impact of Hypersonic Missiles on Strategic Stability," *De militaire spectator*, pp. 182–193, 2020.

[4] Y. Shi and Z. Wang, "A deep learning-based approach to real-time trajectory," pp. 1–19, January 2020.

[5] K. Sachan and R. Padhi, "Nonlinear robust neuro-adaptive flight control for hypersonic vehicles with state constraints," *Control Engineering Practice*, vol. 102, August 2020.

[6] X. Hui, C. Guangbin, Z. Shengxiu, Y. Xiaogang, and H. Mingzhe, "Hypersonic reentry trajectory optimization by using improved sparrow search algorithm and control parametrization method," *Advances in Space Research*, vol. 69, no. 6, pp. 2512–2524, 2022.

[7] J. J. Bertin, *Hypersonic Aerothermodynamics*. Washington, D.C.: American Institute of Aeronautics and Astronautics Conference, 1994.

[8] J. D. Anderson Jr., *Hypersonic and High Temperature Gas Dynamics*, 2nd ed., Reston, 2006.

[9] B. Coulter, Z. Wang, D. Huang, and Y. Yao, "Hypersonic trajectory optimization with high-fidelity aerothermodynamic models," *AIAA Scitech 2021 Forum*, pp. 1–17, January 2021.

[10] D. A. Benson, G. T. Huntington, T. P. Thorvaldsen, and A. V. Rao, "Direct trajectory optimization and costate estimation via an orthogonal collocation method," *Collection of Technical Papers - AIAA Guidance, Navigation, and Control Conference 2006*, vol. 4, pp. 2731–2744, August 2006.

[11] D. E. Kirk, *Optimal Control Theory: an introduction*. Mineola: Dover Publications, Inc., 1998.

[12] M. A. Patterson and A. V. Rao, "CGPOPS: A C++ Software for Solving Multiple-Phase Optimal Control Problems Using Adaptive Gaussian Quadrature Collocation and Sparse Nonlinear Programming," *ACM Transactions on Mathematical Software*, vol. 41, no. 1, 2014.

[13] T. R. Jorris, "Common aero vehicle autonomous reentry trajectory optimization satisfying waypoint and no-fly zone constraints," 2007.

[14] T. J. Masternak, "Multi-Objective Trajectory Optimization of a Hypersonic Reconnaissance Vehicle with Temperature Constraints," *AFIT Dissertations and Theses*, June 2014.

[15] M. A. Dunkel, "The impact of atmospheric fluctuation on optimal boost hypersonic vehicle dynamics," *The Air Force Institute of Technology*, 2017.

[16] J. D. Vasile, F. Fresconi, J. Despirito, M. Duca, T. Recchia, B. Grantham, D. W. Rodney, and E. B. White, "High-Speed Army Reference Vehicle," 2022.

[17] Woodbank Communications Ltd, "Simple missile ballistics, orbits and aerodynamics," 2005.

[18] US Air Force. AIM-120 AMRAAM. Accessed on January 2023. [Online]. Available: https://www.af.mil/About-Us/Fact-Sheets/Display/Article/104576/aim-120-amraam/

[19] M. A. Patterson and A. V. Rao, "GPOPS-II manual: A General-Purpose MATLAB Software for Solving Multiple-Phase Optimal Control Problems Version 2.3," pp. 1–72, December 2016.

[20] G. Duan, Y. Sun, M. Zhang, Z. Zhang, and X. Gao, "Aerodynamic coefficients models of hypersonic vehicle based on aero database," *Proceedings - 2010 1st International Conference on Pervasive Computing, Signal Processing and Applications, PCSPA 2010*, pp. 1001–1004, 2010.

[21] G. T. Chapman, "Theoretical Laminar Convective Heat Transfer and Boundary-Layer Characteristics on Cones at Speeds to 24 km/sec," Ames Research Center, Moffett Field, CA, Tech. Rep. NASA TN D-2463.

[22] K. Sutton and R. A. Graves, Jr., "A General Stagnation-Point Convective-Heating Equation for Arbitrary Gas Mixtures," NASA Langley Research Center, Hampton, VA, Tech. Rep. NASA TR R-376, November 1971.

[23] B. A. Galman, "Some Fundamental Considerations For Lifting Vehicles in Return From Satellite Orbit," *Planetary and Space Science*, vol. 4, pp. 399–410, 1961.

[24] V. R. Makkapati, J. Ridderhof, P. Tsiotras, J. Hart, and B. Van Bloemen Waanders, "Desensitized Trajectory Optimization for Hypersonic Vehicles," *IEEE Aerospace Conference Proceedings*, vol. 2021-March, 2021.

[25] L. G. Hood, G. Bennett, and J. J. Parish, "Model fidelity studies for rapid trajectory optimization," *AIAA Scitech 2019 Forum*, January 2019.

[26] S. R. Kadam and H. B. Hablani, "Trajectory optimization of reentry capsule," *IFAC Proceedings Volumes (IFAC-PapersOnline)*, vol. 3, pp. 68–74, 2014.

BIOGRAPHY

Noor Khan *received her B.S. degree in aeronautical engineering USAFA. She graduated in 2021 and continued to pursue a higher education by attending AFIT. She is currently a graduate student at AFIT working on obtaining her master's degree from the Dept of Aeronautics and Astronautics. After graduate school, she will be headed to pilot training.*

Michael Zollars *received a B.S. in Mechanical Engineering from the Pennsylvania State University in 2003 and an M.S. and PhD in Aeronautical Engineering from the Air Force Institute of Technology in 2007 and 2018 respectively. He is a professor with the Department of Aeronautics and Astronautics at the Air Force Institute of Technology. His research interests include optimal control for vehicle trajectory analysis and dynamics and control of aircraft systems.*

Robert MacDermott *received a B.S. in Aerospace Engineering from Purdue University in 2005 and an M.S. and PhD in Aeronautical Engineering from the Air Force Institute of Technology in 2012 and 2021 respectively. He is an assistant professor with the Department of Aeronautics and Astronautics at the Air Force Institute of Technology. His research interests include experiment and computational investigations of hypersonic phenomena.*

Bibliography

1. Anderson Jr., J. D., *Hypersonic and High Temperature Gas Dynamics*, Reston, 2nd ed., 2006.

2. Sayler, K. M., "Hypersonic weapons: Background and issues for Congress," *Key Congressional Reports for July 2019. Part I*, 2019, pp. 161–194.

3. Woolf, A. F., "Conventional prompt global strike and long-range ballistic missiles: Background and issues (updated)," *Key Congressional Reports for August 2019: Part IX*, 2020, pp. 181–264.

4. Aarten, S. R., "The Impact of Hypersonic Missiles on Strategic Stability," *De militaire spectator*, 2020, pp. 182–193.

5. Vasile, J. D., Fresconi, F., Despirito, J., Duca, M., Recchia, T., Grantham, B., Rodney, D. W., and White, E. B., "High-Speed Army Reference Vehicle," 2022.

6. Chapman, D. R., "An Approximate Analytical Method for Studying Entry into Planetary Atmospheres," Tech. Rep. NACA TN 4276, NACA, Washington, May 1958.

7. Sutton, K. and Graves, Jr., R. A., "A General Stagnation-Point Convective-Heating Equation for Arbitrary Gas Mixtures," Tech. Rep. NASA TR R-376, NASA Langley Research Center, Hampton, VA, November 1971.

8. Galman, B. A., "Some Fundamental Considerations For Lifting Vehicles in Return From Satellite Orbit," *Planetary and Space Science*, Vol. 4, 1961, pp. 399–410.

9. Rizvi, S. T. u. I., shu He, L., and jun Xu, D., "Optimal trajectory and heat load analysis of different shape lifting reentry vehicles for medium range application," *Defence Technology*, Vol. 11, No. 4, 2015, pp. 350–361.

10. Bertin, J. J., *Hypersonic Aerothermodynamics*, American Institute of Aeronautics and Astronautics Conference, Washington, D.C., 1994.

11. Anderson Jr., J. D., *Modern Compressible Flow*, McGraw Hill Inc., New York, 1982.

12. Jorris, T. R., "Common Aero Vehicle Autonomous Reentry Trajectory Optimization Satisfying Waypoint and No-fly Zone Constraints," 2007.

13. Hood, L. G., Bennett, G., and Parish, J. J., "Model fidelity studies for rapid trajectory optimization," *AIAA Scitech 2019 Forum*, January 2019.

14. Masternak, T. J., "Multi-Objective Trajectory Optimization of a Hypersonic Reconnaissance Vehicle with Temperature Constraints," *AFIT Dissertations and Theses*, June 2014.

15. Kadam, S. R. and Hablani, H. B., "Trajectory optimization of reentry capsule," *IFAC Proceedings Volumes (IFAC-PapersOnline)*, Vol. 3, 2014, pp. 68–74.

16. Coulter, B., Wang, Z., Huang, D., and Yao, Y., "Hypersonic Trajectory Optimization with High-Fidelity Aerothermodynamic Models," *AIAA Scitech 2021 Forum*, January 2021, pp. 1–17.

17. Lees, L., "Hypersonic Flow," *Journal of Spacecraft and Rockets*, Vol. 40, No. 5, 2003, pp. 700–735.

18. Wright, M. and Dec, J., "Aerothermodynamic and Thermal Protection System Aspects of Entry System Design Course," *NASA Thermal and Fluids Analysis Workshop*, Pasadena, 2012.

19. Royal Society of Chemistry, "Periodic Table," 2022.

20. Grant, M. J. and Antony, T., "Rapid Indirect Trajectory Optimization of a Hypothetical Long Range Weapon System," *AIAA Atmospheric Flight Mechanics Conference*, January 2016.

21. Hellman, B. M., "Trajectory Approaches for Launching Hypersonic Flight Tests," *AIAA SPACE 2014 Conference and Exposition*, 2014.

22. Hui, X., Guangbin, C., Shengxiu, Z., Xiaogang, Y., and Mingzhe, H., "Hypersonic Reentry Trajectory Optimization by Using Improved Sparrow Search Algorithm and Control Parametrization Method," *Advances in Space Research*, Vol. 69, No. 6, 2022, pp. 2512–2524.

23. Makkapati, V. R., Ridderhof, J., Tsiotras, P., Hart, J., and Van Bloemen Waanders, B., "Desensitized Trajectory Optimization for Hypersonic Vehicles," *IEEE Aerospace Conference Proceedings*, Vol. 2021-March, 2021.

24. Rexius, S. L., Rexius, T. E., Jorris, T. R., and Rao, A. V., "Advances in highly constrained multi-phase trajectory generation using the General Pseudospectral Optimization Software GPOPS," *AIAA Guidance, Navigation, and Control (GNC) Conference*, , No. 412, 2013, pp. 1–16.

25. Bettinger, R. A., "The Prospect of Responsive Spacecraft Using Aeroassisted, Trans-Atmospheric Maneuvers," *AFIT Scholar*, June 2014.

26. Cummings, R. H., Mason, W. H., Morton, S. A., and McDaniel, D. R., *Applied Computational Aerodynamics*, Cambridge University Press, New York, 2015.

27. Weiland, C., *Aerodynamic Data of Space Vehicles*, Springer, Berlin, 2014.

28. Science Museum Group Collection, "Apollo 10 command module," Accessed on September 2022.

29. National Air and Space Museum, "North American X-15," Accessed on September 2022.

30. Hollis, B. R. and Borrelli, S., "Aerothermodynamics of Blunt Body Entry Vehicles," *Progress in Aerospace Sciences*, Vol. 48-49, 2012, pp. 42–56.

31. Dalle, D. J., "Interactions between Flight Dynamics and Propulsion Systems of Air-Breathing Hypersonic Vehicles," *AFIT Dissertations and Theses*, 2013.

32. Dunkel, M. A., "The Impact of Atmospheric Fluctuation on Optimal Boost Hypersonic Vehicle Dynamics," *The Air Force Institute of Technology*, 2017.

33. Kirk, D. E., *Optimal Control Theory: an introduction*, Dover Publications, Inc., Mineola, 1998.

34. Betts, J. T., "Survey of Numerical Methods for Trajectory Optimization," *Journal of Guidance, Control, and Dynamics*, Vol. 21, No. 2, 1998, pp. 193–207.

35. Benson, D. A., Huntington, G. T., Thorvaldsen, T. P., and Rao, A. V., "Direct trajectory optimization and costate estimation via an orthogonal collocation method," *Collection of Technical Papers - AIAA Guidance, Navigation, and Control Conference 2006*, Vol. 4, August 2006, pp. 2731–2744.

36. Patterson, M. A. and Rao, A. V., "GPOPS-II manual: A General-Purpose MATLAB Software for Solving Multiple-Phase Optimal Control Problems Version 2.3," December 2016, pp. 1–72.

37. Patterson, M. A. and Rao, A. V., "CGPOPS: A C++ Software for Solving Multiple-Phase Optimal Control Problems Using Adaptive Gaussian Quadrature Collocation and Sparse Nonlinear Programming," *ACM Transactions on Mathematical Software*, Vol. 41, No. 1, 2014.

38. Karasz, W. J., "Optimal Re-entry Trajectory Terminal State Due to Variations in Waypoint Locations," March 2008.

39. Scott, C. D., Ried, R. C., Maraia, R. J., Li, C.-P., Derry, S. M., Scott, C. D., Robert, C., Li, C.-p., and Derryo, S. M., "An AOTV Aeroheating and Thermal Protection Study," *AIAA 19th Thermophysics Conference*, 1984.

40. Rizvi, S. T. U. I., Linshu, H., and Dajun, X., "Optimal trajectory analysis of hypersonic boost-glide waverider with heat load constraint," *Aircraft Engineering and Aerospace Technology*, Vol. 87, No. 1, 2015, pp. 67–78.

41. Lee, C. J., "Hypersonic Vehicle Control and Trajectory Determination Through the Application of Artificial Intelligence," March 2020.

42. Woodbank Communications Ltd, "Simple Missile Ballistics, Orbits and Aerodynamics," 2005.

43. US Air Force, "AIM-120 AMRAAM," Accessed on January 2023.

44. Hicks, K. D., *Introduction to Astrodynamic Reentry*, Air Force Institute of Technology, 2009.

45. Duan, G., Sun, Y., Zhang, M., Zhang, Z., and Gao, X., "Aerodynamic coefficients models of hypersonic vehicle based on aero database," *Proceedings - 2010 1st International Conference on Pervasive Computing, Signal Processing and Applications, PCSPA 2010*, 2010, pp. 1001–1004.

REPORT DOCUMENTATION PAGE

Form Approved
OMB No. 0704–0188

1. REPORT DATE *(DD–MM–YYYY)*	2. REPORT TYPE	3. DATES COVERED *(From — To)*
23–03–2023	Master's Thesis	Sept 2021 — Mar 2023

4. TITLE AND SUBTITLE

DIRECT METHODS FOR COMPARISON OF AEROTHERMODYNAMIC MODEL EFFECTS ON HYPERSONIC TRAJECTORY OPTIMIZATION BY THE CONTINUATION PROCESS

5a. CONTRACT NUMBER

5b. GRANT NUMBER

5c. PROGRAM ELEMENT NUMBER

6. AUTHOR(S)

Khan, Noor K, 2nd Lt, USAF

5d. PROJECT NUMBER

5e. TASK NUMBER

5f. WORK UNIT NUMBER

7. PERFORMING ORGANIZATION NAME(S) AND ADDRESS(ES)

Air Force Institute of Technology
Graduate School of Engineering and Management (AFIT/EN)
2950 Hobson Way
WPAFB OH 45433-7765

8. PERFORMING ORGANIZATION REPORT NUMBER

AFIT-ENY-MS-23-M-278

9. SPONSORING / MONITORING AGENCY NAME(S) AND ADDRESS(ES)

10. SPONSOR/MONITOR'S ACRONYM(S)

11. SPONSOR/MONITOR'S REPORT NUMBER(S)

12. DISTRIBUTION / AVAILABILITY STATEMENT

DISTRIBUTION STATEMENT A:
APPROVED FOR PUBLIC RELEASE; DISTRIBUTION UNLIMITED.

13. SUPPLEMENTARY NOTES

14. ABSTRACT

An algorithm was created to optimize trajectories of hypersonic glide vehicles with selected cost functions by applying the process of continuation to direct orthogonal collocation methods. The trajectory was optimized to maximize the range of launch position given a fixed terminal location. The hypersonic glide vehicle system dynamics were modeled with three-dimensional, three degree of freedom equations of motion assuming no thrust and a non-rotating Earth with the control as bank angle. Three aerothermodynamic models were compared when input as path constraints to calculate the stagnation point heating rate at the nose as well as integrated for heat load. Use of the continuation method enabled rapid generation of converged optimized trajectories. Differences noted between iterations of the continuation process showed the evolution of vehicle trajectories based on the problem formulations. The continuation method was demonstrated as an effective tool for optimization. Each aerothermodynamic model rendered a different optimal trajectory with the Sutton Graves model producing the most conservative heat flux and heat load estimates.

15. SUBJECT TERMS

hypersonic trajectory optimization, direct orthogonal collocation methods, psuedospectral methods, GPOPS-II, continuation process, aerothermodynamic models, stagnation point heating rate, hypersonic glide vehicle (HGV)

16. SECURITY CLASSIFICATION OF:			17. LIMITATION OF ABSTRACT	18. NUMBER OF PAGES	19a. NAME OF RESPONSIBLE PERSON
a. REPORT	b. ABSTRACT	c. THIS PAGE			Lt Col Michael Zollars, AFIT/ENY
U	U	U	UU	133	19b. TELEPHONE NUMBER *(include area code)* (937) 255-3636; michael.zollars@afit.edu